



HAL
open science

Adaptive optics in full-field spatially incoherent interferometry and its retinal imaging

Peng Xiao

► **To cite this version:**

Peng Xiao. Adaptive optics in full-field spatially incoherent interferometry and its retinal imaging. Human health and pathology. Université Paris sciences et lettres, 2017. English. NNT : 2017PSLET015 . tel-02310664

HAL Id: tel-02310664

<https://pastel.hal.science/tel-02310664>

Submitted on 10 Oct 2019

HAL is a multi-disciplinary open access archive for the deposit and dissemination of scientific research documents, whether they are published or not. The documents may come from teaching and research institutions in France or abroad, or from public or private research centers.

L'archive ouverte pluridisciplinaire **HAL**, est destinée au dépôt et à la diffusion de documents scientifiques de niveau recherche, publiés ou non, émanant des établissements d'enseignement et de recherche français ou étrangers, des laboratoires publics ou privés.

THÈSE DE DOCTORAT

de l'Université de recherche Paris Sciences et Lettres
PSL Research University

Préparée à École Supérieure de Physique et de Chimie
Industrielles de la Ville de Paris

ADAPTIVE OPTICS IN FULL-FIELD SPATIALLY INCOHERENT INTERFEROMETRY AND ITS RETINAL IMAGING

Ecole doctorale n°564

École Doctorale Physique en Île-de-France

Spécialité Physique

Soutenu par PENG XIAO
le 16 Novembre 2017

Dirigée par **Mathias FINK**
et **A. Claude BOCCARA**

COMPOSITION DU JURY :

M. ROUSSET Gérard
Université Paris-Diderot, Rapporteur

Mme. LEVEQUE-FORT Sandrine
Université Paris-Sud, Rapporteur

Mme. MAITRE Agnès
UPMC, Présidente du jury

M. PAQUES Michel
UPMC, Membre du jury

M. MEIMON Serge
ONERA, Membre du jury

M. FINK Mathias
ESPCI, Directeur de thèse

M. BOCCARA Claude
ESPCI, Co-Directeur de thèse



THÈSE DE DOCTORAT
de l'université de recherche Paris Sciences et Lettres
PSL Research University

Spécialité

Optique Physique

(ED 564 - Physique en Île-de-France)

Préparée à l'INSTITUT LANGEVIN - ONDES ET IMAGES
ÉCOLE SUPÉRIEURE DE PHYSIQUE ET DE CHIMIE INDUSTRIELLES DE LA VILLE DE PARIS

Présentée par

Peng XIAO

sous la direction de

Mathias FINK et A. Claude BOCCARA

Pour obtenir le grade de

DOCTEUR de l'UNIVERSITÉ DE RECHERCHE PARIS SCIENCES ET LETTRES

Sujet de la thèse :

**Adaptive optics in full-field spatially incoherent
interferometry and its retinal imaging**

Soutenue le 16 Novembre 2017

devant le jury composé de :

M.	ROUSSET	Gérard	Rapporteur
Mme.	LEVEQUE-FORT	Sandrine	Rapporteur
Mme.	MAITRE	Agnès	Présidente du jury
M.	PAQUES	Michel	Examineur
M.	MEIMON	Serge	Examineur
M.	FINK	Mathias	Directeur de thèse
M.	BOCCARA	Claude	Co-Directeur de thèse

Acknowledgements

Firstly, I would like to offer my sincere appreciation to my thesis advisors Prof. Mathias FINK and Prof. A. Claude BOCCARA for giving me this great opportunity to work with and learn from them. I could not have imagined having better advisors and mentors for my PhD study. Their guidance as well as the independence they have given to me are indispensable and crucial for me to tackle every obstacle during my PhD training. Their passion and attitude toward research and life have motivated me greatly to become a good researcher as well as a good person. I am immensely grateful to Claude for his trust and comfort during my hardest period when I first arrived in France. I could have not come to this step without his support.

Besides my advisors, I would also like to thank the rest of my honorable jury members for their valuable time to review my thesis and participate in my thesis defense. Thanks to Prof. Gérard ROUSSET, Serge MEIMON and Sandrine LEVEQUE-FORT for writing the thesis reports with their professional suggestions and comments. Thanks to Prof. Michel PAQUES for his insightful comments from the point of view as a medical doctor and thanks to Prof. Agnès MAITRE for being the president of the jury and writing the defense report for me.

My gratitude also goes to the former and current FFOCT group members: Olivier, Clément, Slava, Egidijus, Jules, Amir, Thu-mai and Daria, with whom I have shared the lab, experiment components, research ideas and problems, stimulating discussions as well as conference trips together. I am also grateful to our cooperators: Prof. Jose-alain SAHEL, Kate GRIEVE, Kristina IRSCH and Romain in Institut de la Vision for their discussions and suggestions.

My time in Institut Langevin was enjoyable in large part due to my fellow office-mates and friends: Slava, Léo, Olivier, Marion, Clément, Aurélien, Vincent, Jean-Baptiste, Yann, Baptiste, Kammel, Florian and Sander. Thanks for sharing those coffee breaks, drinks, parties, as well as the KTV and HOT POT night. All are unforgeable memories for my life in France.

There are much more than a thank-you I would like to say to my closest friends in Paris. We have shared innumerable memorable moments in France with both joys and sorrows. And I am also thankful to all my best friends in China for their continuous support. All of them are true friendships that I will treasure for a lifetime.

Last but not least, I would like to give my biggest appreciation and gratitude to my family for their unconditional love and support in all my endeavours.

This thesis follows the study and development of an adaptive optics full-field optical coherence tomography (AO-FFOCT) system, aiming for high resolution *en face* human retinal imaging. During the quantification of the effects of geometrical aberrations on the FFOCT system performance, it is shown that, with spatially incoherent illumination, the lateral resolution of FFOCT is insensitive to aberrations, which only cause the FFOCT signal reduction. Since low order aberrations like myopia and astigmatism dominate in human eye, a non-conjugate AO configuration by using transmissive wavefront corrector is suggested and applied for low order aberrations correction to simplify the AO-FFOCT system. Wavefront corrections are done with a wavefront sensorless method by using FFOCT signal level as the metric. Experiments with scattering samples and artificial eye model are conducted to demonstrate the feasibility of the customized AO-FFOCT system for aberration correction. In order to resolve the eye motion effects and employ real-time matching of the optical path lengths of the two interferometric arms in FFOCT, a system combination of traditional spectral-domain OCT with FFOCT is adopted. With this combined system, high resolution FFOCT cellular retinal imaging is achieved in human eye *in vivo* for the first time.

Keywords:

Full-field optical coherence tomography, Adaptive optics, Spatial coherence, High resolution, Retinal imaging, Ophthalmology

Cette thèse traite de l'étude et du développement d'un système d'optique adaptative pour la tomographie par cohérence optique plein champ (AO-FFOCT en anglais) appliquée à l'imagerie haute résolution de la rétine. L'analyse de l'effet des aberrations géométriques sur les performances en FFOCT a montré que pour une illumination spatialement incohérente, la résolution transverse est insensible aux aberrations et ne fait que diminuer le niveau du signal. Comme ce sont des aberrations de bas ordres comme la myopie et l'astigmatisme qui prédominent pour l'œil humain, une méthode d'optique adaptative avec une configuration sans conjugaison qui utilise une correction de front d'onde en transmission est suggérée, puis appliquée à la correction de ces ordres afin de simplifier le système d'AO-FFOCT. Des corrections de front d'onde sont effectuées sans analyseur de surface d'onde, en utilisant le niveau du signal de FFOCT comme métrique. Des expériences avec des échantillons diffusants et un œil artificiel sont menées pour démontrer la faisabilité d'un système d'AO-FFOCT conçu pour la correction d'aberration. Afin de résoudre les problèmes posés par les mouvements oculaires et de compenser en temps réel la différence de chemin optique entre les deux bras de l'interféromètre, l'instrument de FFOCT est couplé à un système d'OCT spectral. Avec cette combinaison de systèmes, l'imagerie FFOCT *in vivo* cellulaire de la rétine à haute résolution a été réalisée pour la première fois sur l'œil humain.

Mots clés:

Tomographie par cohérence optique plein champ, Optique adaptative, Cohérence spatiale, Haute résolution, Imagerie de la rétine, Ophtalmologie

Contents

Introduction	1
I Optical Coherence Tomography and Adaptive Optics in Retinal Imaging	5
1 Optical coherence tomography (OCT)	7
1.1 Imaging in scattering media	8
1.2 Introduction of OCT	9
1.3 Low coherence interferometry (LCI)	11
1.4 OCT performances	13
1.4.1 Axial resolution	13
1.4.2 Lateral resolution	13
1.4.3 Field of view	14
1.4.4 Sensitivity	15
1.5 OCT techniques	15
1.5.1 Scanning OCT	15
1.5.2 Parallel OCT	17
2 Wavefront correction with adaptive optics	19
2.1 Wavefront aberration	20
2.2 Aberration representation with Zernike polynomials	20
2.3 Strehl ratio	22
2.4 Adaptive optics (AO)	23
2.4.1 Introduction of AO	23
2.4.2 Wavefront corrector	24
2.4.3 Direct wavefront sensing	27
2.4.4 Indirect wavefront measurement based on image analysis	27
2.5 Computational adaptive optics	30
3 The human eye and retinal imaging	31
3.1 Imaging properties of human eye	32
3.1.1 The structure and geometry of human eye	32
3.1.2 Eye aberrations	34
3.1.3 Eye movements	36
3.2 Retinal imaging	37
3.2.1 Flood illuminated fundus camera	37
3.2.2 Scanning laser ophthalmoscope	38

3.2.3	OCT retinal imaging	39
II	Full-field Optical Coherence Tomography and its Adaptive Optics	45
4	Full-field optical coherence tomography (FFOCT)	47
4.1	Introduction	48
4.2	Basic principles of FFOCT	48
4.2.1	Basic layout	48
4.2.2	Image acquisition	50
4.3	FFOCT performances	52
4.3.1	Resolution	52
4.3.2	Field of view	52
4.3.3	Sensitivity	52
4.3.4	Comparison of FFOCT with other OCT techniques	53
4.4	LightCT scanner	53
4.5	FFOCT applications	55
4.5.1	Histological evaluation of <i>ex vivo</i> tissues	55
4.5.2	Dynamic FFOCT imaging	56
4.5.3	Inner fingerprint imaging	57
5	FFOCT resolution insensitive to aberrations	59
5.1	Aberration fuzziness and PSF	60
5.2	The unexpected PSF determination using nanoparticles in FFOCT	61
5.3	Optical coherence	61
5.3.1	Temporal coherence	63
5.3.2	Spatial coherence	63
5.4	Theoretical system PSF analysis in various OCTs	65
5.4.1	Scanning OCT with spatially coherent illumination	66
5.4.2	WFOCT with spatially coherent illumination	66
5.4.3	FFOCT with spatially incoherent illumination	68
5.5	Experimental confirmation with extended object	71
5.5.1	USAF imaging with defocus	71
5.5.2	UASF imaging with random aberration	72
6	Adaptive optics FFOCT (AO-FFOCT)	75
6.1	Simplifying AO for low order aberrations in FFOCT	76
6.1.1	Plane conjugation in AO induce system complexity	76
6.1.2	Non-conjugate AO for eye's low order aberration correction	77
6.1.3	Wavefront sensorless method further simplify the system	77
6.2	The compact AO-FFOCT setup	78
6.3	Aberration correction algorithm	79
6.4	LCSLM-induced aberration correction	80
6.4.1	Non-conjugate AO	80
6.4.2	Conjugate AO	83

6.5	Sample induced aberration correction	83
6.5.1	Ficus leaf experiment: weak aberration correction	83
6.5.2	Mouse brain slice: strong aberration correction	84
6.6	AO-FFOCT retinal imaging of artificial eye model	86
III	<i>In vivo</i> Human Retinal Imaging with FFOCT	89
7	Combing FFOCT with SDOCT for <i>in vivo</i> human retinal imaging	91
7.1	Introduction	92
7.2	Combining FFOCT with SDOCT	93
7.3	Eye safety analysis	96
7.4	System performance validation with artificial eye model	99
7.5	<i>In vivo</i> human retinal imaging	100
7.5.1	FFOCT retinal imaging of the fovea	100
7.5.2	FFOCT retinal imaging of retinal near periphery	103
	Conclusions and perspectives	105
	Publications	109
	References	111

List of abbreviations

- **AMD:** Age-related Macular Degeneration
- **AO:** Adaptive Optics
- **CA:** Coherence Area
- **DME:** Diabetic Macular Edema
- **FDOCT:** Fourier-domain Optical Coherence Tomography
- **FFT:** Fast Fourier Transform
- **FFOCT:** Full-field Optical Coherence Tomography
- **FOV:** Field of View
- **FTIR:** Frustrated Total Internal Reflection
- **FWHM:** Full Width at Half Maximum
- **IS/OS:** Inner/Outer Segment
- **LCI:** Low Coherence Interferometry
- **LCSLM:** Liquid Crystal Spatial Light Modulator
- **LED:** Light-emitting Diode
- **MRI:** Magnetic Resonance Imaging
- **NA:** Numerical Aperture
- **NIR:** Near-Infrared Light
- **OCT:** Optical Coherence Tomography
- **OCM:** Optical Coherence Microscopy
- **OPL:** Optical Path Length
- **PSF:** Point Spread Function
- **PZT:** Piezoelectric Transducer
- **RMS:** Root Mean Square
- **RNFL:** Retinal Nerve Fibre Layer
- **RPE:** Retinal Pigment Epithelium
- **SDOCT:** Spectral-domain Optical Coherence Tomography
- **SLD:** Super-luminescent Diode
- **SLM:** Spatial Light Modulator
- **SLO:** Scanning Laser Ophthalmoscope
- **SNR:** Signal-to-Noise Ratio
- **SSOCT:** Swept-source Optical Coherence Tomography
- **TDOCT:** Time-domain Optical Coherence Tomography
- **UHR:** Ultrahigh-resolution
- **WFOCT:** Wide-field Optical Coherence Tomography

After about 25 years of development, optical coherence tomography (OCT) has become a powerful imaging modality [1, 2]. Similar to ultrasound technique but using light illumination, optical coherence tomography (OCT) has been broadly used in biomedical imaging due to its high resolution, high sensitivity and non-contact advantages. By measuring the echoes of backscattered light that indicates the structures inside biological samples with light interferometry, cross-sectional images are usually formed. OCT techniques have proved important and successful applications in ophthalmology, especially in retinal imaging. The cross-sectional depth exploration of the retinal layers offers important information of pathologies for early diagnosis of retinal diseases and tracing disease evolutions. Nevertheless, due to the habitual use of imaging devices like fundus camera or scanning laser ophthalmoscope (SLO), ophthalmologists often ask for *en face* images of OCT. Thanks to the speed improvement of OCT systems, *en face* retinal images can be obtained by real-time 3-dimension imaging. But because of the requirement of large depth of focus, low numerical aperture (NA) objectives are typically used in traditional OCTs results in relatively lower spatial resolution compared with microscopes that use high NA objectives.

Developed in ESPCI Paris, Full-field OCT (FFOCT) is a kind of parallel OCT techniques that use full-field illumination and an array detector to acquire *en face* images perpendicular to the optical axis without lateral scanning [3, 4]. By utilising high NA microscope objectives in a Linnik interferometer configuration, FFOCT is able to achieve standard microscope spatial resolution. Since its introduction, FFOCT has been applied in various researches and medical studies like rapid histological evaluation of *ex vivo* tissue samples, human breast and brain tissue characterization, human inner fingerprint detection, non-destructive material evaluation and also *ex vivo* ophthalmology studies to provide morphological characterization of the ocular tissues. While FFOCT system is able to achieve micron resolution in 3-dimension with microscope objectives and broadband light source to select ballistic photons from scattering light, aberration needs to be considered when apply it to in-depth imaging into biological samples or eye imaging.

Aberrations present in the eye are typically induced by the curvature irregularities of cornea and crystalline lens, tear film or some eye diseases. It is one of the main limitations that degrade the imaging performance of variety of optical instrumentations for eye imaging, especially for retinal examination when the eye works as an optical element of the imaging sys-

tem. Adaptive optics (AO), which is originally developed for astronomical imaging to correct atmosphere-induced wavefront distortion, are broadly used to measure and correct eye aberrations in retinal imaging in combination with different imaging modalities like flood-illuminated ophthalmoscope, SLO and OCT. Typically, with AO added, the spatial resolution and signal to noise ratio (SNR) of these systems are increased result in better visualization of the retinal structures.

As a part of the ERC HELMHOLTZ synergy program whose aim is to explore the holistic evaluation of light and multi-wave techniques in ophthalmic studies, the work expound in this thesis belongs to a sub-project aiming to apply FFOCT system for high resolution *en face* human retinal imaging. To apply FFOCT for *in vivo* retinal imaging, eye aberration is the first important thing that needs to be considered. This thesis therefore is concerned with the effects of aberrations on the performance of FFOCT and the development of an AO-FFOCT for aberration correction. Then the subsequent work is to adapt FFOCT to *in vivo* human retinal imaging.

The thesis is divided into three main parts:

The first part focuses on OCT and AO as well as their applications in human retinal imaging. In chapter 1, the backgrounds and basic principles of OCT is introduced. The definition of various parameters such as resolution, field of view and sensitivity indicating OCT performances are detailed. Various OCT techniques are briefly discussed based on their imaging formation methods. In chapter 2, the causes of wavefront aberrations are discussed. The representation of aberrations by Zernike polynomials and aberration quantification by Strehl ratio are presented. What's more, the concept of AO and its basic components are illustrated. Different wavefront correctors and wavefront sensing methods are presented as well as the pros and cons and their potential applications. Chapter 3 aims to introducing the imaging properties of human eye, including its structural and geometrical formation, especially on the human retina structures and functions. Also, current retinal imaging modalities such as fundus camera, SLO and OCT are presented and compared. The combination of these retinal imaging techniques with AO are also discussed.

The second part of the thesis focus on FFOCT and its adaptive optics. Chapter 4 introduces the basic layout of FFOCT system and its imaging acquisition methods. The FFOCT performance parameters are presented and the comparison its main features with the other OCT techniques are shown. It also includes the applications of FFOCT together with some newly developed FFOCT techniques such as dynamic FFOCT for intra-cellular motion detection and FFOCT for inner fingerprint imaging. Chapter 5 focuses on the work on quantifying the FFOCT resolution performance in presence of aberrations. Both theoretical analysis and experimental results are presented to show that in FFOCT system with a spatially incoherent illumination, its lateral resolution is insensitive to geometrical aberrations with only signal level reduction, while it is not the case in the other OCT techniques with spatially coherent illuminations. This surprising finding supports FFOCT for human retinal imaging even without AO when aberration is not too large. In chapter 6, a simplified AO-FFOCT system is introduced with non-conjugate AO by using an transmissive liquid crystal spatial light modulator (LCSLM) for low order aberration correction. A wavefront sensorless method is applied that further simplified the system with the image intensity as the metric since aberration affects only the signal level in FFOCT. Non-conjugate AO is compared with conjugate-AO experimentally.

And the system is applied for sample induced aberration correction in a ficus leaf and also mouse brain tissue slice. At last, the AO-FFOCT retinal imaging is demonstrated with an artificial eye model to improve signal level by correcting low order aberrations.

The third part of the thesis mainly shows the application of FFOCT for *in vivo* human retinal imaging. In chapter 7, in order to resolve the problem of optical path length (OPL) matching in FFOCT for *in vivo*, the FFOCT is combined with a SDOCT system to realise real-time matching of the OPL for FFOCT. The evaluation of the illumination on eye safety is calculated. The combined system performance is validated by doing artificial eye model retinal imaging. Finally, *in vivo* human retinal imaging are performed with the combined system and the results are presented. *En face* high resolution FFOCT images of different retinal layers are acquired showing cellular level retinal structures like nerve fibres, blood vessels as well as retinal photoreceptors.

In the end of this thesis, a conclusion sums all the achievements of this thesis work and the current stage of FFOCT system in human retinal imaging. Also the perspectives and challenges of FFOCT for *in vivo* human retinal imaging and eye examination are discussed.

Part I

Optical Coherence Tomography and Adaptive Optics in Retinal Imaging

Optical coherence tomography (OCT)

Table of contents

1.1	Imaging in scattering media	8
1.2	Introduction of OCT	9
1.3	Low coherence interferometry (LCI)	11
1.4	OCT performances	13
1.4.1	Axial resolution	13
1.4.2	Lateral resolution	13
1.4.3	Field of view	14
1.4.4	Sensitivity	15
1.5	OCT techniques	15
1.5.1	Scanning OCT	15
1.5.2	Parallel OCT	17

1.1 Imaging in scattering media

With the rapid development of science and technology, many optical imaging techniques have been greatly improved. Optical imaging techniques refreshed our understanding of the world with tremendous performances, particularly in biology studies which have benefited a lot with the advances of optical microscopies. But in medical imaging, methods like ultrasound, computed tomography and magnetic resonance are still more preferred compared to optical modalities. This is due to the fact that the optical imaging window is considered to be from visible to near-infrared (NIR) spectrum (400-1350 nm) as light in this spectrum range suffers low absorption by biological tissues (figure 1.1(a)), while the heterogeneous structures in biological tissues are mostly in this range of optical wavelengths and strongly scatter light (figure 1.1(b)). This prevents optical instruments from in-depth imaging and has made optical imaging being a complementary method in many applications in medical imaging.

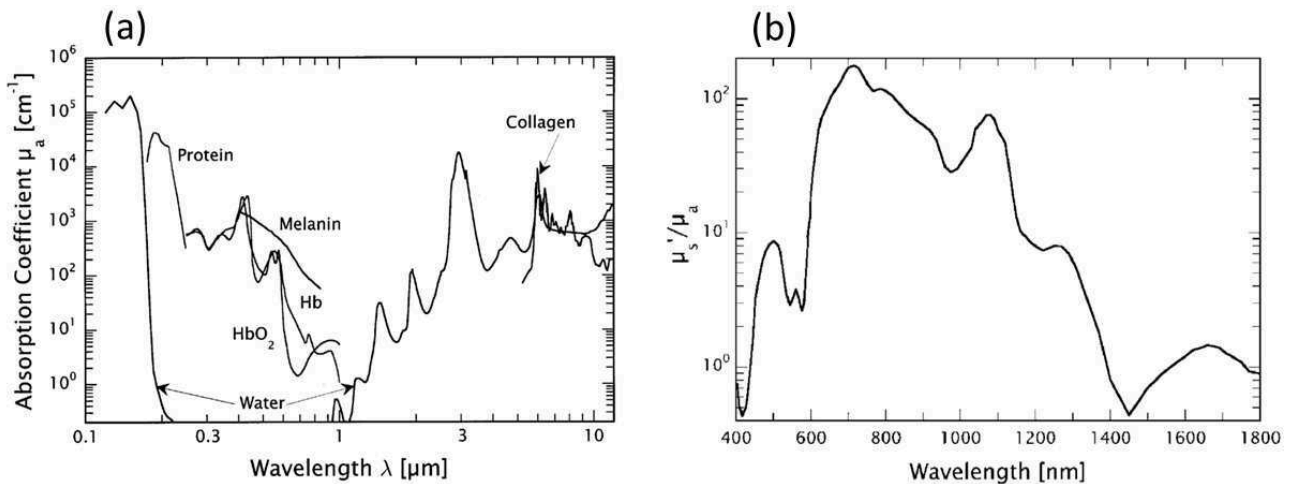


Figure 1.1 – Absorption and scattering in biological tissue [5]. (a) Absorption coefficient versus optical wavelength in the range of 0.1 – 12 μm. (b) Ratio of the reduced scattering coefficient to the absorption coefficient versus optical wavelength in the range of 400 – 1800 nm, scattering outside of this range is not characterized since it is dominant by absorption.

When doing optical imaging in scattering tissue, due to small variations of refractive index between biological structure, only extremely weak light would be backscattered and most of the light would be scattered by the surrounding structures. According to the Lambert-Beer law, the intensity of backscattered light, more precisely ballistic light, which contains the most useful information of the sample structures, decreases exponentially with the imaging depth. The multiply scattered signals would degrade the contrast, the resolution as well as the imaging

depth. So, to perform better optical imaging, the main challenge is to extract these low ballistic signals while rejecting the multiply scattered light.

To accomplish this challenge, different methods like spatial filtering [6], time reversal [7,8] or coherence detection [9] have been exploited. For example, the widely used confocal microscope is based on spatial filtering of out-of-focus light with a optically conjugated pinhole in front of the detector. The multiply scattered light rejection in confocal microscope has been both theoretically discussed and experimentally demonstrated in [10]. By combining the spatial filtering and coherence detection, imaging through scattering to produce high contrast images from very weak signals can also be achieved in optical coherence tomography (OCT) [1, 11], which is explained in details in the following sections.

1.2 Introduction of OCT

The OCT technique was first invented in the early 1990s in MIT [1]. Based on low coherence interferometry, OCT is now a well-established imaging modality by measuring the magnitude and echo time delay of backscattered light. It can provide cross-sectional (B-scan) and 3-dimensional volumetric internal sample structures with resolutions of $1 - 15\mu m$ by laterally scanning the optical beam and performing axial measurements of echo time delay (A-scan)(figure 1.2). Compared with other imaging methods, its non-invasiveness, high resolution, high sensitivity, low cost and easy to use advantages make OCT a powerful imaging modality with applications across many clinical fields as well as fundamental scientific and biological researches.

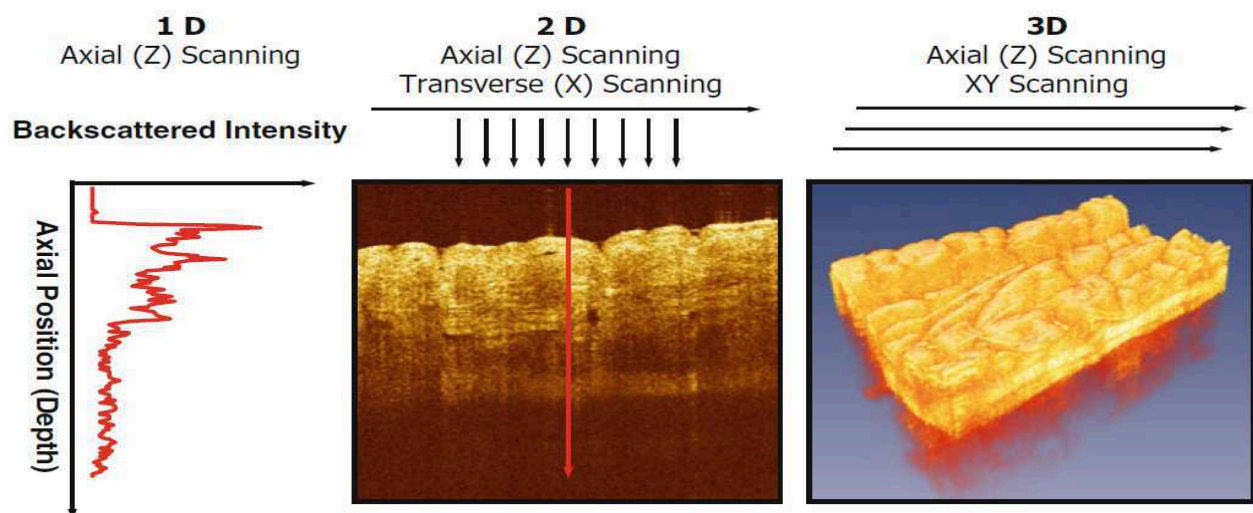


Figure 1.2 – OCT cross-sectional or 3-dimensional image formation [12]. Measurements of the backscattered light versus imaging depth forms axial scans(A-scan). By scanning the optical beam in transverse direction, a series of A-scans forms a cross-sectional OCT image (B-scan). Multiple B-scans would generate 3-dimensional OCT data sets by raster scanning.

OCT holds the features of both ultrasound and microscopy. Figure 1.3 shows the comparison of these imaging techniques in parameters as resolution and imaging depth. The clinical ultrasound uses acoustic waves with frequencies ranging between $3 - 40MHz$ and gives a resolution of $0.1 - 1mm$ [13]. Sound waves at these frequencies are transmitted with minimal absorption

in biological tissues so that deep imaging is possible in ultrasound. Although with higher frequency ultrasound (up to 100MHz), imaging resolution of $15 - 20\mu\text{m}$ could be achieved, the imaging depths would be limited to only a few millimetres as high frequencies sound waves are strongly attenuated in biological tissues. On the other hand, microscopy and confocal microscopy have high lateral resolutions up to $1\mu\text{m}$. However, imaging depth is limited because image signal and contrast are significantly degraded by optical scattering. Imaging can be performed to only a few hundred micrometers in most of the tissues.

OCT just fills the gap between ultrasound and microscopy. With current technology, imaging resolution of $1 - 15\mu\text{m}$ and a penetration depth of $2 - 3\text{mm}$ can be achieved. The high resolution of OCT imaging enables the visualization of tissue architectural morphology. The fact that OCT itself is also an optical imaging technique makes its imaging depth limited by the effects of absorption and scattering within the biological samples. The axial resolution of OCT is determined by the bandwidth of the light source. Better axial resolution can be achieved with broader bandwidth.

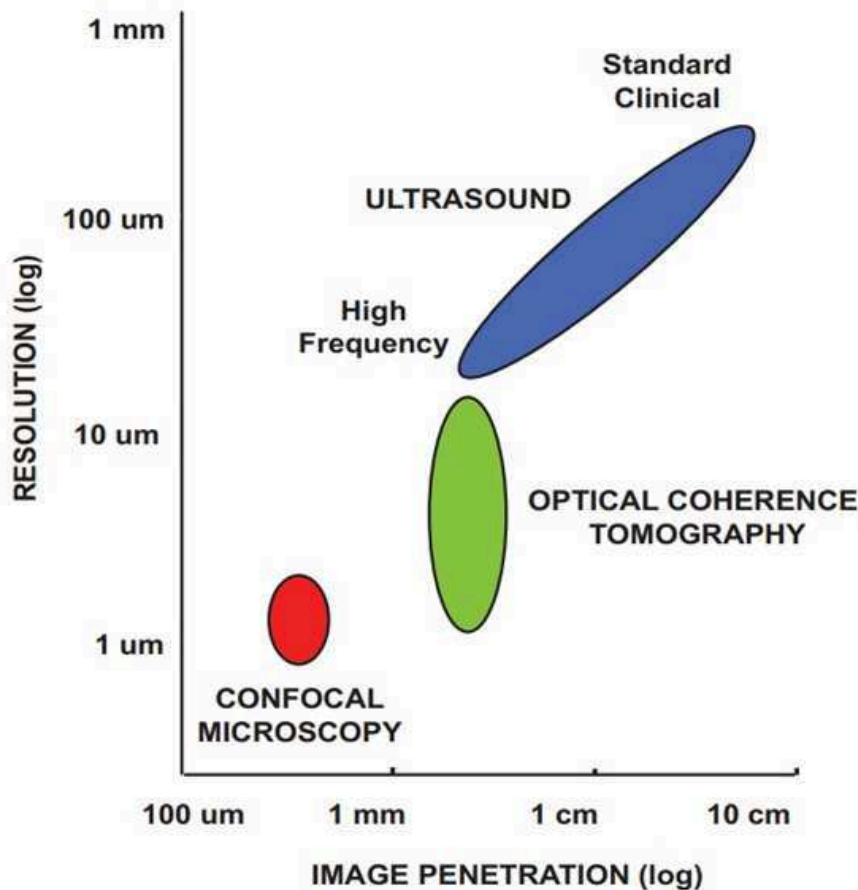


Figure 1.3 – Comparison of resolution and imaging depth for ultrasound, OCT and confocal microscopy [12].

After its invention, OCT has found successful application in ophthalmology imaging and has become a clinical standard in this field, especially in retinal imaging [14]. High resolution and non-contact imaging of anterior segment as well as retina is possible with OCT as the transparency of the eye offers easy access of the OCT beam to these eye structures with minimal optical attenuations and scattering. OCT performs non-invasive optical biopsy of living retina

which was only possible in *ex vivo* histology before. The high resolution cross-sectional sectioning of retina layers offers great potential for not only pathologies detection such as macular hole and retinal detachment (figure 1.4) [15, 16], but also early diagnosis of common eye disease like glaucoma [17] with the cell morphology and vascular structures revealed in individual retinal layers.

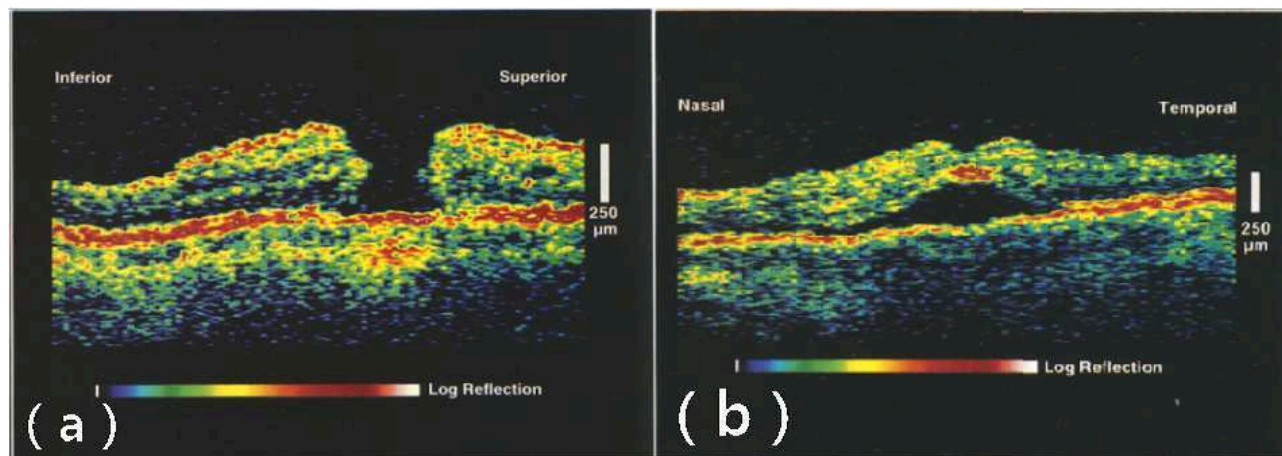


Figure 1.4 – OCT human retinal images indicating macular hole and detachment [15]. (a) OCT image shows a macular hole on the retina. (b) OCT image demonstrates detachment of the neurosensory retina.

The development of new light sources, high performance computers, different illumination geometries, and image construction methods is pushing OCT to achieve higher resolution and signal to noise (SNR) levels, faster imaging speed, larger imaging depth, and better image interpretation. Besides its application in ophthalmology field, OCT have also been utilised in many diverse areas such as oncology [18–20], dermatology [21–26], dentistry [27, 28], etc. Many alternative OCT techniques have also emerged based on the original OCT with endoscopic imaging probes giving access to internal organs [29–31], or signal orientations to explore various biological sample properties. Optical coherence elastography measures sample elastic properties [32–36], polarization sensitive OCT detects tissue birefringence information [25, 26, 37–39], phase-sensitive OCT reveals cellular morphology and dynamics [40–42], angiography OCT forms vascular maps [43–45] while Doppler OCT could offer functional information of blood flow [46–49]. Combination of difference OCT techniques and also complementary imaging modalities have also been demonstrate to do multifunctional imaging [50–53].

1.3 Low coherence interferometry (LCI)

Interferometry is an important method for the measurement of small optical path length changes, from which small displacements, refractive index changes or surface irregularities can be extracted. As mentioned before, OCT is based on a so called low coherence interferometry (figure 1.5(a)) to detect the magnitude and echo time delay of the backscattered light for sample structure reconstructions. Interferometry measures the electric field of the optical beam rather than its intensity. The function form of the electric field in a light wave is

$$E(t) = E_0 \cos\left(2\pi\nu t - \frac{2\pi}{\lambda} z\right). \quad (1.1)$$

As shown in figure 1.5a, the most commonly used interferometer in LCI is Michelson interferometer. Light $E_i(t)$ from the source is directed into the beamsplitter that splits the beam into the reference arm and a sample arm. The sample arm beam is incident on the tissue and undergoes partial reflection whenever it encounters a structure or surface within the tissue. Thus the sample reflected beam $E_s(t)$ contains multiple echoes from the interfaces within the tissue. The reference arm beam is directed to a reference mirror and reflected $E_r(t)$. Both beams travel back toward the beamsplitter, recombine and interfere, result in the output beam, which is the sum of the electromagnetic fields of both arms

$$E_o(t) \sim E_s(t) + E_r(t). \quad (1.2)$$

As the detector measures the output intensity which is proportional to the square of the electromagnetic field, it can be written as

$$I_o(t) \sim \frac{1}{4}|E_s|^2 + \frac{1}{4}|E_r|^2 + \frac{1}{2}E_s E_r \cos\left(2\frac{2\pi}{\lambda}\Delta l\right) \quad (1.3)$$

in which Δl is the path length difference between the sample arm and reference arm. Varying the position of the reference mirror changes the value of Δl will cause the two beams to interfere constructively or destructively. The intensity will oscillate between maximum and minimum each time the path length between reference arm and sample arm changes by one optical wavelength.

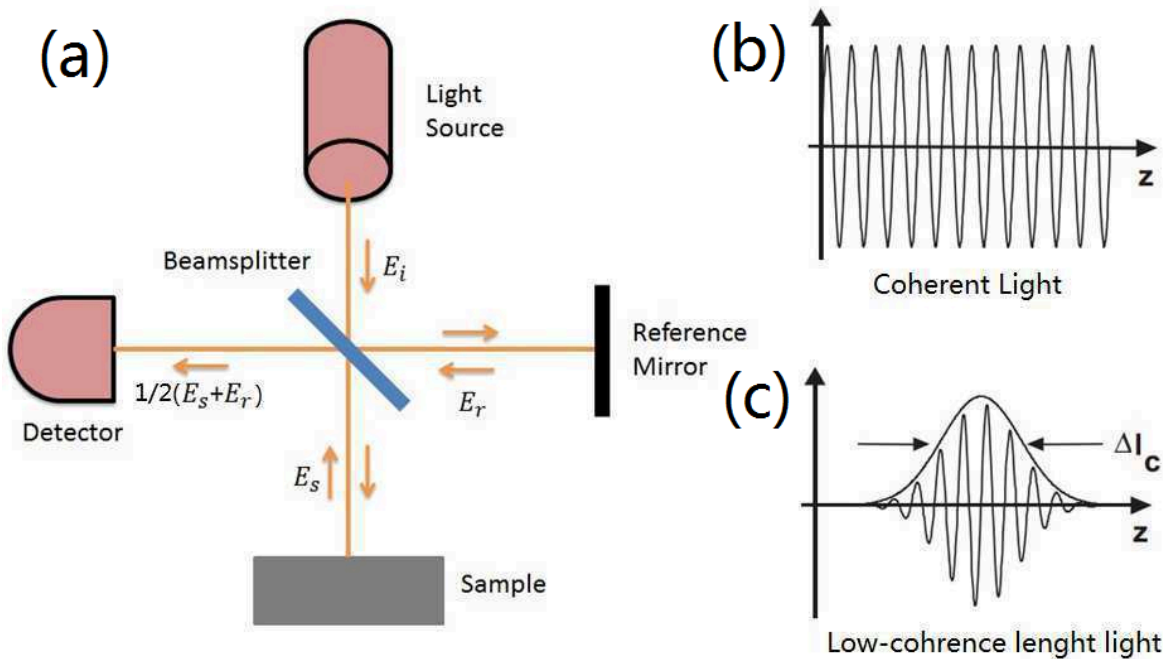


Figure 1.5 – Interference in low coherence interferometry. (a) A classic Michelson interferometer in which the backscattered or backreflected light is interfered with a scanning reference mirror. (b) If the light source is coherent, interference fringes will be observed for a wide range of path length difference. (c) If low coherence length light is used, interference occurs only when the optical path lengths of the two arms are matched within the coherence length l_c .

As it is shown in figure 1.5(b), if the light beam is coherent, interference patterns will be observed for a wide range of relative path length differences of the reference and sample arms.

However, in optical imaging, it is crucial to know the precise position of the structures within the sample, thus light with a low temporal coherence length (broad bandwidth) should be used. Low temporal coherence light is characterized by the temporal coherence length l_c , which is inversely proportional to the frequency bandwidth. It is also the spatial width of the field autocorrelation produced by the interferometer. With low temporal coherence length light (figure 1.5(c)), interference could only be seen when the paths travelled by the reference and sample arm beams are nearly equal. If the paths are mismatched by more than the coherence length of the light, the two electromagnetic fields from the two beams are not correlated, thus no interference effects are observed.

1.4 OCT performances

The OCT system performances are typically defined by several important parameters such as resolution, field of view and sensitivity. Figure 1.6 illustrate the basic sample arm geometrics of typical OCT systems.

1.4.1 Axial resolution

The dependence of the interference range on the temporal coherence length l_c of the broadband source in LCI, as explained in section 1.3, distinguishes OCT from traditional microscopy techniques, in which both axial and lateral resolution is dependent on the numerical aperture (NA) of the objectives. In OCT techniques, the determination of the axial resolution is independent of the beam focusing, given by the width of the electromagnetic field autocorrelation function. With a Gaussian-shaped spectrum, the OCT axial resolution is calculated as

$$\Delta z = \frac{2 \ln 2}{\pi} \cdot \frac{\lambda^2}{\Delta \lambda} \quad (1.4)$$

in which λ is the center wavelength of the light source and $\Delta \lambda$ is the full-width-half-maximum (FWHM) of the spectrum.

1.4.2 Lateral resolution

The lateral resolution of OCT is determined by the diffraction limited spot size on the focus plan that is proportional to wavelength and inversely proportional to the NA or the focusing angle of the beam. This could be calculated as

$$\Delta x = \Delta y = \frac{4 \lambda}{\pi} \cdot \frac{f}{d} \quad (1.5)$$

in which λ is the center wavelength, d is the size of the incident beam on the objective lens and f is the focal length [12]. So better lateral resolution could be obtained with large NA objective to form smaller spot size.

In fact in fiber-based OCT systems, the single mode fiber end works as a pinhole aperture in a reflection mode confocal microscopy to reject out-of-focus light and scattered photons, while explained later in full-field OCT (FFOCT) with spatially incoherent illumination the

spatial coherence area works as pinholes. In this way, the lateral resolution is actually slightly improved, calculated as

$$\Delta x = \Delta y = 0.37 \cdot \frac{\lambda}{NA} \quad (1.6)$$

in which λ is the center wavelength and NA is the effective numerical aperture of the system [12].

1.4.3 Field of view

Here, we define the depth of focus (depth of field) of OCT as the axial field of view. OCT imaging is usually performed with low NA focusing. As in microscopy, the axial field of view in OCT is related to the transverse resolution, defined as

$$FOV_{axial} = \frac{\pi \Delta x^2}{2\lambda}, \quad (1.7)$$

and the lateral field of view is typically determined by the scanning angle and can be calculated as

$$FOV_{lateral} = 2 \cdot f \cdot \theta_{max} \quad (1.8)$$

in which f is the focal length of the objective and θ_{max} is the maximum one-side scanning angle.

As discussed later, FFOCT achieves 3-dimensional imaging by doing *en face* imaging with depth scanning. The axial field of view is then limited by sample scattering and the lateral field of view is depend on the detector array size and system magnification.

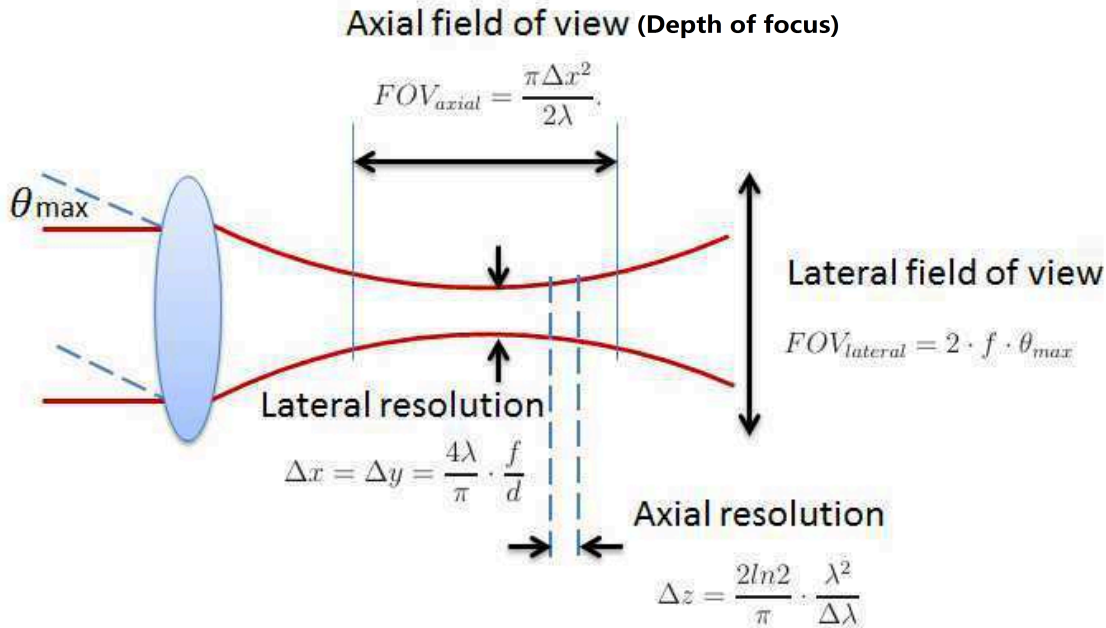


Figure 1.6 – Schematic of OCT sample arm optical geometrics. Formulas for calculating resolution and field of view of typical OCT systems are provided.

1.4.4 Sensitivity

OCT is able to measure very weak signal due to the fact that it detects the amplitude instead of the intensity with interferometry that is equivalent to optical heterodyne detection. The weak electric field of the sample beam from the tissue is multiplied by the large amplitude field from the reference arm, thus amplified the interference signal amplitude.

The most well-known expression for signal-to-noise ratio (SNR) calculation is

$$SNR = 10\log\left(\frac{\eta P}{2h\nu B_{\text{detection}}}\right), \quad (1.9)$$

in which η is the detector responsivity, $h\nu$ is the photon energy, P is the signal power from the sample arm and $B_{\text{detection}}$ is the electronic detection bandwidth. As $B_{\text{detection}}$ is related with A-scan depth and time, higher optical power would be needed to achieve the same SNR for higher imaging speed or resolution. Detailed calculation of the sensitivity for various modes of OCT could be found in section 2.9 in reference [12]. Based on the optical design and acquisition requirements, current OCT systems could reach sensitivities up to around -110dB [54].

1.5 OCT techniques

Based on the image generation geometries, point-by-point scanning or *en face* plane-by-plane imaging, OCT techniques can be briefly divided into scanning OCT or parallel OCT.

1.5.1 Scanning OCT

In scanning OCT systems, spatially coherent illumination like super-luminescent diode (SLD) or frequency-swept laser are typically used.

In early developed OCT systems, a scanning reference arm is implemented in a time-domain LCI with lateral scanning sample arm. In such systems, an A-scan is acquired by axially scanning the reference mirror to detect axial positions of the light re-emitting sites in samples. A series of A-scans at different lateral positions are performed using the lateral OCT beam scanner to addresses laterally adjacent sample positions in order to generate two-dimensional cross-sectional images (B-scan). Such type of OCT modality in which the depth profile in the sample is obtained sequentially in time by scanning the reference mirror with a constant speed is called time-domain OCT (TD-OCT) as shown in figure 1.7(a) [1]. *en face* scanning TD-OCT technique named optical coherence microscopy (OCM) has also been developed to achieve higher lateral resolution with higher NA objectives [55]. In OCM, instead of acquiring A-lines by scanning the reference mirror, *en face* image is obtained first by fast modulation of the lateral scanners. 3-dimensional image is then acquired by doing depth scanning with reference mirror.

Since the needs for mechanical scanning to obtain A-scans in TD-OCT limits the acquisition speed and SNR, soon after the report of TD-OCT, Fourier-domain OCT (FD-OCT) techniques was developed with increased imaging speed and system sensitivity [56–59], in which the depth profile is resolved in Fourier space as a function of the frequency. A-scans then be acquired by a Fourier transform of the frequency encoded profiles. Two methods are developed to record

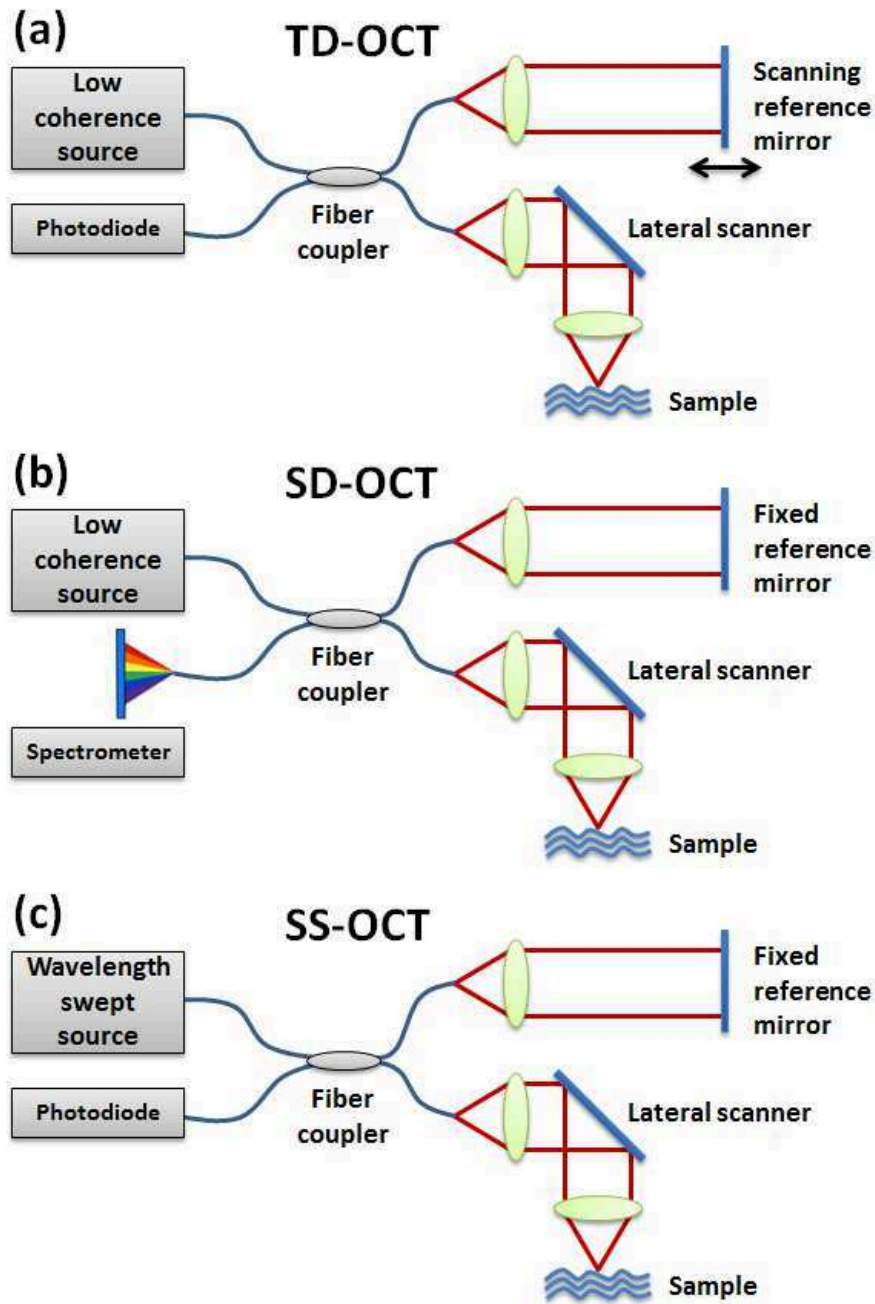


Figure 1.7 – Schematic of different scanning OCT techniques. (a) Time-domain OCT with scanning reference mirror, (b) Spectral-domain OCT with spectrometer and (c) Swept-source OCT with wavelength swept source.

the frequency spectrum of the interference signal. One uses a diffraction grating and a high speed line-scan camera to form a spectrometer, in which the spectrum frequency is associated with the depth location of the backscattering features within the sample. This technique is called spectral-domain OCT (SD-OCT) [59–61] as shown in figure 1.7(b). The other method of FD-OCT is using a narrow-bandwidth, frequency-swept light source and a photodiode as detector is called swept-source OCT (SS-OCT) (figure 1.7(c)) [62–64], in which the frequency profile is obtained by rapidly swept the emission wavelength of the light source and record the instantaneous interferometric signal with the photodetector as a function of time.

In FD-OCT techniques, there is a significant improvement in imaging speed since there is

no need for the scanning of reference arm. With the same imaging speed of TD-OCT and FD-OCT, FD-OCT techniques will offer considerably better sensitivity.

1.5.2 Parallel OCT

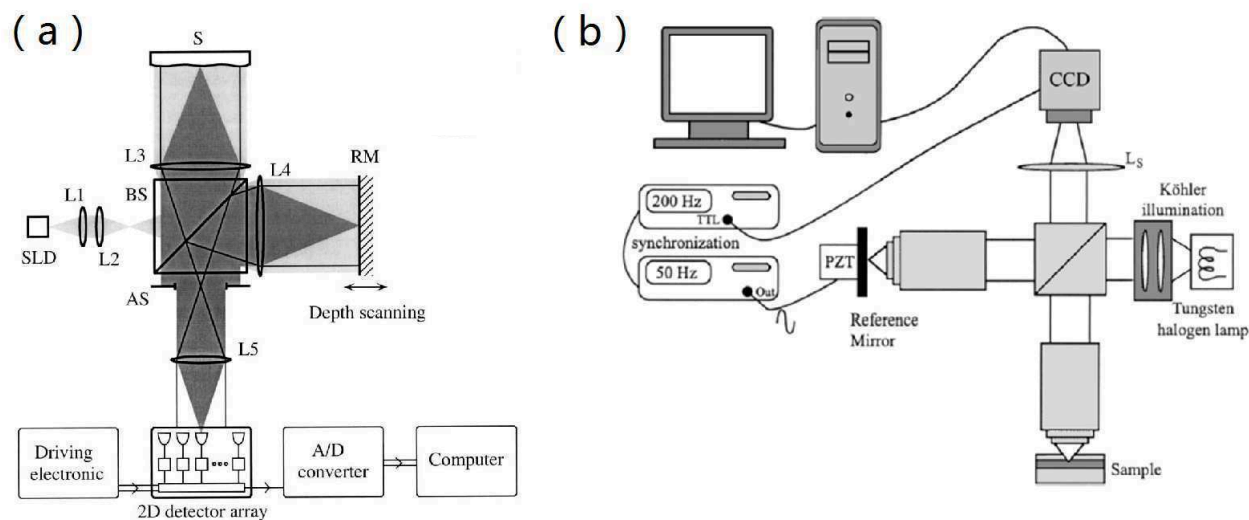


Figure 1.8 – Schematic of parallel OCT techniques. (a) Wide-field OCT with spatially coherent illumination like SLD [65]. (b) Full-field OCT with spatially incoherent illumination like halogen lamp [4].

Parallel OCT system takes *en face* images without lateral scanning. Unlike OCM technique, in which lateral scanning works with photodiode to form an *en face* image, parallel OCT enables non-scanning *en face* imaging with the planes that are perpendicular to optical axis with specific detectors and methods and achieves high pixel density images over the wide fields of view. Parallel OCT could be achieved with either spatially coherent illumination or spatially incoherent illumination. Parallel OCT system with spatially coherent light source like SLD or femtosecond laser is called wide-field OCT (WFOCT) [65–69], while the system with spatially incoherent light source like halogen lamp or LED is called full-field OCT (FFOCT) [4].

In WFOCT systems as shown in figure 1.8(a), as spatially coherent illumination is used, optical beams are usually broadened with lens to form parallel illumination on both sample and the reference mirror. *En face* images of large field could be achieved without scanning. With powerful laser sources or SLDs, WFOCT has high sensitivity. But due to the fact that spatially coherent light is used, WFOCT usually suffers strong cross-talks generated by the multiply scattered light collected by parallel detection [70–72].

The details of FFOCT system would be introduced in chapter 4, briefly speaking, as shown in figure 1.8(b), FFOCT uses spatially incoherent source in a Linnik interferometer, in which microscope objectives are used in both arms to achieve high spatial resolution. As demonstrated in [70], the cross-talks are severely reduced in FFOCT with spatially incoherent light sources. Also, due to the spatial incoherence of illumination, the spatial resolution of FFOCT is found to be insensitive to geometric aberrations, which is well established in chapter 5.

Wavefront correction with adaptive optics

Table of contents

2.1	Wavefront aberration	20
2.2	Aberration representation with Zernike polynomials	20
2.3	Strehl ratio	22
2.4	Adaptive optics (AO)	23
2.4.1	Introduction of AO	23
2.4.2	Wavefront corrector	24
	Deformable mirror	24
	Liquid crystal spatial light modulator	25
	Adaptive liquid lens	25
2.4.3	Direct wavefront sensing	27
	Shack-Hartmann wavefront sensor	27
2.4.4	Indirect wavefront measurement based on image analysis	27
	Metric-based sensorless algorithms	28
	Phase diversity	29
	Pupil segmentation	30
2.5	Computational adaptive optics	30

2.1 Wavefront aberration

Optical wavefront is an imaginary surface that connecting all the wave points with identical phase, or geometrically points with identical optical path length (OPL) from one point of the source. In a perfect optical imaging system, when the light from one point of the object could direct into a corresponding single point on the detection plan after passing through all the optics, it is usually called a diffraction-limited imaging system in which flat wavefront are formed in the pupil plan. But in realistic imaging systems, due to the imperfection of optical elements or the inhomogeneity of light propagating medium, optical wavefront could be distorted, resulting in blurring of the image. These causes of the departure of the optical wavefront from the predictions of paraxial optics is called optical aberrations or wavefront aberrations.

Technical developments have helped to remove most of the optical element-induced aberrations in imaging systems. Multi-element objectives are used to remove both monochromatic and chromatic aberrations in microscopy. Non-planar folding of the off-axis spherical mirror [73], toroidal mirror [74] or off-plane design of reflective optics [75] has also been implemented in retinal imaging systems to reduce system induced aberrations. But sample-induced wavefront aberration is still another challenge for optical imaging. Wavefront distortions could be induced by the atmosphere turbulence in telescope imaging, the structure heterogeneity of biological sample in deep tissue imaging, the curvature irregularities of the cornea and lens or eye diseases in human eye imaging, etc.

2.2 Aberration representation with Zernike polynomials

It is needed to mathematically represent wavefront aberrations in order to evaluate their effects on imaging. Due to the complicity of a wavefront surface, polynomials are typically used to simplify the description. And the commonality of circular apertures in telescopes and lens makes treatment in polar coordinates more preferable. Zernike polynomials is one of the most commonly used orthonormal polynomials over circular pupils that have been widely used in astronomy and in vision for wavefront aberration representation [76–79].

Any wavefront aberration function could be decomposed into a linear combination Zernike polynomials as

$$W(r, \theta) = W(R\rho, \theta) = \sum_{i=0}^{\infty} c_i Z_i(\rho, \theta) \quad (2.1)$$

in which $W(r, \theta)$ is the wavefront aberration with circle pupil size of R , ρ is the normalized pupil radius $\rho = r/R$, $Z_i(\rho, \theta)$ are a set of Zernike polynomials and c_i are the i th Zernike coefficient which determine the weight of each Zernike mode in the overall wavefront structure. Owing to the orthonormality, c_i could be calculated by

$$c_i = \frac{1}{\pi} \int_0^{2\pi} \int_0^1 W(R\rho, \theta) Z_i(\rho, \theta) \rho d\rho d\theta. \quad (2.2)$$




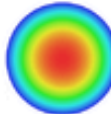
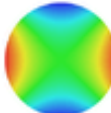
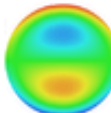
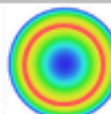
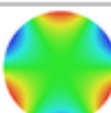
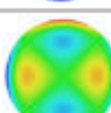
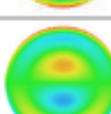
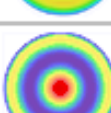
#	ZERNIKE TERM	ZERNIKE ORTHOGONAL CIRCLE POLYNOMIAL	Name	WF Map w/ANSI sign PEAK  VALLEY
0	Z_0	1	PISTON	
1	Z_1	$2\rho\cos\theta$	DISTORTION/TILT	
2	Z_2	$2\rho\sin\theta$		
3	Z_3	$\sqrt{3}(2\rho^2-1)$	DEFOCUS/FIELD CURVATURE	
4	Z_4	$\sqrt{6}(\rho^2\cos 2\theta)$	PRIMARY ASTIGMATISM	
5	Z_5	$\sqrt{6}(\rho^2\sin 2\theta)$		
6	Z_6	$\sqrt{8}(3\rho^3-2\rho)\cos\theta$	PRIMARY COMA	
7	Z_7	$\sqrt{8}(3\rho^3-2\rho)\sin\theta$		
8	Z_8	$\sqrt{5}(6\rho^4-6\rho^2+1)$	BALANCED PRIMARY SPHERICAL ABERRATION	
9	Z_9	$\sqrt{8}\rho^3\cos 3\theta$	ELLIPTICAL COMA (ARROWS, TREFOIL)	
10	Z_{10}	$\sqrt{8}\rho^3\sin 3\theta$		
11	Z_{11}	$\sqrt{10}(4\rho^4-3\rho^2)\cos 2\theta$	SECONDARY ASTIGMATISM	
12	Z_{12}	$\sqrt{10}(4\rho^4-3\rho^2)\sin 2\theta$		
13	Z_{13}	$\sqrt{12}(10\rho^5-12\rho^3+3\rho)\cos\theta$	SECONDARY COMA	
14	Z_{14}	$\sqrt{12}(10\rho^5-12\rho^3+3\rho)\sin\theta$		
15	Z_{15}	$\sqrt{7}(20\rho^6-30\rho^4+12\rho^2-1)$	SECONDARY SPHERICAL ABERRATION	

Figure 2.1 – First 15 Zernike circle polynomials and their surface map representations [80].

The orthonormality of Zernike polynomials is defined as

$$\frac{1}{\pi} \int_0^{2\pi} \int_0^1 Z_i(\rho, \theta) Z_j(\rho, \theta) \rho d\rho d\theta = \delta_{ij} \quad (2.3)$$

in which δ_{ij} is the Kronecker delta. $\delta_{ij} = 1$ when $i = j$; otherwise, $\delta_{ij} = 0$.

Figure 2.1 shows the first 15 Zernike circle polynomials, as shown in the formulas of different Zernike polynomials, higher-order polynomials is balanced with lower-order polynomials so that each Zernike polynomials gives a minimum variance. And the orthonormality of ensures that we can truncate the Zernike modes to lower orders without affecting the remaining Zernike coefficients. All the Zernike modes except for piston have a mean of zero.

To quantify the similarity of the aberrated wavefront to a reference flat wavefront, the wavefront error σ (or root mean square (RMS)) of the wavefront aberration for a circular pupil is used and can be expressed as

$$\sigma^2 = \frac{1}{\pi} \int_0^{2\pi} \int_0^1 (W(R\rho, \theta) - W_0(R\rho, \theta))^2 \rho d\rho d\theta. \quad (2.4)$$

Since the reference is considered to be flat and equal to zero, and if the aberrated wavefront is decomposed by Zernike polynomials, according to equation 2.1 and 2.2, the wavefront error could be calculated as

$$\sigma^2 = \frac{1}{\pi} \int_0^{2\pi} \int_0^1 \left(\sum_{i=0}^{\infty} c_i Z_i(\rho, \theta) \right)^2 \rho d\rho d\theta = \sum_{i=0}^{\infty} c_i^2. \quad (2.5)$$

This equation is commonly used to give a parameter for the image quality with a given wavefront aberration, especially for ocular aberrations. And typically the coefficients for piston and tilt ($i = 0, 1, 2$) are ignored as this do not change the image quality.

2.3 Strehl ratio

Beside of the wavefront error σ , Strehl ratio is another parameter that gives information about the degradation of image quality of wavefront aberrations. Strehl ratio S is defined as the the ratio of the "best focus" image intensity from a point source in the presence of aberrations compared to its maximum diffraction-limited intensity using an ideal optical system without aberrations. Thus the Strehl ratio has a value between 0 and 1, and mathematically can be expressed as

$$S = \frac{1}{\pi^2} \left| \int_0^{2\pi} \int_0^1 e^{i2\pi\Delta W(\rho, \theta)} \rho d\rho d\theta \right|^2 \quad (2.6)$$

in which ΔW is the wavefront aberration relative to the reference wavefront. An estimation formula is also widely used for simple approximation of the Strehl ratio down to 0.1 expressed as:

$$S \approx e^{-\sigma^2} \quad (2.7)$$

in which σ is the wavefront error defined by equation 2.4. Based on the Maréchal criterion [81], system could be considered as aberration-free when the Strehl ration is bigger than 0.8, which corresponding to a wavefront error $\leq \lambda/14$.

2.4 Adaptive optics (AO)

2.4.1 Introduction of AO

Adaptive optics (AO) is a kind of technology, rather than an imaging system, that can be used in combination with imaging modalities to dynamically sensing and compensating the wavefront aberrations induced by systems or samples to improve the optical image quality. Based on the general definition, AO is actually far more common in our daily life, for example, the human eye itself is an adaptive system that could alter the pupil size and lens curvature to form good images on the retina, or the autofocus function in every cellphone camera with internal control loops. The concept of AO was first proposed in 1953 by Horace W. Babcock [82] and originally applied to astronomical telescopes [83] for correcting wavefront distortions induced by atmosphere turbulence due to the variations of refractive index in different layers. Compared with sending imaging systems to outer space to get rid of the aberration effects, AO coupled telescopes are more cost-efficient and can also achieve resolution close to diffraction-limit.

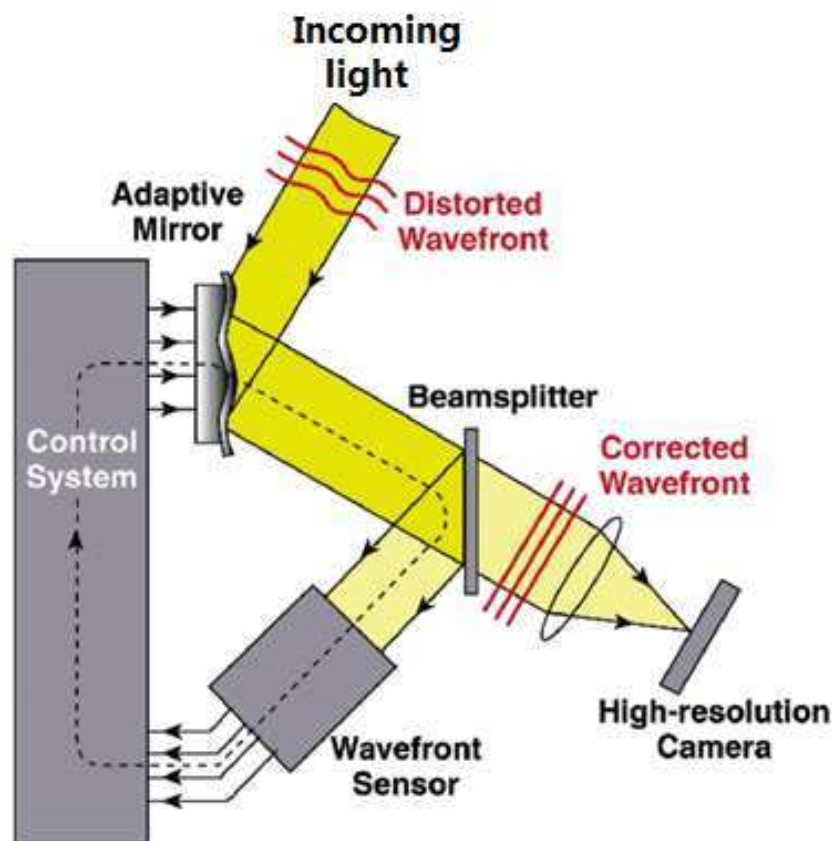


Figure 2.2 – Simplified schematic of a basic adaptive optics system in an optical imaging system [84].

Beside of its indispensable application in astronomical imaging, AO has actually played a significant role in various biological imaging areas to improve image quality. Although the modern optical systems could be almost perfect, aberrations could still come from the imperfect assembly of customized systems, the inhomogeneity of imaging medium and also the sample

itself. Particularly in retina imaging, as optical wavefront need to pass the anterior part of the eye, from where most of the ocular aberration is induced, AO is essential in many *in vivo* retinal imaging modalities like fundus camera [85], scanning laser ophthalmoscopy (SLO) [86] and OCT, which will be discussed in section 3.1.2, to achieve better resolution.

Figure 2.2 shows a simplified schematic of the AO part for an optical imaging system. The incoming light is aberrated with distorted wavefront. Reflected by an adaptive mirror (deformable mirror), the light is then split by a beamsplitter with part of it going to the wavefront sensor and the rest to the high resolution camera. The wavefront aberration is measured by the sensor and through the control system the measured aberration is inversely applied to the adaptive mirror to correct the distorted wavefront. Thus the corrected wavefront would go to the imaging system to form high resolution images. The main part of an AO system is the wavefront corrector for aberration correction and the wavefront sensor for aberration determination. Of course many wavefront sensorless methods have also been developed, which will also be discussed.

2.4.2 Wavefront corrector

As a key part of an AO system, wavefront corrector works by altering the OPL to delay the leading parts of the aberrated wavefront so that the trailing parts could catch up to form a flat wavefront. Based on the way of changing the OPL, wavefront correctors can be briefly divided into two catalogues: changing the physical shape of the reflective surface like deformable mirrors; and altering the refractive index by transmissive devices like liquid crystal spatial light modulators or adaptive liquid lens. Depends on the nature of aberrations being corrected, imaging system requirements and correction accuracy, different wavefront correctors have their own pros and cons.

Deformable mirror

Up to today, many kinds of deformable mirrors have been developed and used in AO systems. The earliest implementation is segmented mirror [87] that are made by a number of closely assembled small mirrors with square, hexagonal or circular shapes. Each segment is controlled separately with actuators that are able to perform piston-only (figure 2.3(a)) or piston with tip and tilt (figure 2.3(b)) motions. Segmented mirrors are able to approximate the wavefront correction with relatively large number of segments, but the discontinuity between segments would induce discontinuous phase correction to the incoming wavefront that will weaken the correction performance. Also the gap between different segmented mirrors would cause energy lose and light scattering due to the diffraction form the edge of the segments. These problems are solved by deformable mirrors with continuous surface (figure 2.3(c)).

Deformable mirrors with continuous surface also work with physical deformations to match the required wavefront correction shape. While the reflecting surface is continuous, the devices that perform the deformation can be either continuous like in membrane mirror [88] or bimorph mirror [89], or discrete like in edge-actuated deformable mirror [90].

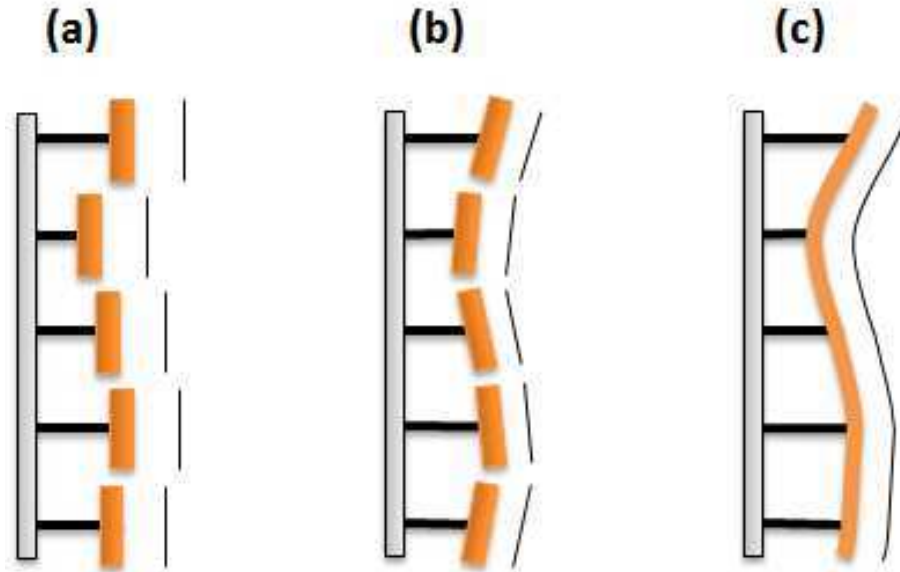


Figure 2.3 – Simplified schematic of different deformable mirrors and the wavefront representation. (a) Segmented mirror that has piston-only actuators; (b) Segmented mirror that has piston with tip and tilt actuators; and (c) Deformable mirror with continuous reflective surface.

Liquid crystal spatial light modulator

Liquid crystal spatial light modulators (LCSLM) are operated by altering the orientation of liquid crystals with electrostatic forces to change the refractive index of different pixels independently. The phase or amplitude or both of the wavefront could be varied in either a transmissive or reflective way. As the performance of LCSLM is wavelength and polarization dependent, its application is limited to small bandwidth polarized light. But as the pixels of LCSLM can be very small and independent, it can achieve high-order aberration corrections with large number pixels and a low control voltage. Although the phase modulation range is confined from 0 to 2π , aberration correction for larger dynamic range could be achieved by phase wrapping techniques [91].

In our work on the AO-FFOCT, we choose to use a transmissive LCSLM [92] as it fits perfectly for our simplified AO-FFOCT system, which will be discussed in details in chapter 6. The LCSLM is a transmissive hexagonal array SLMs (figure 2.4(a)) achieves more than 90% transmittance with 127 pixels of anisotropic nematic liquid crystal molecules that are aligned with their long axes parallel, but with their centres randomly distributed as shown in figure 2.4(b). With no voltage applied, the liquid crystal molecules lie parallel and maximum retardation is achieved. When voltage is applied, liquid crystal molecules begin to tip perpendicular causing a reduction in the effective birefringence and hence, retardance.

Adaptive liquid lens

Adaptive liquid lenses are transmissive wavefront correctors based on the physical change of the liquid lens shape and have the advantages of intrinsic smooth continuous interface, adaptively tunable optical power, polarization insensitive and also vibration resistance with two density-matched liquids employed. Using the electrowetting [93] or dielectrophoretic [94] phenomena,

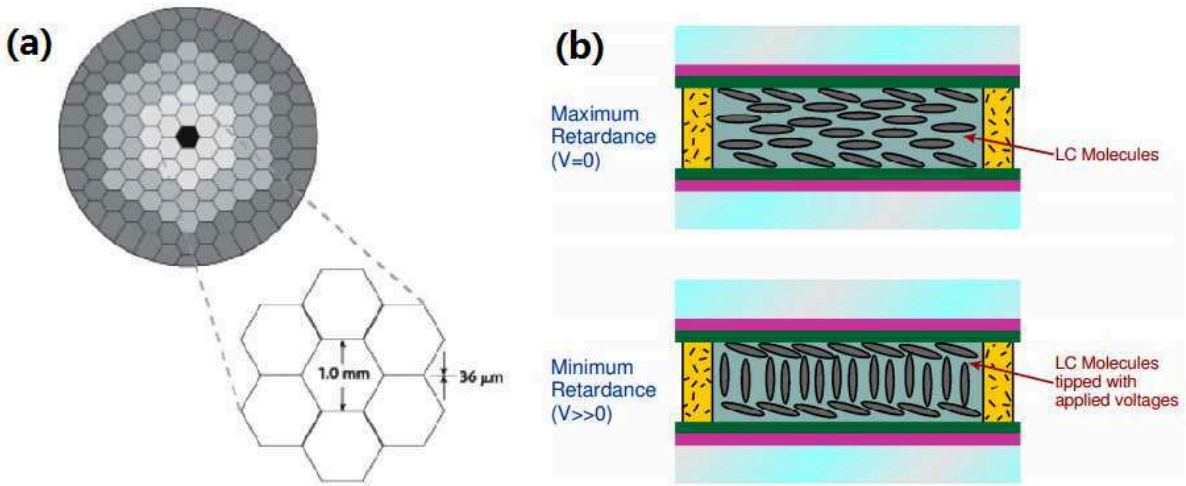


Figure 2.4 – Transmissive liquid crystal spatial light modulator [92]. (a)Hexagonal SLM pixel geometry with 127 pixels; (b)Liquid crystal variable retarder construction showing molecular alignment without and with applied voltage.

the interface properties between two immiscible liquids could be altered to change the liquid lens curvature. This could also be achieved by applying a hydraulic pressure in one of the chamber to displace the liquid and bend the deformable membrane (figure 2.5), which is used to separate the two liquids. Many methods have been proposed to generate the required pressure such as thermal, electromagnetic, electrostatic, piezoelectric actuators and so on [95–98]. Adaptive liquid lenses are relatively new technology and are promising in many applications like cellphone cameras and vision sciences.

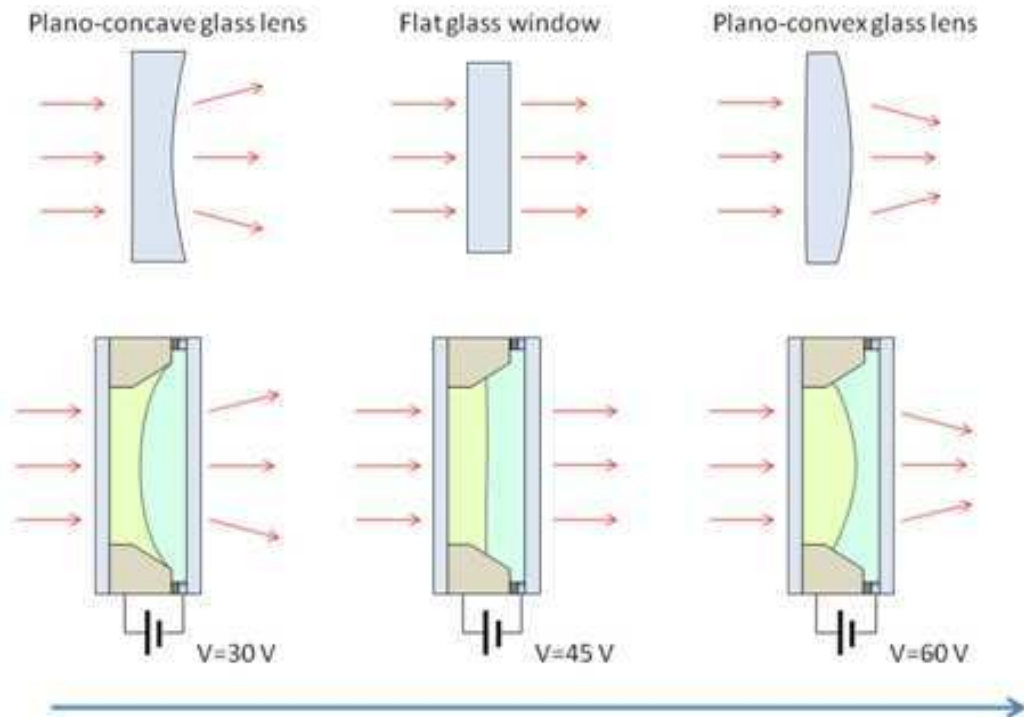


Figure 2.5 – Adaptive liquid lens curvature changes [99]. By adjusting the voltage, the hydraulic pressure is altered to bend the deformable membrane.

2.4.3 Direct wavefront sensing

Wavefront sensing deals with the aberration determination. Many AO systems nowadays do have a way to sense the optical wavefront directly with enough spatial resolution and speed to apply a real-time correction with wavefront correctors. There are various kinds of direct wavefront sensing techniques have been developed such as curvature sensing [100,101], pyramid wavefront sensor [102,103], coherence-gated wavefront sensing [104,105]. Beside these, Shack-Hartmann wavefront sensor is probably the simplest in concept and most widely used in both astronomy and ophthalmology applications.

Shack-Hartmann wavefront sensor

Invented in 1971, the Shark-Hartmann wavefront sensor is an optical system derived from the Hartmann method [106] for a number of measurements like human eye aberration determination, laser beam quality evaluation, and astronomical aberration measurement. As shown in figure 2.6 Shark-Hartmann wavefront sensor is composed of a 2D array of miniaturized lenslets that is placed in front of a detector at a distance equal to the focal length of the lenslets. Typically, the lenslets array is conjugated with the pupil plane of an optical system. When there is no aberration, the wavefront arriving at the lenslets array is planar thus the incoming light is formed into many small spots onto the detector as shown in figure 2.6(a). When aberration presents, the small spots focused on the detector is shifted from the center optical axis position as shown in figure 2.6(b). These displacements of the small spots corresponding to the local slope of the wavefront arriving at the lenslets. With centroid algorithm [107] and wavefront reconstruction method [108], the wavefront within the subaperture could be estimated.

2.4.4 Indirect wavefront measurement based on image analysis

The performance of direct wavefront measurement in AO systems could be limited by many sources of errors such as the accuracy of the wavefront sensor, non-common path errors, back reflection from lens based systems, etc. Also the lack of guiding star in many situations makes wavefront measurement ambiguous as the wavefront sensor would response to all the light impinging upon it and one cannot be sure whether the measured wavefront corresponds to the aberration that are induced to the light coming from the focal plan. For these reasons, Indirect methods that rely on the optical image itself, which is formed by the light coming from the focal plan, as the source for wavefront measurement has been developed. The basic principle is to use the effects of aberrations on the image to optimize the image quality. With a wavefront corrector in the optical beam path, known aberrations are generated before images are recorded. By analysing how the additional known test aberrations changes the image quality, optimization could be achieved by various algorithms to decide the best aberration correction parameters for wavefront corrector. In contrary to the direct wavefront measurement which invariably adds extra hardware like Shack-Hartmann wavefront sensor, indirect methods needs only the wavefront corrector. Up to today, methods like metric-based sensorless algorithms, phase diversity and pupil segmentation have been developed and applied to various applications like microscopy or OCT.

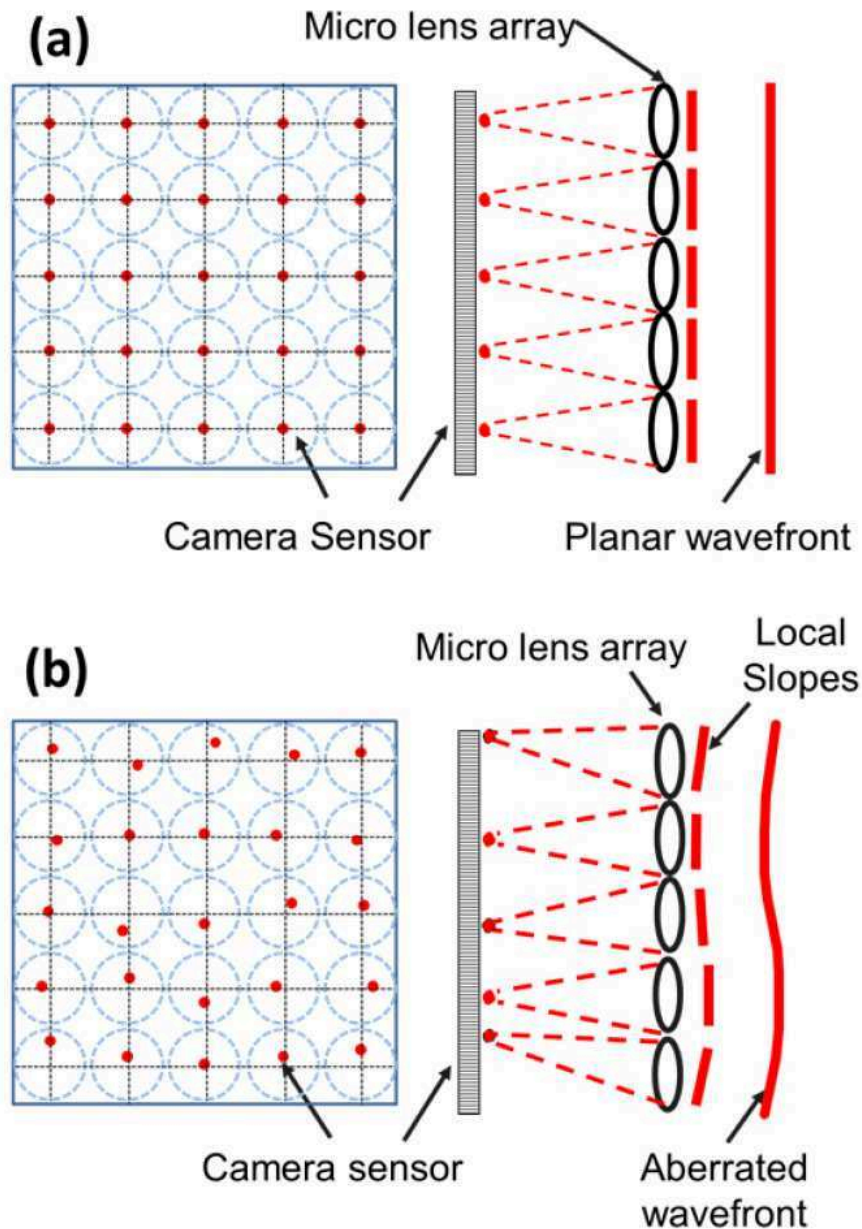


Figure 2.6 – Principle of operation of a Shark-Hartmann wavefront sensor [109]. The wavefront spot patterns produced by a planar wavefront (a) and by an arbitrarily aberrated wavefront (b). The blue dotted circles represent the lenslets.

Metric-based sensorless algorithms

The concept of metric-based sensorless algorithms, or sensorless AO, is actually analogue to what people do when adjusting a microscope for focusing. While adjusting the distance between the objective and specimen, the operator is actually evaluating the imaging quality based on the intrinsic appreciation of good image, which should be sharp and reveal enough details and contrast, until the image quality is maximised. Although the process is subjective, it is still a search algorithm in which the distance change works as an input that alters the image metric until it is maximized. In sensorless AO, the variable input could be all the aberration modes like defocus, astigmatism, coma, spherical, etc. Various type of aberration modes could be applied with a wavefront corrector in the system. The image metric is defined mathematically as the contrast, total intensity, or parameters of interested image regions. The choice of different

optimization algorithms in sensorless AO actually leads to considerable differences in their performance. Briefly, these approaches can be divided into two categories: model-agnostic algorithms and model-based algorithms.

Model-agnostic algorithms are designed to solve problems with very little background and no theoretical model is available for describing how aberrations will affect the functional image metrics. Methods like hill-climbing [110], genetic search [111, 112], conjugate gradient methods [113], etc. have been developed and applied to microscopy and imaging. The drawback of these methods is that they require large number of measurements for optimization and still may not be able to achieve the global optimum.

Model-based algorithms have been implemented in a range of imaging techniques [114–117] since the effects of aberrations on the imaging process can be modelled using theory or through empirical observations. Still these algorithms are metric-based, but in contrast to model-agnostic algorithms, the imaging model is used here to determine an orthogonal set of test aberration modes which affects the metric independently, allowing the determination of the optimum aberration correction with few test images per modes. Zernike polynomials are the most widely used approach as the orthogonality ensures that the parameters of each modes are determined independently, leading to non-iterative operations. The metric of test images could be approximated by quadratic, Gaussian or Lorentzian functions to define the optimum parameters. Figure 2.7 shows an example of the general procedure of model-based algorithms. The algorithm we applied to our AO-FFOCT system for low order aberration correction is also a model-based wavefront sensorless algorithm which will be discussed in section 6.3.

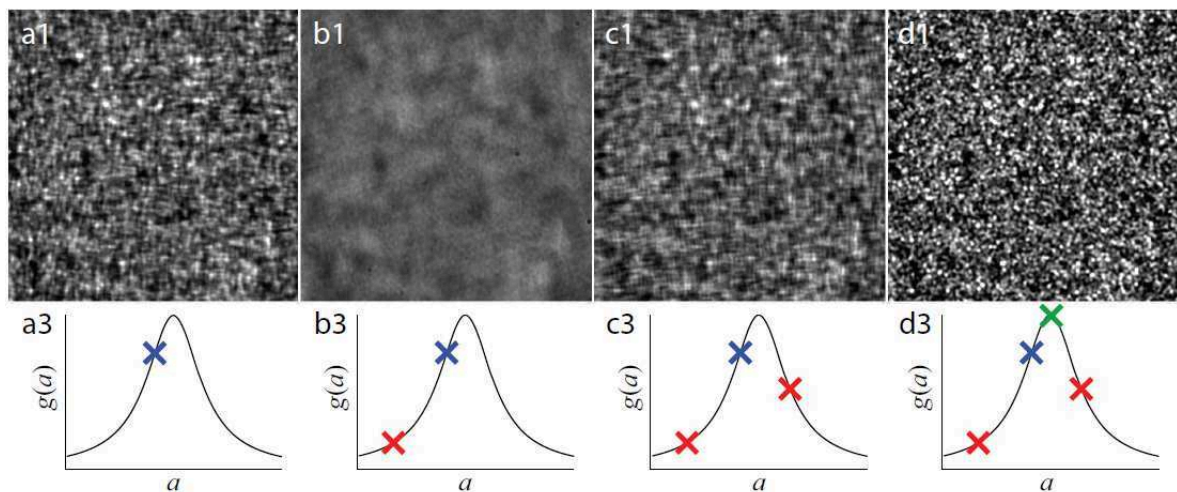


Figure 2.7 – General procedure of model-based algorithms [118]. Three test images of speckle patterns (a1, b1, c1) while changing the parameters of one specific aberration mode are taken. The respective metric values are calculated (a3, b3, c3) and modelled metric curve (black solid line) allows the determination of the optimal parameter for this specific mode (d1, d3). Some procedures could be applied to the other orthogonal aberration modes.

Phase diversity

In phase diversity method, a small set of test images are recorded with different test aberrations (phase-only) added. The actual aberrations, which are coherent with all the test images, are determined with phase retrieval algorithms. Instead of relying on a single metric, the full

information content of different images is combined to find the most likely form of all the aberration modes. The exact implementation of phase diversity varies such as the heuristic approaches in electron microscopy [119] or wide-field microscopy [120] and also a maximum likelihood approach in astronomical applications [121, 122].

Pupil segmentation

For pupil segmentation [123], instead of using a phase modulation, the test aberration is a spatial amplitude modulation. By exciting fluorescence through various subregions of the microscopy objective pupil and acquiring separate fluorescence images, the lateral shift of the signal could be acquired, which gives an estimation of the average wavefront tilt of that subregion. Simply speaking, it is an inverse Hartmann test. A more recent pupil segmentation method called zonal-based approach [124, 125] uses full-pupil illumination and takes total intensity as the metric while performs sequential 2D tip-tilt scans of different segments of the wavefront to determine the optimal condition.

2.5 Computational adaptive optics

Besides the AO techniques discussed in former section that wavefront shaping could be done with many hardware methods, it is also possible to do wavefront correction computationally. It has been shown that using interferometric detection, the complex optical wavefront could be measured. Thus the phase of the wavefront could be modified computationally. Analogous to what people do with a wavefront corrector, computational AO modifies the wavefront by adding different phase filters to the original data. And the similar methods to hardware AO with image metrics, wavefront sensor or guiding stars have also been performed in computational AO using the interferometric data [126–128]. Computational AO has been applied for high-resolution human retinal imaging in different kinds of OCT systems for aberration correction [129–131]. Note that computational AO methods are mostly adapted to systems with spatially coherent illumination.

The human eye and retinal imaging

Table of contents

3.1	Imaging properties of human eye	32
3.1.1	The structure and geometry of human eye	32
	Human retina	33
3.1.2	Eye aberrations	34
3.1.3	Eye movements	36
3.2	Retinal imaging	37
3.2.1	Flood illuminated fundus camera	37
3.2.2	Scanning laser ophthalmoscope	38
3.2.3	OCT retinal imaging	39
	Ultrahigh-resolution OCT retinal imaging	40
	AO-OCT retinal imaging	41

3.1 Imaging properties of human eye

The human eye, one of the most finely tuned evolutions in the animal world, is a robust and unique organ that works as a complete imaging system. It is composed of refracting optics (cornea and crystalline lens), aperture (iris) and photosensitive detector (retina). Compared with artificial imaging systems, which are often composed of complex optical parts to ensure high imaging performance, the eye is rather simple but does great job for vision. It forms high resolution images of objects from a large field of view at different distance using transparent tissue to the retina. And the detected light signal is converted into electro-chemical impulses in neurons. The eye provides the only direct view of the central nervous system, thus it is quite interesting for early detection of retinal and possibly systemic diseases. But if we want to inversely image the retina, the optical properties of human eye impose severe constraints on how much information we can get and how well we can resolve the details. This includes the eye aberration and eye motion problems.

3.1.1 The structure and geometry of human eye

As shown in figure 3.1(a), the eye ball is a hollow and approximately spherical structure. Externally it is mostly covered by sclera, a resistant and flexible tissue that contains many collagen fibres, to protect and maintain the shape of the eye ball. While in the anterior part, it is a transparent portion that is called cornea. The cornea is avascular tissue that admits and helps to focus light when it enters the eye. Internal to the sclera, there are two layers: the choroid and the retina. The choroid lies adjacent to the sclera and contains numerous blood vessels to provide nutrients and oxygen to the other tissues. It also contains pigmented cells that absorb light and prevent it from being reflected within the eye ball. The retina, where the light is absorbed by the photoreceptors after image formation, is the neural and sensory layer of the eye ball. Structural details of human retina will be further discussed in the following section.

The light reaching the eye ball is first refracted by the transparent cornea. After the cornea, before the iris and lens, the anterior chamber is filled with a thin watery fluid called aqueous humour, that helps to maintain the shape of the front part of the eye and provides nutrients to the lens and cornea. The iris contains two types of smooth muscles, circular muscles and radial muscles, and has an opening in the centre called pupil whose size is adjustable (2 mm to 8 mm) by the muscles to control the amount of light entering the eye. The crystalline lens is a transparent, biconvex, elastic structure that works together with cornea to form images on the retina. While the cornea has a fixed optical power, the lens is an active optical component that could change its shape from time to time by ciliary body to focus objects from various

distances. After the light is refracted by the lens, it enters the posterior chamber filled with vitreous humour and then reaches the retina.

Figure 3.1(b) shows the average values of the main geometrical and optical information of human eye. Unlike most artificial system, the human eye is not a centred optical system. The ocular surfaces are not spherical in shape and they are not perfectly aligned. The visual axis is decentred around 5 degree from the geometrical axis, focusing light on the fovea area on the retina that provides the highest resolution.

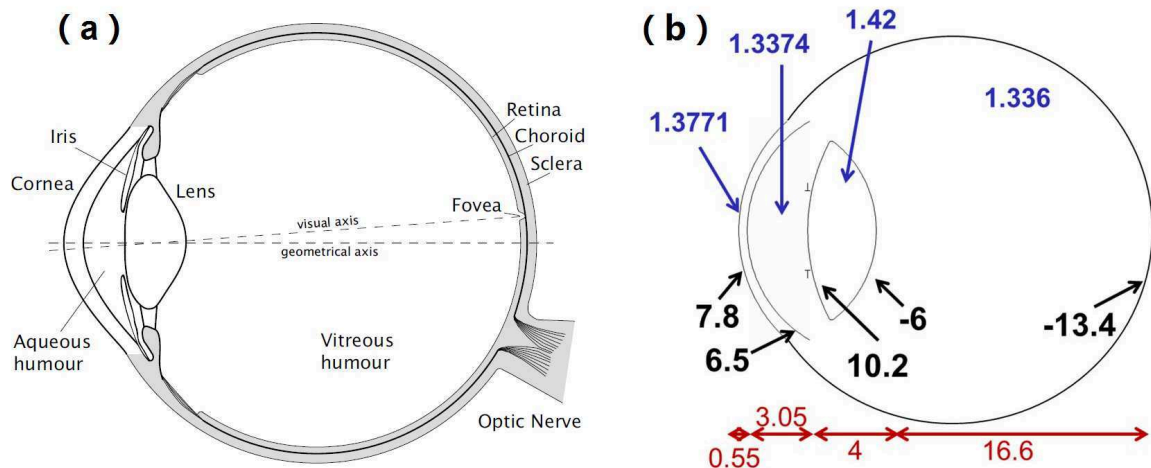


Figure 3.1 – Schematic representation of the structure and geometry of human eye [132, 133]. (a) Schematic cross-section of the human eye structure. (b) Main geometrical and optical information of human eye. Refractive indices (blue), curvature radii (black), and distance (red) in mm.

Human retina

As mentioned before, the retina is the most inner coating of the eye ball. It is a light sensitive layer that works much the same way as the film in a camera. After the image is formed on the retina layer, the light striking the retina initiates a cascade of chemical and electrical events that ultimately trigger nerve impulses. These are sent to various visual centres of the brain through the fibres of the optic nerve.

Figure 3.2 shows a cross-sectional representation of the layer structures of retina. From the direction of the incoming light, the inner limiting membrane separates the retina from the vitreous humour. The retinal nerve fibre layer (RNFL) lies immediately after the membrane. RNFL contains axons of the ganglion cells that form the optic nerve. The nerve fibres are converged and leave the eye through optical disc, which is a blind spot as no photoreceptors lies in this area. The nerve fibres are connected to the photoreceptors via a series of complex links with ganglion, amacrine, bipolar and horizontal cells, which make up the next few layers (Ganglion cell layer, Inner/Outer plexiform layer and Inner/Outer nuclear layer) in the retina before the photoreceptors. The photoreceptor layer contains light sensing rods and cones. They are large molecule chemicals that change shape when they are energized and the energy is passed to nerve endings when relaxed. The rods are for dim light and black/white vision,

while the cones are for color vision with the combination of three different types. The central part of the fovea contains only cones which are smaller (around $2\mu\text{m}$ in diameter) and more densely packed in this region than elsewhere in the retina, giving a higher visual acuity in this region. The layers at the front of the retina are thinner or completely absent at the fovea, thus increasing the amount of light reaching the photoreceptors. The last layer of retina that lies closely to the choroid is the retinal pigment epithelium (RPE) which is a single layer of hexagonal cells of pigment bits tightly packed together. RPE is quite important in protecting retina from the damaging effects of light, maintaining the photoreceptor structure, providing energy and needed components to retina, balancing the pH, and also getting rid of damaged or dead photoreceptor cells.

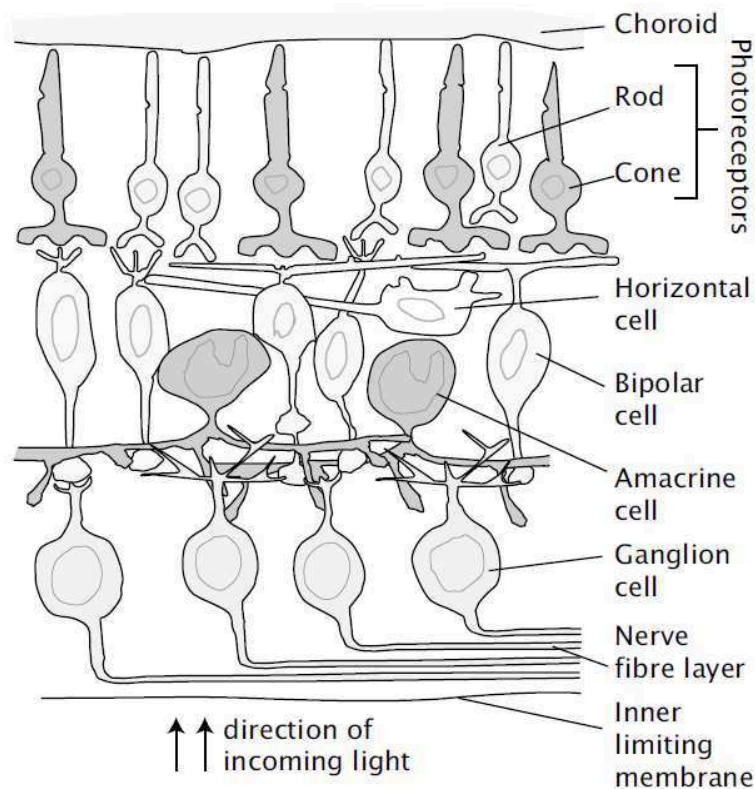


Figure 3.2 – Cross-sectional representation of retina showing the principal layers [132].

3.1.2 Eye aberrations

In an aberration-free optical imaging system like a microscope, the system resolution, or the point spread function (PSF), is limited by diffraction. With larger numerical aperture (NA), smaller PSF could be achieved. But for human eye, the first restriction is that the eye pupil size is limited to maximum 8mm , corresponding to 0.23 NA. This is not the only problem as aberration exists in every eye due to the refractive indexes mismatch in the anterior part. The benefits of increased numerical aperture of any pupil sizes larger than 3mm are defeated by the presence of aberration, which distort the PSF (see figure 3.3). Studies have shown that the balance between diffraction which blurs the image for small pupils and aberration is between $2 - 4\text{mm}$ pupils, depending on the individuals [134–136].

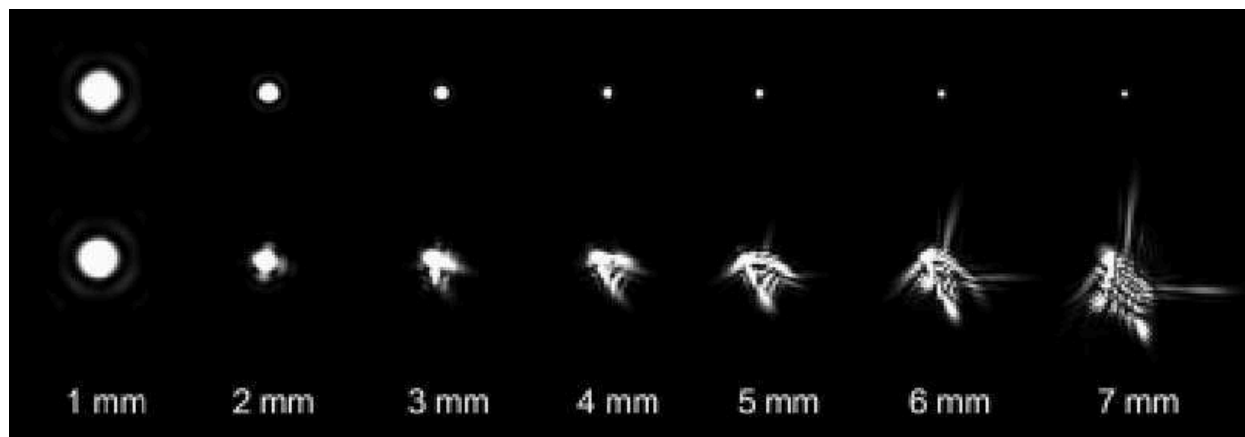


Figure 3.3 – The constraints between diffraction and aberration on the PSF of the eye [137]. The top row shows the point spread function of an eye with no aberrations. As the pupil size increases the PSF decreases in size, offering the potential for higher resolution. The lower row shows the point spread functions for an eye with typical aberrations. In this case aberrations, particularly for the larger pupil sizes, blur the PSF. The best pupil size for lateral resolution in a typical eye is between 2 – 4mm.

The magnitude of aberration is strongly dependent on individual factors such as age, state of accommodation, or the particular direction through the ocular media. It also varies spatially across the pupil, over time, and with field location in the retina. As discussed in section 2.2, with the orthogonality over circular pupils, any wavefront profile is able to be decomposed into a weighted sum of these polynomials, making Zernike polynomials the most popular representation of ocular polynomials. With the representation of Zernike polynomials, the aberration of the eye has been well characterized. Many studies on eye aberrations tests have shown that low order Zernike polynomials are actually dominating [138–141]. Figure 3.4 is the measured wavefront aberrations in large human population samples using Shack-Hartmann aberrometry by Proter et al [138] showing that the majority of the eyes' aberration lies within the low order modes such as defocus and astigmatism, which accounting for more than 92% of the total wavefront aberration variance in the eye.

Although eye is a simple optical system, it is a complex biological organ with various and continuous physical and physiological processes, resulting in the aberration of eye and the corresponding PSF being not static but fluctuate with time [141]. This is mostly due to changes in accommodation level as well as the change in shape of crystalline lens, pupil size, eye movements and the tear film. Although these micro-fluctuations might be small enough to produce perceptible effect on vision under normal circumstances, they are though to be large enough to affect retinal image quality [142]. The accommodation of the eye leads to a focus error fluctuate at a frequency around $5Hz$ [142]. The crystalline lens change would introduce fluctuations in higher-order Zernike terms with temporal frequencies of up to $2Hz$ at least [143] and the fluctuations of the eye's aberration have a non-negligible effect up to temporal frequencies of $30Hz$ [144]. The dynamic nature of the ocular aberration indicates that, instead of applying a static correction, a real-time measurement and/or correction is needed to achieve optimal correction.

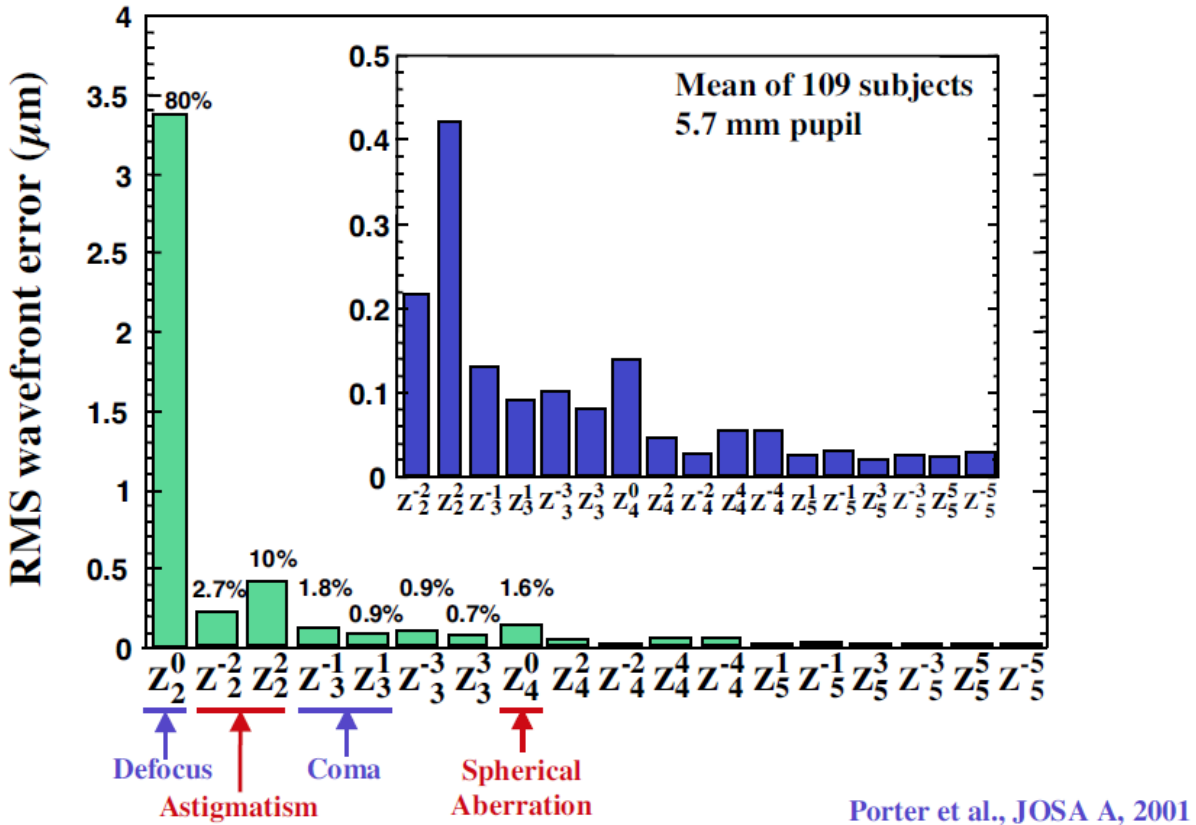


Figure 3.4 – The wavefront aberration decomposed into Zernike polynomials for a large human population over a 5.7mm pupil [138]. The percentages listed above the first eight modes represent the percentage of the variance of the wave aberration accounted for by each Zernike mode. The majority of the aberration power is found in the low order modes like defocus and astigmatism.

3.1.3 Eye movements

The human eye is constantly in motion with voluntary or involuntary movements, which move a stimulus projected onto the retina over dozens to hundreds of photoreceptors. The voluntary movements includes pursuit, the slow movement for focusing and maintaining the image on the fovea, and saccade, the renunciation of image hold on the fovea like a change in observation direction. There are also several involuntary movements like torsion, drift, tremor and micro-saccades. Torsion is the rotation of the eye ball around the axis to follow head movements. Drift is a slow movement of the eye during eye fixation. Tremor is the high frequency oscillations of the eye to maintain the image on the retina, which is also referred as physiological nystagmus. What’s more, there are micro-saccades that are fast micro movements of the eye during fixation to correct the effect of drift. The voluntary movements usually can be removed to some extend by fixation, while the involuntary movement is usually not able to stop due to people’s conscious participation and concentration. Eye movements with fixation typically still produce gaze instability of 10 or 15 arc minutes during sustained periods of attempted steady gaze [145, 146]. Table 3.1 summarizes the amplitude, speed, duration and frequency of the involuntary movements that could still exit with fixation. These movements are too small to be seen with the naked eye or with mid-level eye movement monitors, but they are a significant source of image artifact when imaging the retina with high resolution systems such as OCT or SLO. For eye

Table 3.1 – Quantitative values of involuntary eye movements [148]

	Drift	Micro-saccades	Tremor
Amplitude	2 – 5min	2 – 15min	50 – 60arcsec
Speed	6 – 30min/s	10 – 100°/s	18 – 20min/s
Duration	0.2 – 1sec	10 – 30ms	
Frequency		0.2 – 2Hz	30 – 100Hz

imaging, studies have also shown the correlation of eye axial movements with heartbeat [147]. These cardiac-induced eye movements is due to the entire head movement and could be reduced with head fixation during imaging.

3.2 Retinal imaging

The eye is one of the key elements in the vision. Thus understanding how the eye works, especially the function of the retina, is the first step towards understanding vision. By imaging and looking at retina would give much more information on how each retina component contributes to the vision. What's more, many important eye diseases as well as systemic diseases manifest themselves in the retina. The needs of retinal images at cellular level to the study and diagnosis of eye diseases are also important reasons why it is necessary to develop high resolution retinal imaging techniques. Improved retinal imaging systems that could offer better image quality would benefit dealing with all stages of various ocular diseases like glaucoma, diabetic macular edema (DME) or age-related macular degeneration (AMD). These includes the study of the causes of diseases and their progression with time, the development of a treatment for each disease, the early diagnosis of the diseases, and the treatment itself to see whether it is of a surgical nature. The anatomy of retina is well-documented with high resolution images from standard microscopes on excised sections of retina tissues. *Ex vivo* imaging of diseased retina tissues also provides useful information of the diseases and their effects on the retina. But imaging excised retina tissue could not provide direct functional information of retina. What's more, with excised retina tissue, structural changes may have already happened to various parts. Imaging excised retina tissue is also not possible to follow the development of a disease, thus plays no role in the disease diagnosis and treatment. All these reasons have pushed on the development of *in vivo* retinal imaging techniques that are non-invasive, high resolution, and can operate at high imaging speed. These includes the most popular retinal imaging techniques that are being used in the hospital nowadays such as fundus camera, scanning laser ophthalmoscope(SLO), and optical coherence tomography(OCT). And the requirements of high resolution images have also been achieved with the combination of these technique with AO techniques discussed in chapter 2.

3.2.1 Flood illuminated fundus camera

The development of fundus camera could be dated back to 1800s with the first concept introduced in 1823. In 1851, Hermann von Helmholtz introduced the Ophthalmoscope. Nowadays, fundus camera is a specialized low power microscope with an attached camera. It works by

capturing a photography of the posterior chamber of the eye that could show the structures of the central and peripheral retina, retinal vessels, optic disc and macula (see figure 3.5(a)). Through the retinal fundus photography, the appearances of retinal diseases could be visualized such as the damage to the optic nerve by glaucoma (figure 3.5(b)) or the damage to the retinal blood vessels from diabetes (figure 3.5(c)). With technology development, fundus camera can also be performed with colored filters, or with specialized dyes including fluorescein and indocyanine green. Fundus camera is first retina imaging system that was coupled with AO system to improve the image quality. The first *in vivo* images of cone receptors using a high resolution flood illuminated fundus camera is achieved in 1996 by Miller et al [149]. After the introduction of AO into eye aberration measurement, various AO fundus camera systems have been built to image retinal structure and function in both normal and diseased eyes [150–153].

The fundus photography provides a bird's view of the top most layer, the inner limiting membrane, as well as the other underlying layers of the retina. While retina contains multiple layers that have specific functions in visual perception, different abnormalities often begin in a particular layer before spreading into the other layers. The fact that fundus camera could not offer specific depth examination of the retinal layers prevent it from offering early and accurate diagnosis of retinal diseases.

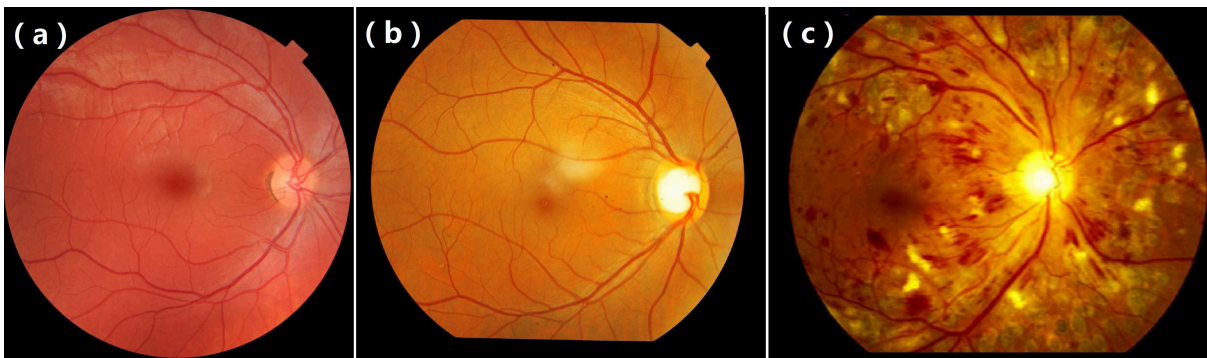


Figure 3.5 – Retinal fundus photography showing normal retina (a), glaucoma (b), and diabetes (c) [154–156].

3.2.2 Scanning laser ophthalmoscope

Scanning laser ophthalmoscope (SLO) is an eye examination method based on confocal laser scanning microscope for diagnostic imaging. By scanning a point source rapidly across the retina with horizontal and vertical scanning mirrors, raster images of specific retina areas could be created. With the reflected light passing through a pinhole that is confocal to distinct layer, SLO could resolve retinal layer structure at microscopic level. With the confocal method, reduced scattering is achieved as only light from a particular point and retinal layer is detected. And the fast scanners used in SLO make video rate imaging of retina possible.

However, due to the exists of eye aberrations, using SLO to monitor individual retinal cells is still problematic as lateral resolution would be diminished. So adding AO to SLO for wavefront correction to achieve better lateral resolution is essential to resolve cellular structure of retinal layers. The first attempt for AO-SLO is demonstrated in 1980s with a deformable mirror to correct estimated aberrations [157]. And the further invention of Shack-Hartmann wavefront

sensor has pushed AO-SLO technique to achieve much higher lateral resolution [86], larger field view [158], and the ability to visualize the distribution of cone photoreceptors around the fovea and the rod photoreceptors (see figure 3.6) [159, 160]. The imaging of Retinal Pigment Epithelium (RPE) cells in patients with and without retinal disease has also proved possible with the use of AOSLO [161]. As the loss of RPE cells represents the primary pathology of macular degeneration, this provides a possible future avenue for tracking RPE degradation *in vivo*.

Compared with other retinal imaging techniques like retinal dissection and fluorescein angiography, AOSLO is able to resolve single photoreceptor on living human retina as well as to track retina changes over time or eye movements without injecting any fluorescein dye. Although SLO provides high lateral resolution with good axial resolution, the nature that the axial resolution is dependent on the NA of the eye still limits the axial sectioning ability of SLO to around $10\mu m$.

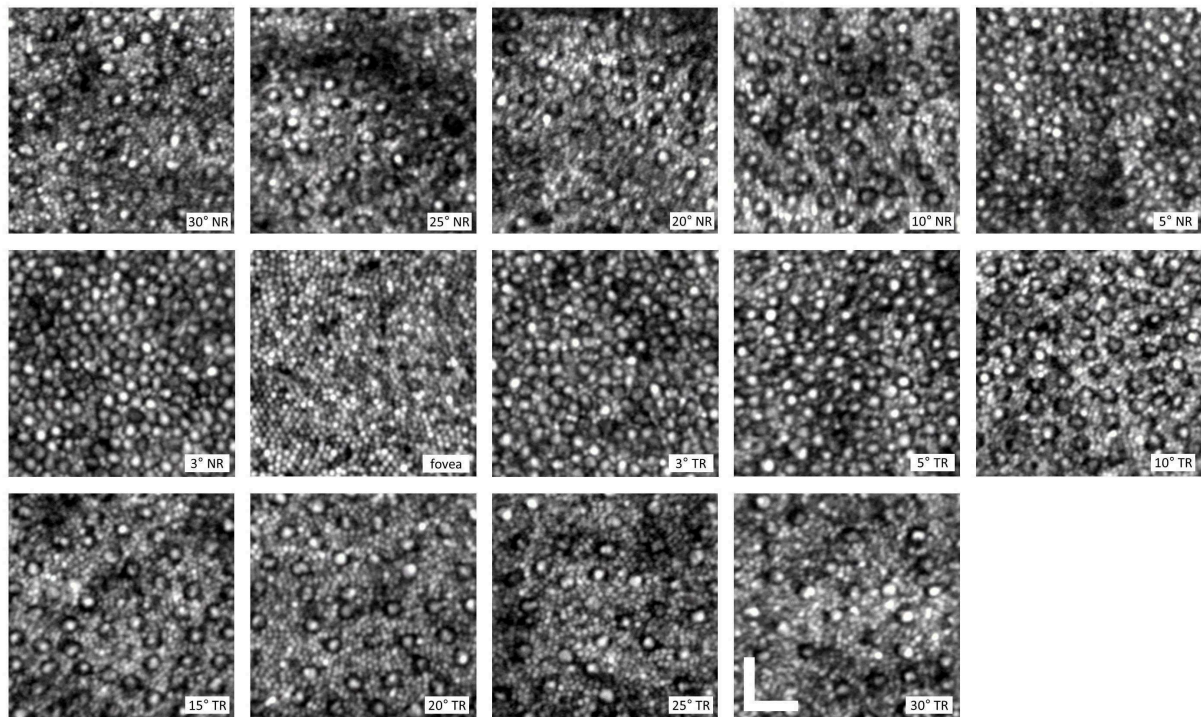


Figure 3.6 – AO-SLO images of the cone and rod mosaic at locations spanning 30° NR to 30° TR [160]. Images are displayed with a logarithmic intensity scale to enhance the visualization of the rod photoreceptors. The scale bar is $25\mu m$.

3.2.3 OCT retinal imaging

As discussed in chapter 1, OCT has emerged as a powerful imaging technology in biomedicine. It fills the gap in terms of resolution between microscopy and larger scale imaging techniques like ultrasound or MRI. With the advantages of non-contact feature, high sensitivity, and high imaging speed with micron-scale resolution, OCT has been successfully applied to ophthalmic and especially retinal imaging. OCT has significantly improved the potential for early diagnosis, understanding of retinal disease pathogenesis, as well as monitoring disease progression and response to therapy.

Ultrahigh-resolution OCT retinal imaging

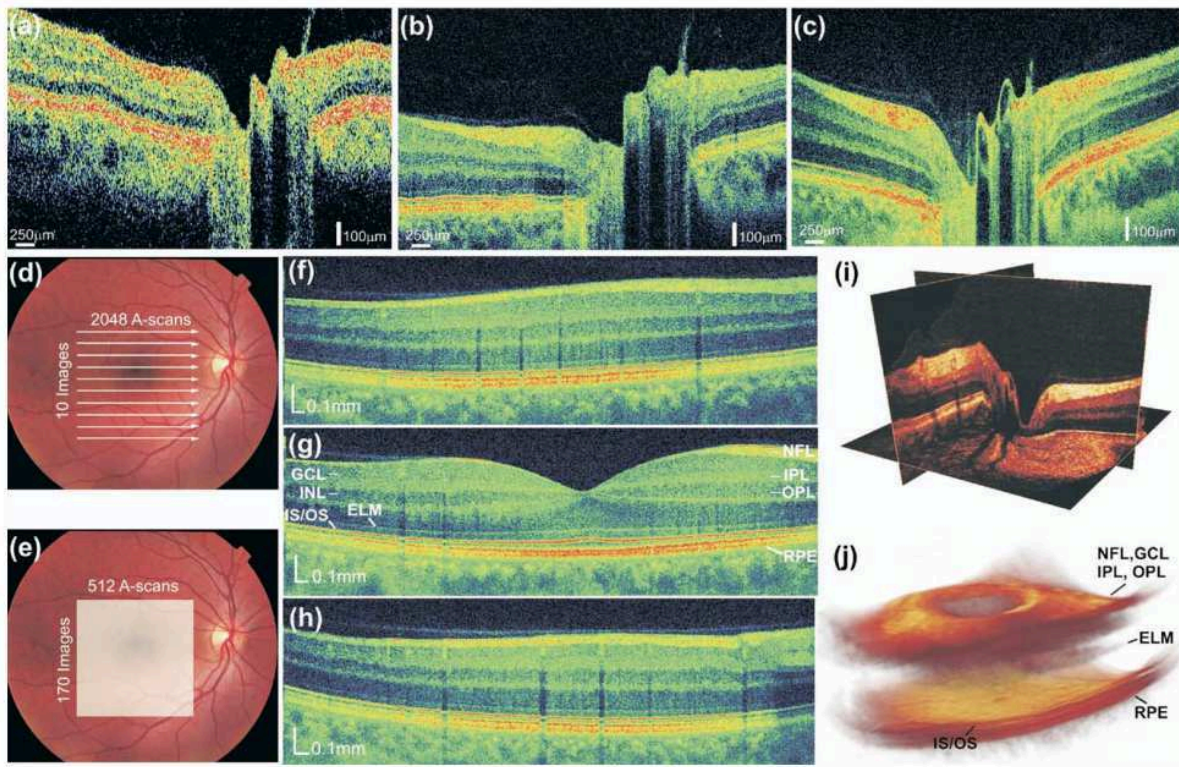


Figure 3.7 – Comparison of normal optic nerve head imaged with different optical coherence tomography (OCT) technologies [162]. (a) Standard-resolution OCT image with axial resolution of $10\mu\text{m}$, 512 transverse pixels (axial scans), acquired in 1.3 seconds. (b) Ultrahigh-resolution (UHR) OCT image with axial resolution of $3\mu\text{m}$, 600 transverse pixels, acquired in 4 seconds. (c) High-definition image using high-speed UHR OCT with axial resolution of $2\mu\text{m}$, 2048 transverse pixels, acquired in 0.13 seconds. High-speed imaging enables raster scan patterns for comprehensive 3-dimensional mapping of the retina (3D OCT). Examples of 2 different scan patterns are shown: (d) 10 cross-sectional images with 2048 axial scans (transverse pixels) each for high-definition imaging, (e) 170 images with 512 axial scans each for 3D OCT imaging, (f–h), representative high-definition OCT images of the macula, (i) representative cross-sectional images along orthogonal planes of the optic disc generated from the 3D OCT data set, and (j) volume rendering of the macula from the 3D OCT data. ELM: external limiting membrane; GCL: ganglion cell layer; INL: inner nuclear layer; IPL: inner plexiform layer; IS/OS: boundary between the inner and outer segments of the photoreceptors; NFL: nerve fiber layer; OPL: outer plexiform layer; RPE: retinal pigment epithelium.

For any kinds of retinal imaging modality, the eye itself always acts as the imaging objective. Thus, the resolutions are mostly limited by the optics of the eye. However, unlike fundus camera or SLO, in which the axial resolution is depend on the large depth of focus of the eye optics, the axial resolution in OCT is decoupled from the eye optics. The high axial resolution of OCT results from the coherent detection scheme of LCI and depends on the axial coherence length of the OCT light source. As discussed in section 1.4, the axial resolution (coherence length) is inversely proportional to the spectrum bandwidth of the light source. Development of ultrabroad bandwidth light sources and high-speed detection techniques has improved the ophthalmic OCT imaging significantly, allowing 3 dimensional ultrahigh-resolution OCT (UHR-OCT) to perform non-invasive optical biopsy of the living human retina [163–165]. The improved axial

resolution and imaging speed enable high-definition, two-dimensional tomograms, topographic thickness maps of all major intra-retinal layer as well as volumetric quantification of pathologic intra-retinal changes [166–168].

Figure 3.7 shows the comparison of the normal optical nerve head imaged by three different OCT systems: Standard OCT system ($10\mu\text{m}$ axial resolution, $400A - \text{scans}/s$, Fig. 3.7(a)), UHR OCT using time domain detection ($3\mu\text{m}$ axial resolution, $150A - \text{scans}/s$, Fig.3.7(b)), and high-speed UHR OCT using Fourier domain detection ($2\mu\text{m}$ axial resolution, $25000A - \text{scans}/s$, figure 3.7(c)). The high-speed UHR OCT not only reduces eye motion artifacts with its fast imaging speed, it also enables better delineation of the intra-retinal layers with its higher axial resolution, smaller speckle size, and increased A-line numbers.

AO-OCT retinal imaging

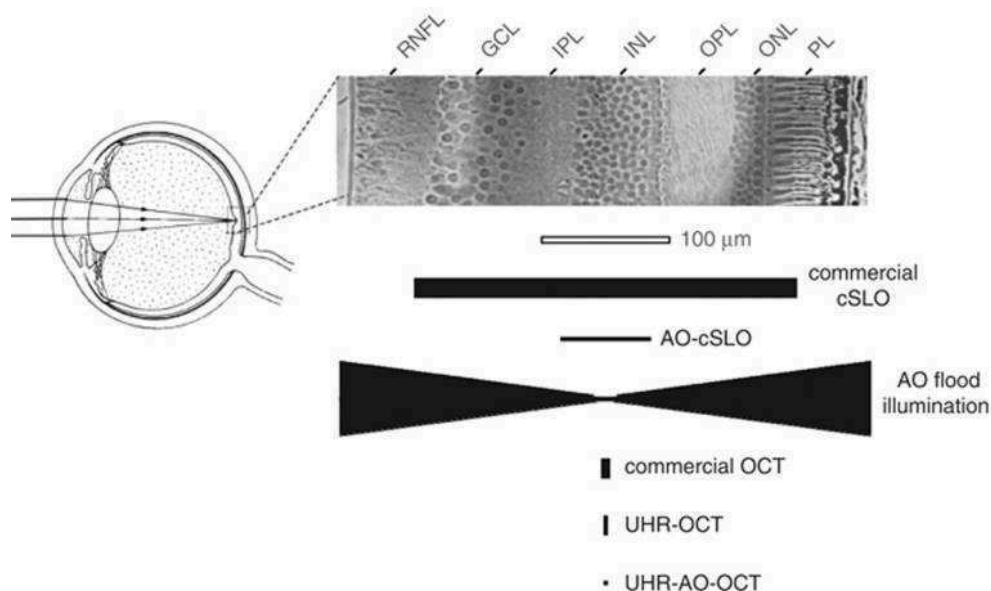


Figure 3.8 – Comparison of (top) cell size in a histological cross section of the human retina with (bottom) the resolving capability of the major types of retinal imaging modalities with and without AO [169]. The vertical and horizontal dimensions of the solid black symbols denote, respectively, the lateral and axial resolution of the instruments. Examples shown include the commercial confocal scanning laser ophthalmoscope (cSLO), confocal scanning laser ophthalmoscope with adaptive optics (AO-cSLO), flood illumination with adaptive optics, commercial OCT, ultrahigh-resolution OCT (UHR-OCT), and ultrahigh-resolution OCT with adaptive optics (UHR-AO-OCT).

High axial resolution in OCT could be achieved by using ultra-broad bandwidth light source, but the highest lateral resolution for retinal imaging is still limited by the finite size of the pupil and also the existed aberrations due to the imperfections of the eye optics (section 3.1.2). To improve the lateral resolution of retinal imaging modalities, the pupil is usually dilated to ensure the best possible diffraction limited PSF. And to compensate the limitation induced by aberrations, AO is typically combined with OCT to achieve close to diffraction-limited lateral resolution. The combination of OCT with AO permits the access to the full retinal reflection that exists a large pupil size, resulting in improving the visualization and detection of microscopic structures in the retina. Compared with commercial OCT system, AO-OCT

could have not only higher lateral resolution, but also a smaller lateral speckle size and higher signal collection efficiency. The combination of AO with high-speed UHR-OCT offers the state-of-the-art performance with an isotropic 3 dimensional resolution of $2.5 \times 2.5 \times 3 \mu\text{m}^3$ (*width* \times *length* \times *depth*) in retinal tissue. Figure 3.8 shows the comparison of the 3 dimensional resolution of various retinal imaging systems. In general, AO-UHR-OCT provides the best resolving capability currently to resolve cells in all three dimensions. Besides of the advantages offered by AO to OCT retinal imaging, AO actually brings some drawbacks. These includes the increased system complexity, physical size, and expense. Thus wavefront-sensorless [170] and also computational AO [129] have also been applied to OCT retinal imaging to get rid of some of these drawbacks.

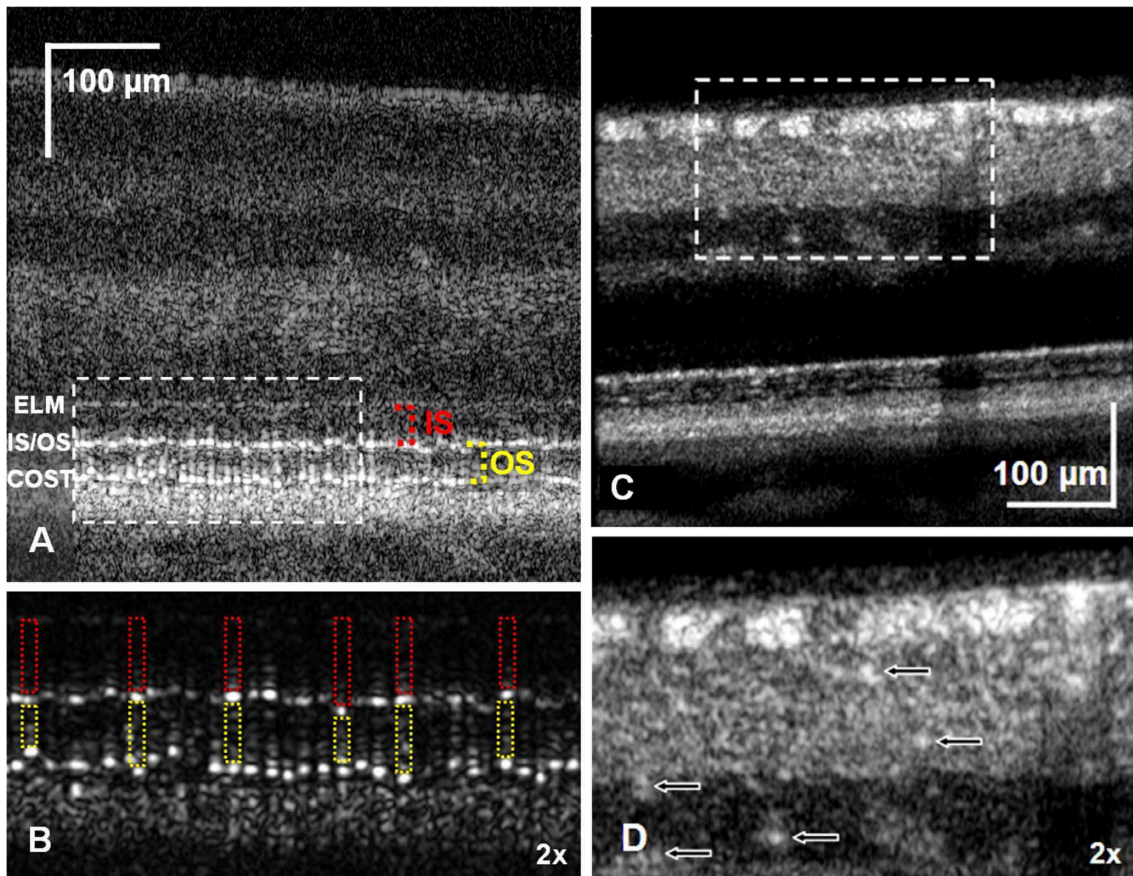


Figure 3.9 – Images acquired with AO-UHR-OCT. [171]. In a log-scale B-scan focused on the outer retina, the ELM, IS/OS, and COST bands are clearly visible, demarcating the IS and OS of the cones. In a linear-scale, magnified view (bottom left), the IS/OS and COST reflections from individual cones are clearly visible, with red and yellow boxes outlining the relatively transparent individual inner and outer segments. The width of the bright reflections is consistent with known IS widths, while their height is comparable to the axial PSF height, which suggests origination at thin reflectors. Axial displacement of neighboring reflectors is apparent in both layers. When focus is shifted to the inner retina, individual nerve fiber bundles, up to $50 \mu\text{m}$ in diameter but separated as little as $5 \mu\text{m}$, become visible. A magnified view of the latter (lower right) reveals capillaries (arrows) lying in multiple plexuses. These individual structures of the inner and outer retina appear as uniform bands in clinical OCT images.

The first implementations of AO-OCT were performed with TD-OCT using an *en face* coherence-gated OCT camera [172] and conventional TD-OCT based on tomographic scanning (xz) [173]. But the fundamental technical limits, especially in imaging speed, prevented

their application in scientific and clinical studies. In 2005, the feasibility of *in vivo* 3 dimensional cellular resolution retinal imaging were demonstrated with Fourier domain detection. The first implementation of AO with SD-OCT was by using a broadband source to illuminate a line on the retina, revealing cone photoreceptors transversely and axially [174]. Soon, a point scanning AO-OCT was developed with X-Y raster scanning system [175], which becomes a template for successive AO-SD-OCT systems. Nowadays, AO-OCT systems have been used to capture volume images of retinal structures that were previously only visible with histology. In order to demonstrate the benefit of AO correction to OCT retinal imaging, a representative AO-UHR-OCT retinal image recorded in a healthy volunteer is displayed in figure 3.9. When the focus was set to the outer retina, the zoom in to the photoreceptor layer (Figure 3.9(B)) shows a discrete spacing of high reflective spots in the IS/OS and the COST bands that correspond to individual cone photoreceptors. When shift the focus to the inner retina, individual nerve fiber bundles becomes visible. The signal originating from the RPE corresponds to a diffuse speckle pattern. Recently, with a 3D image registration and data analysis method, RPE cells were visualized and characterized in 3D with AO-OCT system [176].

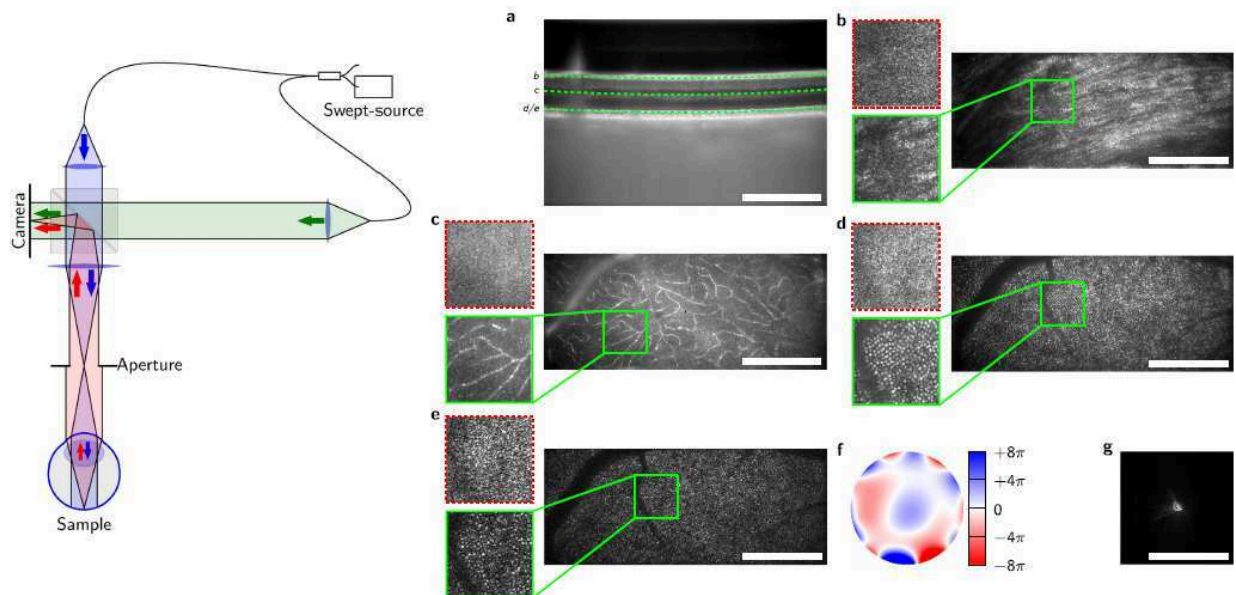


Figure 3.10 – Full-field swept-source OCT retinal imaging with computational AO [130]. (left) Setup of the full-field swept-source OCT for retinal imaging. Light from a tunable light source is split into reference (green) and sample arm (blue); the sample light illuminates the retina and the backscattered light (red) is imaged onto the camera where it is superimposed with the reference light. (right) Retinal volume acquired by FF-SS-OCT at NA 0.2 corresponding to 7mm pupil diameter after aberration removal. (a) B-scan (sectional view) from the recorded volume; the dashed green lines indicate the location of the curved en face images shown in (b–e). (b–e) Averaged (b–d) and unaveraged (e), aberration-corrected en face images with magnification of a small area in the green boxes; the same area is shown before aberration removal (dashed red boxes); nerve fiber layer (b), small capillaries (c) and photoreceptor mosaic (d,e) are only visible after correction. (f) Wavefront used for aberration correction of the green box in (d) with defocus removed. (g) Corresponding PSF. Scale bars are 0.5mm .

As discussed before, the possible diffraction-limited PSF for retinal imaging depends on the eye pupil size. Thus, in high resolution applications, *en face* OCT techniques, of which the

optical beam covers the full pupil, may be advantageous compared with scanning OCT system, which usually uses beam size smaller than the eye pupil size. *En face* OCT systems record images with planes perpendicular to the optical axis, maintaining high lateral resolution throughout the imaging depth. Figure 3.10(left) shows a recently published remarkable full-field swept-source OCT which can obtain truly coherent 3 dimensional tomograms of the living human retina with high image quality [130]. The aberrations are obtained and corrected computationally using a modal-based method with the phase information of the *en face* images. Figure 3.10(right) shows the in vivo retinal image of human eye with 7mm pupil. Without the aberration correction, the volumes were laterally blurred in all layers of the retina. With this significant image degradation, we can hardly see any lateral structures. The structure of the nerve fiber layer and small capillaries became visible and single photoreceptor cells were identified after aberration corrected computationally.

Part II

Full-field Optical Coherence Tomography and its Adaptive Optics

Full-field optical coherence tomography (FFOCT)

Table of contents

4.1	Introduction	48
4.2	Basic principles of FFOCT	48
4.2.1	Basic layout	48
4.2.2	Image acquisition	50
4.3	FFOCT performances	52
4.3.1	Resolution	52
4.3.2	Field of view	52
4.3.3	Sensitivity	52
4.3.4	Comparison of FFOCT with other OCT techniques	53
4.4	LightCT scanner	53
4.5	FFOCT applications	55
4.5.1	Histological evaluation of <i>ex vivo</i> tissues	55
4.5.2	Dynamic FFOCT imaging	56
4.5.3	Inner fingerprint imaging	57

4.1 Introduction

Full-field OCT (FFOCT) was originally developed in our lab with the conceivability of creating a high-resolution but easy-to-use OCT device [3, 4]. As discussed in chapter 1, traditional OCT systems obtain cross-sectional (B-scan) and 3 dimensional images by laterally scanning a point light source across the sample with axial measurements (A-scan) of the backscattered and back-reflected light. While in FFOCT, instead of taking images by raster scanning like traditional scanning OCT system, it takes *en face* images with planes that are perpendicular to the optical axis. Depth imaging is achieved by scanning the sample along the optical axis, thus no large depth of field is needed, allowing using large NA optics to achieve much higher lateral resolution than traditional OCT. In this way, FFOCT achieves both high axial resolution with coherence gating effect like traditional OCT and high lateral resolution with high NA objective like microscopes. Following the development of the first prototype model, subsequent improvements to the original instrument have revealed a resolution capability surpassing that of the most advanced femtosecond laser systems, but using a simple white light source [177, 178]. In FFOCT, by illuminating the entire field with a spatially incoherent source with low temporal coherence length like halogen lamps or LEDs, *en face* images is recorded with a 2 dimensional detector array such as CCD or CMOS camera. The differences of FFOCT with most optical coherence microscopy (OCM) systems and wide-field OCT (WFOCT) are that OCM and WFOCT use spatially coherent light sources. Although they all take *en face* images, OCM would also need to do raster scanning of the light focused at the required depth. The use of a spatially incoherent illumination has been proved to severely reduce the cross-talk effects in FFOCT compared with WFOCT with spatially coherent illumination [70]. Also, taking the advantage of spatially illumination in FFOCT, the lateral resolution is found to be insensitive aberrations. This has been proved both theoretically and experimentally and will be discussed in details in chapter 5.

4.2 Basic principles of FFOCT

4.2.1 Basic layout

The schematic of general FFOCT setup is shown in figure 4.1(left). Briefly speaking, it is a combination of an interferometer with a microscope. A spatially incoherent broadband light source is coupled into a Michelson interferometer in a Linnik configuration that has both microscope objectives in the sample arm and reference arm. The optical beam from the source is divided into two arms by a broadband non-polarizing beamsplitter cube: one goes to the sample and the other goes to the reference mirror. The backscattered beams are recombined and

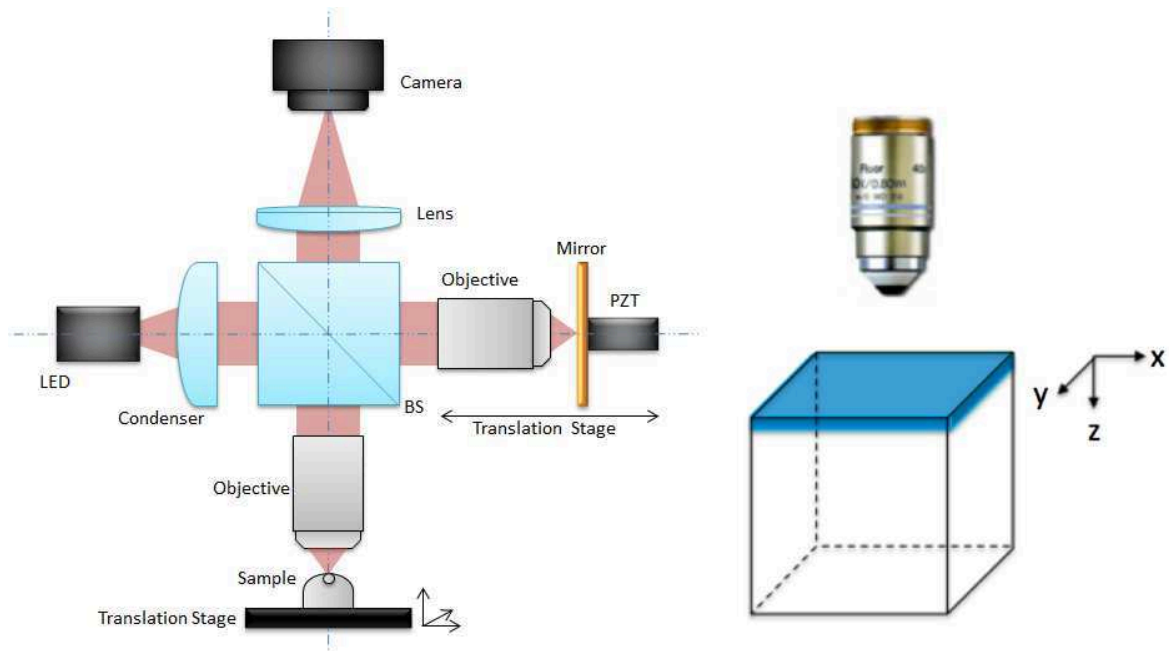


Figure 4.1 – Schematic of FFOCT. (left) Diagram of a conventional FFOCT in a Linnik interferometer. BS: beamsplitter; PZT: piezoelectric transducer. (right) Diagram showing FFOCT takes *en face* images with planes(xy) that are perpendicular to the optical axis(z).

imaged on the camera. The optical sectioning ability is from the low coherence interference of the two arms to select optical slices that are perpendicular to the optical axis (figure 4.1(right)). Interferometric amplitudes which form the FFOCT images are obtained using the combination of two or four phase shifting images by modulating the path difference with a piezoelectric transducer (PZT) in the reference arm.

The spatially incoherent light source is a key element in FFOCT as its various features would have a direct impact on the imaging performance of FFOCT. The spectral properties of the illumination light determine both the lateral and axial resolution. The wavelength also determines the depth of penetration into the samples. To maximize the imaging depth, wavelength within the near-infrared window ($650\text{nm} - 1350\text{nm}$) is typically selected to minimize the optical absorption. The optical power plays a role on the imaging speed. The spatial incoherence of the source in FFOCT not only helps to avoid cross-talks but also has a close relationship with the lateral resolution of FFOCT in case of aberration exists (see chapter 5).

The camera used in FFOCT should also be selected with great care as it is crucial for the quality of the images. Currently silicon cameras based on CCD or CMOS technologies or InGaAs cameras have been applied in FFOCT systems. Camera parameters, such as spectral sensitivity, dynamic range as well as frame rate, are of great importance for FFOCT. Silicon based cameras could not detect light with wavelength longer than $1.1\mu\text{m}$ while InGaAs cameras are sensitive to wavelength between $0.9\mu\text{m}$ and $1.7\mu\text{m}$, which would offer possibilities of better penetration in highly scattering samples [179, 180]. A high dynamic range detector is particularly important in FFOCT to resolve small modulations on a large background signal with low noise. High frame rates are extremely crucial for high speed imaging of FFOCT and plays an important role in applying FFOCT for *in vivo* imaging to damp the artifacts of sample motions.

4.2.2 Image acquisition

The broadband source used in FFOCT ensures that interference only happens within the coherence length, between the light back-reflected from the reference mirror and backscattered from the selected depth volume in the sample. FFOCT acquires *en face* tomographic images that intends to reveal the intensity of the backscattered light from the selected depth volume. The amplitude of the backscattered light could be calculated by combining two or four images taken with an imposed reference mirror modulation. The reference mirror is modulated with PZT by two or four values of the phase ψ shifted by π or $\pi/2$, respectively. The recorded signal of the direct image is given by

$$I(x, y) = \frac{I_0}{4} \{ R_{inc}(x, y) + R_{ref}(x, y) + 2\sqrt{R_{sam}(x, y) \cdot R_{ref}(x, y)} \cos[\phi(x, y) + \psi] \} \quad (4.1)$$

in which:

- ϕ is the phase difference between the sample signal and reference signal;
- ψ is the phase shift induced by the shift of the reference mirror with the PZT;
- I_0 is the photon flux of the illumination;
- R_{ref} is the reflectivity of the reference, which is rather uniform;
- R_{sam} is the reflectivity of the sample structures within the coherence volume that is conjugated to the reference mirror;
- R_{inc} is the reflectivity of all the other structures that are out of the coherence volume and other stray reflections.

With a two-phase modulation, the reference mirror is shifted corresponding to a phase shift of π . Thus the recorded signal of the two direct images would be:

$$I_1(x, y) = \frac{I_0}{4} \{ R_{inc}(x, y) + R_{ref}(x, y) + 2\sqrt{R_{sam}(x, y) \cdot R_{ref}(x, y)} \cos[\phi(x, y) + 0] \} \quad (4.2)$$

$$I_2(x, y) = \frac{I_0}{4} \{ R_{inc}(x, y) + R_{ref}(x, y) + 2\sqrt{R_{sam}(x, y) \cdot R_{ref}(x, y)} \cos[\phi(x, y) + \pi] \} \quad (4.3)$$

By subtracting the two consecutive images, we would get

$$I_1(x, y) - I_2(x, y) = I_0 \sqrt{R_{sam}(x, y) \cdot R_{ref}(x, y)} \cos[\phi(x, y)] \quad (4.4)$$

As in OCT images, speckles always exist since the interference happens with the light backscattered by different tissue structures inside the coherence volume. The amplitude and phase of the recorded backscattered signals are random. Thus, by just taking the absolute value of the real part of the resulted complex signal would still keep most of the information.

Four four-phase modulation method, the reference mirror is shifted consecutively with a phase shift of $\pi/2$, the subtraction of every other direct images results in:

$$I_1(x, y) - I_3(x, y) = I_0 \sqrt{R_{sam}(x, y) \cdot R_{ref}(x, y)} \cos[\phi(x, y)] \quad (4.5)$$

$$I_2(x, y) - I_4(x, y) = I_0 \sqrt{R_{sam}(x, y) \cdot R_{ref}(x, y)} \sin[\phi(x, y)] \quad (4.6)$$

Thus,

$$\sqrt{[I_1(x, y) - I_3(x, y)]^2 + [I_2(x, y) - I_4(x, y)]^2} = I_0 \sqrt{R_{sam}(x, y) \cdot R_{ref}(x, y)} \quad (4.7)$$

While R_{ref} is homogeneous, this result in a signal proportional to $\sqrt{R_{sam}(x, y)}$ that is the amplitude of the backscattered signal intensity.

The above methods show how single *en face* tomogram is acquired with FFOCT. Typically, multiple images is taken at the same imaging depth for averaging to improve the signal to noise ratio. To acquire 3 dimensional images, the imaging depth is shifted successively across the sample volume of interest, acquiring tomograms of different imaging depth that could reveal the 3 dimensional structure of the sample. Due to the refractive index mismatch between the imaging sample and the reference arm immersion medium, the optical coherence plane would be varied from the focal plane in the sample when only the sample is elevated to image deeper. Thus defocus would occur and lead to the degradation of the signal level. Thus, a dynamic adjustment of the two arms would be needed to match the coherence plane with the focal plane when imaging deeper. For the detailed methods, one can refer to [181, 182]. Figure 4.2 shows an example of FFOCT 3 dimensional imaging of a 5 days post fertilization (dpf) zebrafish larva embedded in agar. By taking 300 *en face* tomograms (xy plane), the entire fish is imaged and combine to form a 3 dimensional view.

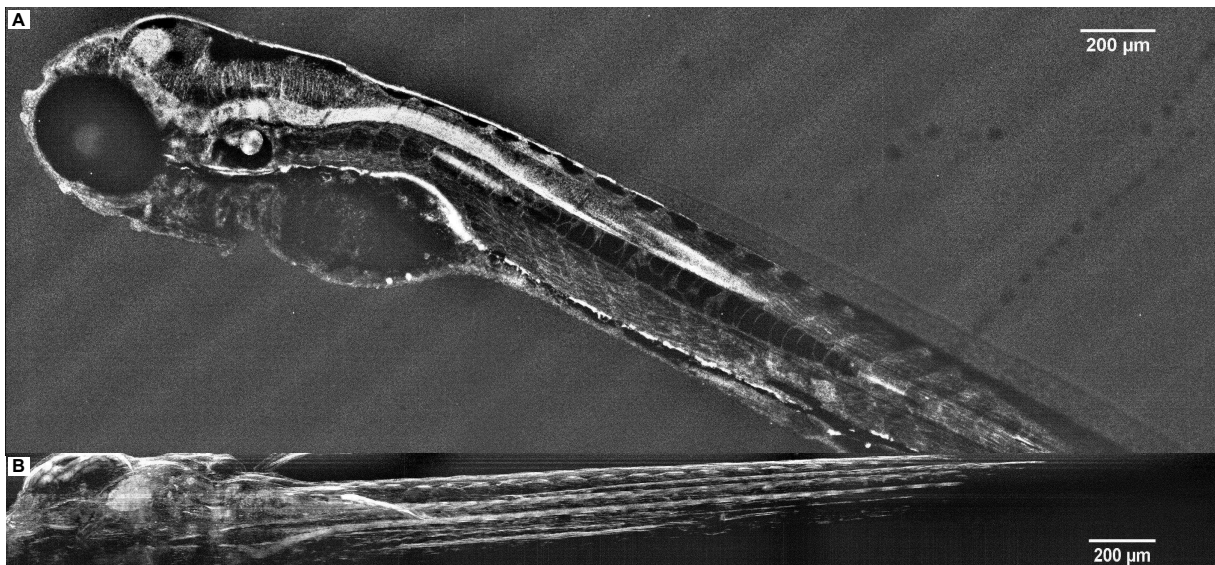


Figure 4.2 – 3 dimensional imaging of 5dpf Zebrafish larva with FFOCT [183]. (A) One single *en face* tomograms (xy plane) acquired in a side view of the larva. (B) 300 tomograms are acquired across the entire fish and combined to form a 3 dimensional image. Here the top view (xz plane) acquired with a maximum projection of the 3 dimensional data is displayed.

4.3 FFOCT performances

4.3.1 Resolution

As mentioned before that traditional OCT produces axially oriented images, a depth of field is needed as the coherence gate is scanned across the imaging depth. Thus, low NA objectives is typically used in order to obtain a relatively large imaging depth, which on the other hand limits the lateral resolution. While in FFOCT, *en face* tomograms is taken. High NA microscope objectives could be used to achieve high lateral resolution, up to around $1\mu m$. For FFOCT the lateral resolution is calculated in the same way as optical microscopy:

$$\Delta x = \Delta y = \frac{1.22\lambda}{2NA}. \quad (4.8)$$

As in traditional OCT, the determination of the axial resolution FFOCT relies mostly on the coherence length of the illumination source. With a Gaussian-shaped spectrum, the FFOCT axial resolution is calculated as equation 1.4:

$$\Delta z = \frac{2ln2}{\pi} \cdot \frac{\lambda^2}{\Delta\lambda}.$$

However, with a very high NA objective in FFOCT, the depth of focus of the objective might appear smaller compared to the temporal coherence length. In these cases, the axial resolution is actually still defined by sectioning ability offered by the depth of focus of the objective [183].

4.3.2 Field of view

The lateral field of view of FFOCT is depend on the camera pixel size, pixel numbers as well as the magnification of the system.

The imaging depth, or axial field of view, of FFOCT is mainly controlled by the extinction of the ballistic signal, which is a consequence of the absorption and scattering of light in the sample. This attenuation is also affected by the illumination wavelength. With illumination wavelength in the near-infrared window ($650nm - 1350nm$), absorption is minimized to ensure better penetration into the sample. Multiple scattering also affects the imaging depth. Although the multiple scattering light might not interfere with the reference beam, it is still detected on the camera thus limiting the detected number of useful photons. Aberration induced by the sample is another factor that limits the imaging depth, especially in large NA conditions. That's why defocus correction is necessary when doing depth imaging with FFOCT, even in relatively homogeneous samples. Currently, the typical imaging depth of FFOCT ranges from $100\mu m - 500\mu m$. Recently, the developments of dark-field FFOCT [184] and smart-OCT [8] have showed improved imaging depth with modified versions of FFOCT to better select the ballistic photons by filter multi-diffusion photons with either physical or numerical ways.

4.3.3 Sensitivity

The sensitivity of FFOCT is defined as the smallest detectable reflection coefficient, giving a SNR of 1. Regardless of the effects of multi-diffusion, aberrations and other reflections along the optical path, the SNR of FFOCT with four-phase modulation can be written as:

$$SNR = \frac{4N_0\sqrt{R_{ref} \cdot R_s}}{B} = \frac{4N_0\sqrt{R_{ref} \cdot R_s}}{\sqrt{N_{sat}}} \quad (4.9)$$

in which:

- $4N_0$ is the total number of incoming photons;
- R_{ref} is the reflectivity of the reference mirror;
- R_s is the reflectivity of the structures of the interest;
- N_{sat} is the full-well capacity of the camera;
- B is the shot noise, $B = \sqrt{N_{sat}}$.

Generally, the camera is almost filled with the photons coming from the reference arm ($N_0 \cdot R_{ref}$) and the incoherent counted photons coming from all the other structures that are out of the coherence volume and other stray reflections ($N_0 \cdot R_{inc}$). Thus: $N_{sat} = N_0(R_{ref} + R_{inc})$:

$$SNR = 4\sqrt{N_{sat}} \cdot \frac{\sqrt{R_{ref} \cdot R_s}}{R_{ref} + R_{inc}} \quad (4.10)$$

when $SNR = 1$, we would have $R_s = R_{min}$:

$$R_{min} = \frac{(R_{ref} + R_{inc})^2}{16N_{sat} \cdot R_{ref}} \quad (4.11)$$

In most of our systems, we chose to use silicon wafers as reference mirror, which provides a reflection coefficient of about 30% at the interface with air. In a typical sample, where the incoherent intensity corresponds to 10% of saturation of a CMOS Adimec camera (FWC of $1,6Me^-$), we obtain $R_{min} = 2.1 \times 10^{-8}$, which corresponds to a sensitivity of 77 dB.

4.3.4 Comparison of FFOCT with other OCT techniques

Table 4.1 summarize the main features of FFOCT compared with traditional scanning OCTs, scanning OCM and WFOCT.

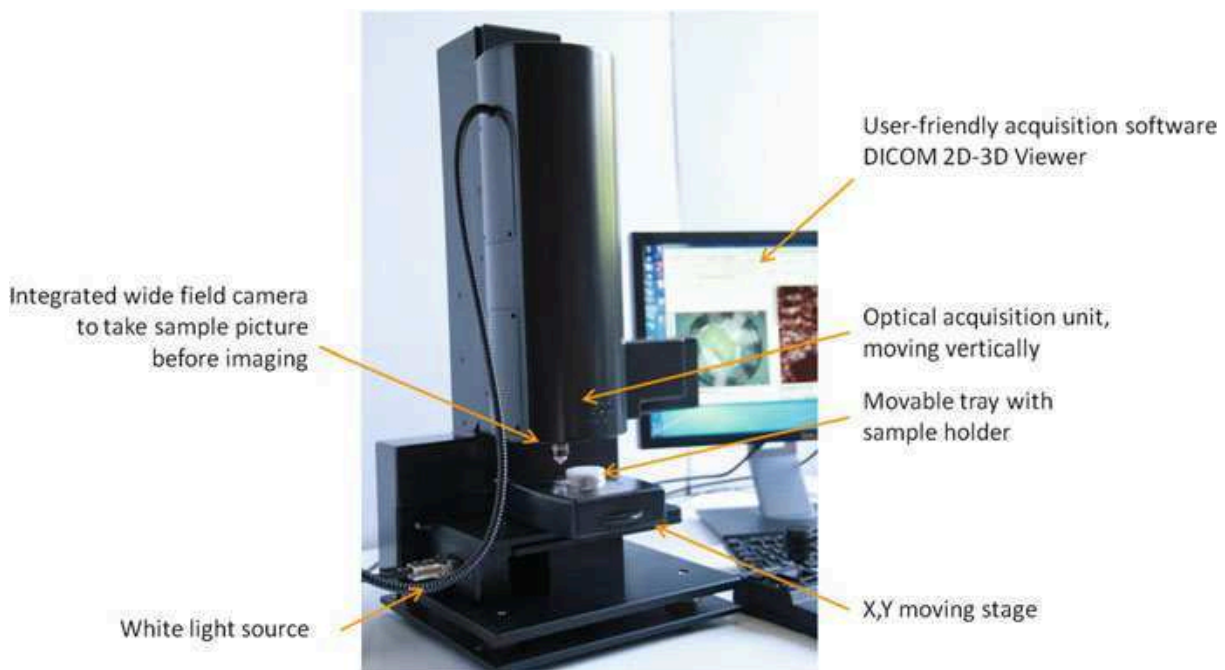
4.4 LightCT scanner

The LightCT scanner [186] is a commercialized FFOCT system developed by LLTech, an ESPCI Paris spin-off. The picture of the system is shown in figure 4.3. This system presents all the advantages of a good commercial system. It can provide consistent and reproducible images of a given sample, is relatively easy to use, and has long range 3D translations. However, its design is fixed, its software only optimized for a small number of imaging conditions, and is not very robust to external mechanical noise since the sample is hold by the motorized translations that are mechanically decoupled of the rest of the setup. The sample is sandwiched between a silica coverslip and the bottom of sample holder, which presents the advantage of flattening the sample. This is important in order to image nice 2D transverse views of the sample, and also

Table 4.1 – Comparison of main features of various OCT systems [185]

	Scanning OCTs (SDOCT/SSOCT)	Scanning OCM	WFOCT	FFOCT
Resolution Axial	3 – 10 μ m	3 – 8 μ m	3 – 8 μ m	0.5 – 8 μ m
Lateral	10 μ m	0.5 – 2 μ m	0.5 – 2 μ m	0.5 – 2 μ m
Speed (Pixels/s)	100G	1-10G >100G with swept source	10-50G 1 processed image	10-50G 1 processed image
Sources	SLD/Lasers	SLD/Lasers	SLD/Lasers	Thermal sources LEDs
Typical power	10 – 100mW	10 – 100mW	1mW	0.5 – 2mW
Sensitivity	100/110dB	100/110dB		80 – 90dB
Aberration correction	With AO	With AO	With AO	No loss of resolution Signal reduction only
Sensitivity to movements	Correction possible	Correction possible	Correction unlikely	Correction unlikely

reduce optical aberrations. LightCt scanner uses 10X, 0.3NA objectives and a thermal source that gives an isotropic 3D resolution of 1 μ m. Coupled to the long range motorized translations, it can acquire large field of views ($0.8 \times 0.8\text{mm}^2$ for single shot, and can be further extended to the order of 1" in diameter by translating the sample and combining different frames).

**Figure 4.3 – Picture of the LLTech lightCT scanner [186].**

4.5 FFOCT applications

Due to the nature of high spatial resolution and taking images with *en face* planes, FFOCT has been applied to medical diagnosis to target complementing histology of *ex vivo* tissues [187–192], functional imaging related with cellular metabolism [193], blood flow [194] or tissue elastography [195], study of embryology and developmental biology [196,197], material characterization and non-destructive testing [198], and also biometrics like fingerprints imaging [199].

4.5.1 Histological evaluation of *ex vivo* tissues

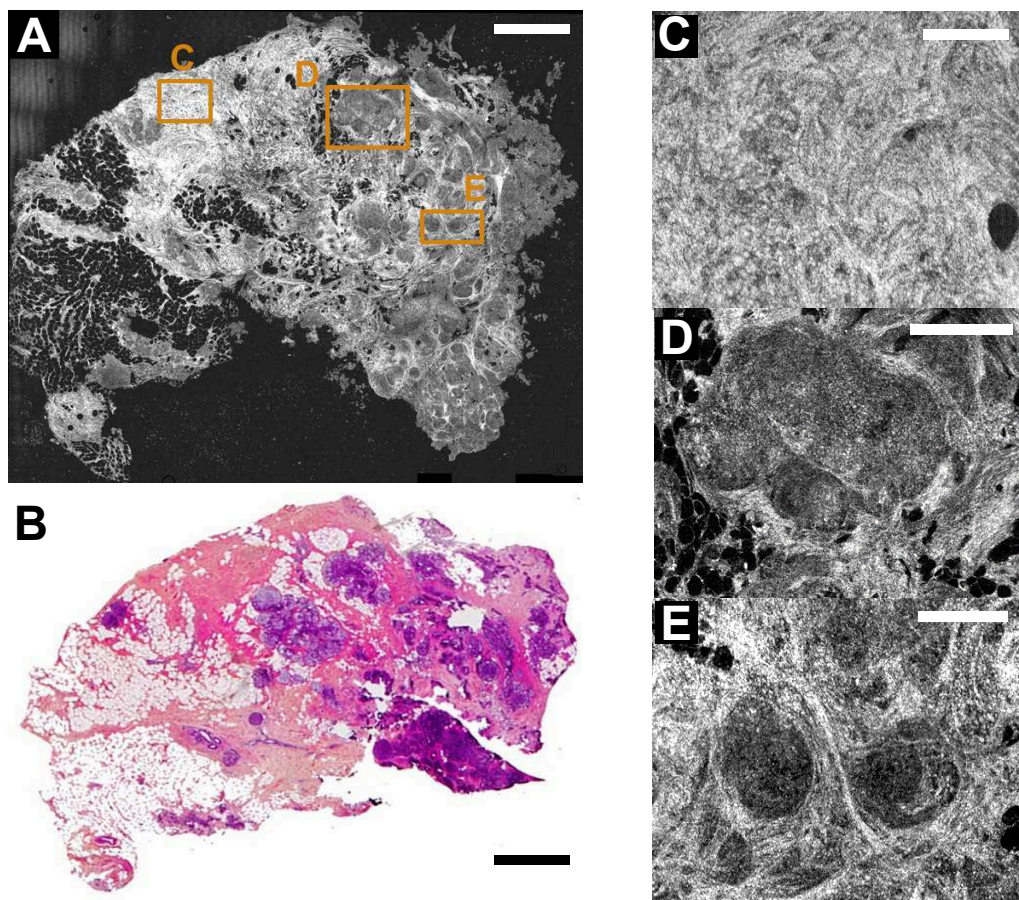


Figure 4.4 – Comparison between FFOCT and Histology [200]. (A,B) Large field image of a breast sample affected by DCIS acquired with FFOCT (A) and histology (H & E staining; (B–E) Zoom in from boxes represented in (A), showing a normal fibrous tissue (C), enlarged ducts(D), and the collagen organization around the carcinomatous cells in a tumorous region(E).

With the advantage of high lateral resolution with relative large imaging field of view, the applications of FFOCT are demonstrated mostly to medical diagnosis with label-free *ex vivo* tissues [187–192]. Compared with biopsy and histology, which are invasive and time-consuming, FFOCT offers the possibility to provide tomographic images of spatial resolution and contrast similar to that of histology images, without the need for tissue processing and preparation. A large number of images of different pathologies, mostly cancers [191, 192], are available on the LLTech image atlas website [201]. FFOCT has demonstrated high levels of sensitivity and

specificity for most of the pathologies, often over 90%. It is reported to reach 100% correct identification of tumours in *ex vivo* kidneys [190], offering similar results as histology. Figure 4.4 shows a comparison between FF-OCT and a regular Hematoxylin and Eosin (H & E) stain histology of a breast sample that was affected by a ductal carcinoma in situ (DCIS). FF-OCT notably reveals normal adipocytes, normal and abnormal collagen fibers, and enlarged ducts. These indicators are characteristics of DCIS, that could be identified with 90% sensitivity and 75% specificity with FFOCT [191].

FFOCT is believed to have great potential in many clinical or surgical contexts, such as being an adjunct tool to histology in intraoperative consultation, obtaining diagnostically relevant tissue during biopsy procedure, or selecting tissue before cryopreservation in biobanking. For the cases when FFOCT does not have enough specificity compared with the gold standard histology, the diagnosis sensitivity and specificity could further be improved by combining with other imaging modalities, such as fluorescence [178,202], photothermal [203], elastography [195], polarization [204] or multispectral and hyperspectral imaging [205,206] to offer complementary information.

4.5.2 Dynamic FFOCT imaging

Motion is a key factor in living systems, one can use FFOCT to assess the evolution of structures with time. Blood flows can be imaged and analysed, and individual erythrocytes can be tracked if the frame rate of the camera is good enough compared to the flow of red blood cells [194]. Dynamic FFOCT aims to highlight intracellular movements and vibrations, that take place inside cells and contributing to its own function [193]. For that matter we record a short movie of en face interferometric images. By calculating the standard deviation of the interferometric signal over time, it gives the amplitude of the signal fluctuations, a substantially different contrast in comparison with the regular FF-OCT signal. This dynamic FFOCT signal, indicating the fluctuations of the backscattered intensity, is linked with the local metabolism inside the sample. To extract more information from intracellular dynamics, the timescales of these variations could also be analysed by calculating the Fourier transform of the time signal. Signals of different frequency bands could be integrated to show dynamic signal originating from different timescales [200].

Figure 4.5 shows the images of static and dynamic FFOCT of the retinal ganglion cell layer in mouse. Thanks to its high spatial resolution, in the ganglion cell layer, FFOCT is able to separate the contribution of the strongly scattering ganglion cells axons to the one of capillaries walls and to the least scattering structures of ganglion cells. Figure 4.5(left) presents a typical FFOCT image of a mouse retinal ganglion cell layer. Figure 4.5(right) displays the amplitude of the temporal fluctuations. The signal from stationary axons and blood vessels is hidden while adding an intracellular contrast, which notably allows the detection of some cell nuclei and enhances the signal from the red blood cells trapped inside the capillaries, thanks to their highly fluctuating membranes. By considering the relative frequencies of the temporal fluctuations. Structures with different signal fluctuation frequencies are able to be separated. Figure 4.5(center) shows a RGB image with the slowly varying structures ($< 0.5Hz$) displayed in red, the intermediate structures in green, and the fastest structures ($> 10Hz$) in blue. This display enables the identification of two cell populations: round cells with almost no

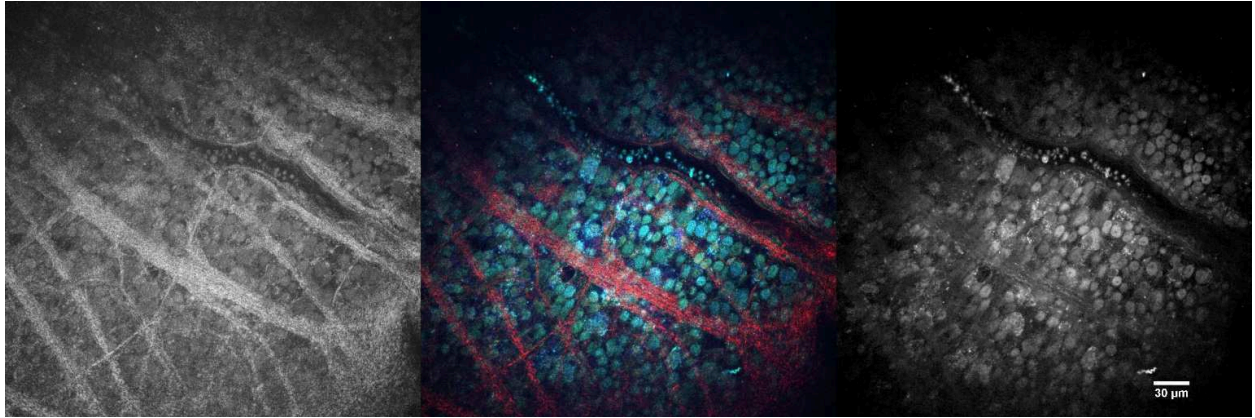


Figure 4.5 – Static and dynamic FFOCT of the retinal ganglion cell layer in mouse [185]. These panels display 3 different views of the same plane inside the ganglion cell layer of a mouse retinal explant, about $30\mu m$ from the surface of the retina. The left hand panel presents the static contrast of this plane offered by FFOCT. By taking advantage of the dynamics inside the living cells of this retina, the Fourier transform of the temporal signal fluctuations is computed. The center panel shows an RGB combination of different frequency bands: The red color represents the low temporal frequencies ($< 0.5Hz$), the green the intermediate frequencies (between 0.5 and $10Hz$), and the blue emphasizes the fastest pixels ($> 10Hz$). The right hand panel is the same image as the blue component of the image in the center panel. The scale bar is $30\mu m$.

intracellular inhomogeneity and some cells that have a faster cytoplasm with a slower dark area which could correspond to the nucleus. These two cell populations could be respectively the displaced amacrine cells and the ganglion cells, which would offer a way to discriminate these cells without any label in an active retina.

4.5.3 Inner fingerprint imaging



Figure 4.6 – Comparison of internal fingerprints taken by FFOCT with external fingerprints taken by FTIR [185]. (left) In vivo FFOCT image of internal fingerprint taken a few hundred micrometers below the skin surface and (right) total reflection image of the same external fingerprint (inversed contrast).

Most optical fingerprint sensors today are based on frustrated total internal reflection (FTIR),

which produces images by reflecting light from areas where the skin does not come in contact with a glass plate, a technique that captures details from only the very top layer of skin. Since imitation fingerprints could easily trick up to 80% of these standard fingerprint sensors and it would fail to produce adequate images for identification when a finger has creases, is dirty, scarred or too wet/dry, considerable interests goes to image the inner fingerprint, which serves as a template for external fingerprint regrows and is believed to be less affected by the surface damage. With its 3 dimensional imaging ability, OCT has been applied for fingerprint imaging and *en face* OCT images of internal fingerprints [207] could be reconstructed. On the contrary, FFOCT is able to capture these *en face* images without the acquisition of 3 dimensional data volume [199]. Figure 4.6 shows the comparison of internal fingerprints images taken fast FFOCT fingerprint imaging with the external fingerprints taken by FTIR.

 FFOCT resolution insensitive to aberrations

Table of contents

5.1	Aberration fuzziness and PSF	60
5.2	The unexpected PSF determination using nanoparticles in FFOCT	61
5.3	Optical coherence	61
5.3.1	Temporal coherence	63
5.3.2	Spatial coherence	63
	Van Cittert-Zernike theorem	64
5.4	Theoretical system PSF analysis in various OCTs	65
5.4.1	Scanning OCT with spatially coherent illumination	66
5.4.2	WFOCT with spatially coherent illumination	66
5.4.3	FFOCT with spatially incoherent illumination	68
	Non-aberrated condition	68
	Aberrated condition	69
5.5	Experimental confirmation with extended object	71
5.5.1	USAF imaging with defocus	71
5.5.2	UASF imaging with random aberration	72

5.1 Aberration fuzziness and PSF

In the development of a generalized model of an imaging system, it is specifically assumed that the presence of a point-source object yields at the exit pupil a perfect spherical wave, converging toward the ideal geometrical image point. Such a system was called diffraction-limited and the PSF is a diffraction-limited spot. But as discussed in section 2.1 and section 3.1.2, aberrations often exist in imaging systems due to the optical system design (e.g. a photographic lens at full aperture) or the wavefront distortions induced by multi-scale aberrating structures along the light path from the object to its image. This is the case in astronomy where images of stars are blurred by the atmospheric turbulence or in human vision because of the eye aberrations are more and more pronounced when the pupil size is increase (e.g. night vision). In both case successful aberration corrections have been obtained by using AO.

We are used to observe images that are affected by aberrations (figure 5.1). They are various equivalent ways to quantify the fuzziness either in the real space using the PSF that reflects the spread of the image of a spatial unit source of light in the object plane or its Fourier transform (transfer function) that express the contrast of periodic object images [208]. In the hypothesis of a linear relationship between the object considered as a source and its image, there is a simple relation between the object, the image and the PSF: the image is the convolution of the object (within the magnification of the optical system) with the imaging system PSF. Note that the spatial coherence of the object illumination must be considered: complex amplitude must be used in the case of a coherent illumination, whereas intensity is used for an incoherent illumination [208, 209]. Here coherent as well as incoherent illuminations are used as we are dealing with imaging interferometers we will have to consider amplitudes.

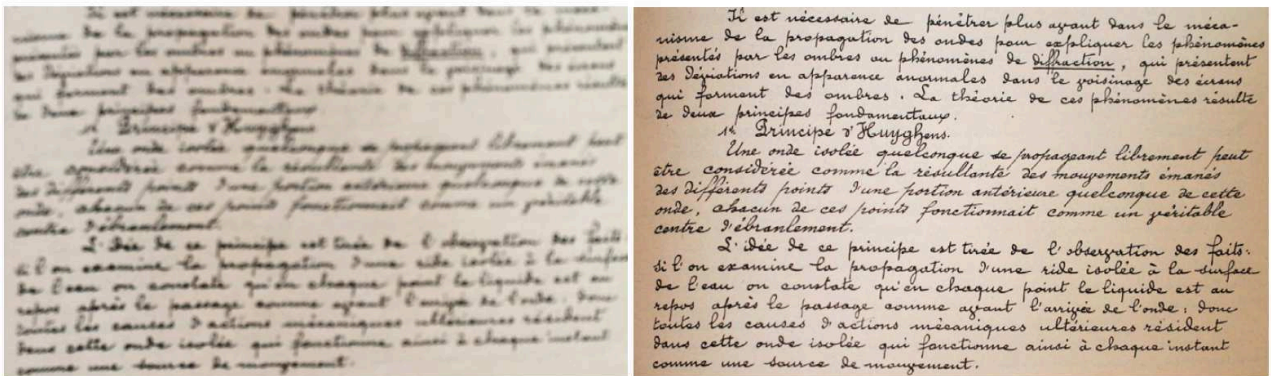


Figure 5.1 – Aberrations reduce the sharpness of the images (Cornu, Polytechnique, 1897).

5.2 The unexpected PSF determination using nanoparticles in FFOCT

During the work of quantifying the effects of geometrical aberrations on FFOCT image, we found that the FFOCT PSF width is almost insensitive to the aberrations induced to the imaging system. By using a commercial FFOCT system LLtech LightCT scanner (section 4.4), experiments has been done with gold nanoparticles in order to follow how the PSF would be affected by various level of defocus aberration. The PSF of such system has a width of about $1.5\mu m$, meaning that with gold nanoparticles having a diameter much smaller than this value, we can record a reliable PSF. The $40nm$ radius gold particles solution was diluted and dried on a coverslip so that single particles could be imaged. By moving the sample stage by $10\mu m$, $20\mu m$ and $30\mu m$ a variable noticeable defocus was induced to the targeted particle if we account for the 0.3 numerical aperture of the microscope (corresponding to RMS of $0.13\mu m$, $0.26\mu m$ and $0.39\mu m$). The initial system resolution of $1.5\mu m$ corresponds to 2.5 pixels on the camera. By adding $10\mu m$, $20\mu m$ and $30\mu m$ defocus, the sample PSF would be broadened by 2.3 times, 4.6 times and 6.9 times. To match the coherence plane with the defocused coverslip in the sample arm for FFOCT imaging, the FFOCT reference arm length is also shifted by $10\mu m$, $20\mu m$ and $30\mu m$ correspondingly. FFOCT images (figure 5.2(a-d)) and the corresponding signal profiles (figure 5.2(e-h)) of the same nanoparticle were displayed in figure 5.2. With more defocus added the signal level of the gold nanoparticles is reduced, but the normalized signal profiles graph (figure 5.2(i)) shows clearly that the size of the particle that corresponds to the system PSF width keeps the same for all the situations.

One can argue that the PSF is not strictly the same: indeed one can first observe more pronounced wings. As we will see later this is due to the fact that we shift from the product of 2 Bessel functions (Reference PSF times the Object PSF) of the same width (Object PSF without aberrations) to a single Bessel one. The symmetry breaking could be due to a small misalignment of the microscope objective. Finally we have to underline that if the width appears unaffected by the strong defocus, the magnitude of the PSF is reduced by more than 20 times, which matches with the theoretical amplitude reduction that would be induced by $30\mu m$ defocus with $0.3NA$ objective in FFOCT. This signal reduction will be used as the metric of our aberration correction, which will be discussed in chapter 6.

5.3 Optical coherence

Before going to the theoretical analysis to explain the above unexpected phenomenon in FFOCT, it is important to understand an important concept, the optical coherence. Note that the one of the most important difference between FFOCT and many other traditional OCT techniques is the spatial coherence of the illumination.

In physics, two wave sources are perfectly coherent if they have a constant phase difference and the same frequency to enable stationary interference, which is an ideal condition as it never quite occurs in reality. In optical interferometry, optical coherence refers to the ability of a light waves to produce interference patterns. If two light waves are brought together and they produce no interference pattern (no regions of increased and decreased brightness), they

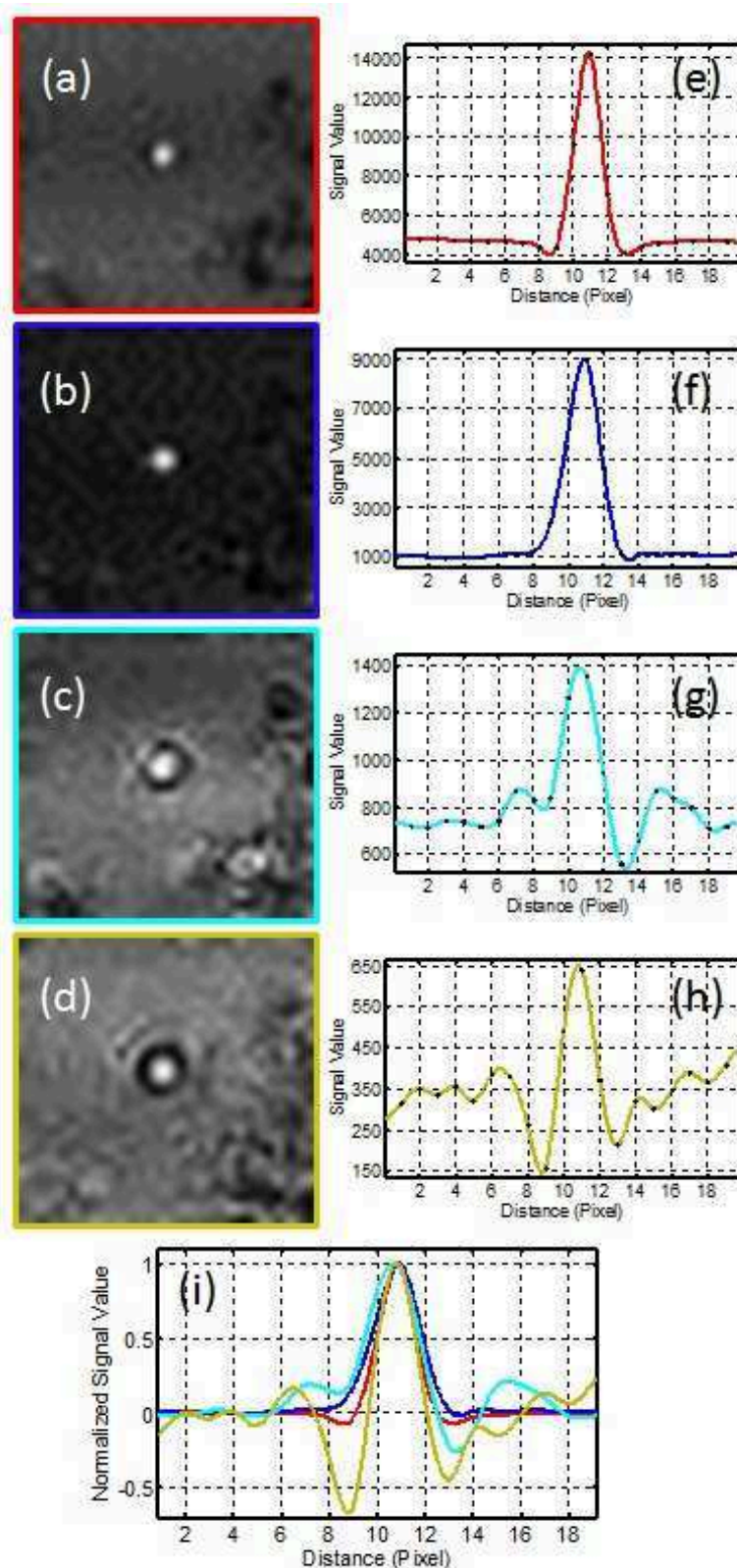


Figure 5.2 – FFOCT experiment results of gold nanoparticles by adding different levels of defocus using LightCT scanner [210]. FFOCT images (a-d) and the corresponding intensity profile (e-h) of a targeted nanoparticle are shown for well-focused (a,e) and defocused for 10 μm (b,f), 20 μm (c,g) and 30 μm (d,h) situations. Normalized PSF profiles are shown in (i) indicating no obvious broadening are observed after inducing different level of defocus.

are said to be incoherent; if they produce a "perfect" (clear with the best contrast) interference pattern, they are said to be fully coherent; If the two light waves produce a "less-than-perfect" interference pattern, they are said to be partially coherent or low coherent.

5.3.1 Temporal coherence

As what have been described in section 1.3 of low coherence interferometry for OCT, the low coherence refers to the temporal coherence of the illumination, which describes the correlation between waves observed at different moments in time. This can be observed in the Michelson interferometer, in which light wave interferes with time-delayed version of itself, as shown in figure 5.3. when one of the mirrors is moved away gradually, the time for the beam to travel increases and the fringes become dull and finally are lost, showing temporal coherence. The light which travels along the path to mirror M1 travels a distance $2d$ further than the light which travels along the path to mirror M2. When $d = 0$, we would see clear interference fringes. When d increases, however, the interference fringes would become less distinct. While for very large d , over the coherence length l_c , the interference pattern would vanish completely, leaving only a diffuse spot of light.

Note that, the axial sectioning abilities in both FFOCT and traditional OCT techniques all come from the low temporal coherence of the illumination, defined by half of the temporal coherence length of the illumination as equation 1.4

$$\Delta z = \frac{l_c}{2} = \frac{2ln2}{\pi} \cdot \frac{\lambda^2}{\Delta\lambda}.$$

5.3.2 Spatial coherence

Beside of the temporal coherence, the correlation between waves at different points in space is defined as the spatial coherence. This phenomenon can be observed in Young's interferometer, in which a light interferes with a spatially-shifted version of itself ,as shown in figure 5.4. A light source is used to simultaneously illuminate a pair of small pinholes, separated by a distance d , in an opaque screen. The light emanating from the pinholes interferes on a second screen some distance away. In a manner similar to that described for temporal coherence, the separation d of the two pinholes could be increased. For small values of d , one sees a distinct pattern of interference fringes on the screen. As d is increased, however, the fringes become less distinct (except for the pattern on the optical axis). And for sufficiently large d , over the spatial coherence length $l_s = 2\rho$, no fringes are visible and only a diffuse spot of light remains on the screen. This critical value ρ is the radius of the spatial coherence area (CA), within which the pinholes must lie to observe interference.

In traditional scanning OCT systems, SLD/lasers is used as the source to generate point scanning across the sample. These SLD/lasers are spatially coherent sources. Parallel OCT systems can also use spatially coherent illumination as in WFOCT. While in FFOCT system, spatially incoherent source is used, to minimize crosstalk that could be generated due to scattering. The use of this spatially incoherent illumination in FFOCT is also the main reason why we observe this unexpected phenomenon shown in the former section.

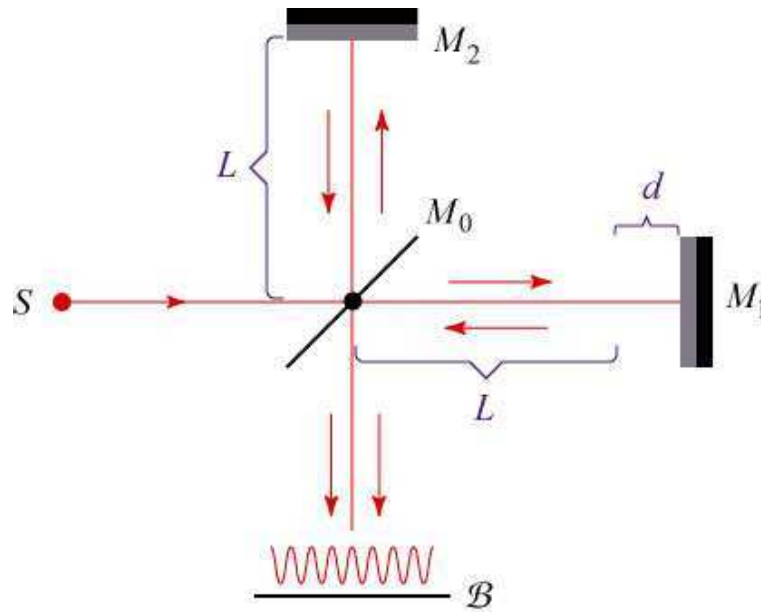


Figure 5.3 – Schematic of a Michelson interferometer [211]. Light from a source S (which could be anything: sunlight, laser light, starlight) is directed upon a half-silvered mirror M_0 , which sends 50% of the light towards mirror M_1 and 50% of the light towards mirror M_2 . The light is reflected from each of these mirrors, returns to the beamsplitter M_0 , and equal portions of the light reflected from M_1 and M_2 is combined and projected on the screen B . The interferometer is tunable, in that we can adjust the distance of the mirror M_1 from the beamsplitter.

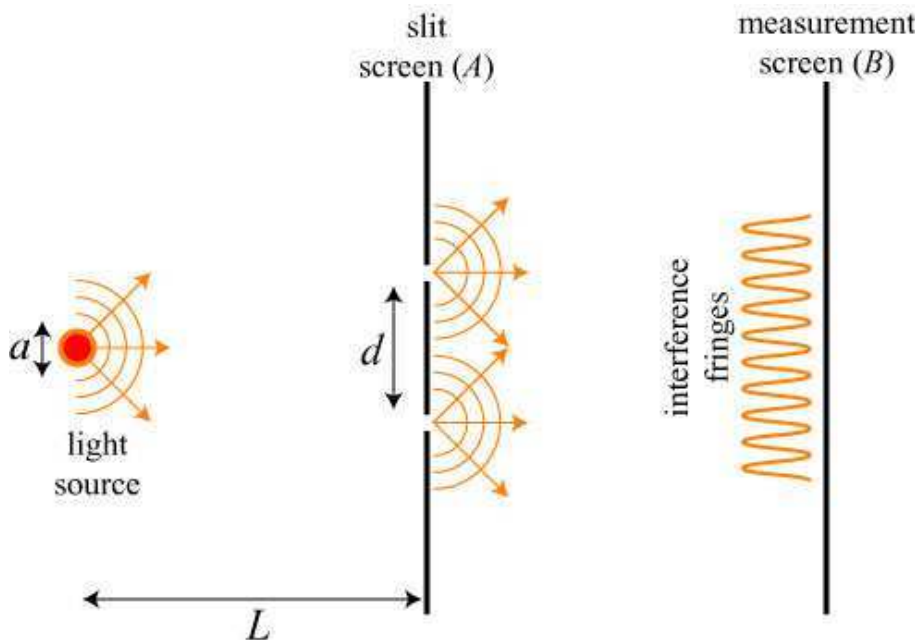


Figure 5.4 – Young's two-pinhole experiment [212]. Light emanating from a thermal source of transverse size a is incident upon an opaque screen a distance L away. The screen is perforated by two holes separated by a distance d .

Van Cittert-Zernike theorem

To decide the CA in imaging systems with spatially incoherent illumination, one should know about the famous van Cittert-Zernike theorem that was published by Dutch physicists P.H.

van Cittert in 1934 [213] and followed by a simpler derivation by F. Zernike in 1938 [214]. The theorem is a rigorous theoretical calculation of the increase of spatial coherence on wave propagation, which implies that the spatially incoherent wavefront would appear mostly coherent after travelling for large distances. Intuitively, one can consider the wavefronts created by two incoherent sources. The coherence of the wavefront would be dominated by the near by source if we measure the wavefront right in front of one of the sources. However, the measurement would not be dominated only by a single source if we make the measurement far away from the sources; both sources will contribute almost equally to the wavefront, meaning the wavefront would be spatially coherent as it propagate to large distances. This is especially relevant for astronomy, where all the stars are spatially incoherent sources, as the light waves become more coherent via the van Cittert-Zernike theorem, the single point sources within the star become more indistinguishable making the luminous star appears more point-like when imaging far away.

The Van Cittert-Zernike theorem states that there is a Fourier transform relationship between the mutual intensity function and spatial intensity distribution of an extended incoherent source. For detailed description of van Cittert-Zernike theorem, one can refer to chapter 10 in the book by Born and Wolf [208]. In the case shown in figure 5.4, the coherence angle can be calculated as

$$\alpha \approx \sin\alpha \approx \frac{\lambda}{a} \text{ (for small } \alpha \text{)}, \quad (5.1)$$

corresponding to the CA with a radius of ρ at the pinhole plane

$$\rho = 1.22 \cdot \frac{\lambda \cdot L}{a} \quad (5.2)$$

meaning that significant interference fringes would appear if two pinholes lie within this transverse area. The further the pinholes are from the source, the greater the radius of CA is.

5.4 Theoretical system PSF analysis in various OCTs

As mentioned before aberrations are known to blur optical images by perturbing the wavefronts; more precisely the distorted optical images are obtained by amplitude or intensity convolution of the diffraction-limited images with the aberrated PSF. Depending on the nature of the illumination, spatially coherent or incoherent, amplitude or intensity has to be considered. Here, instead of considering the PSF of a classical imaging system such as a microscope, we will pay attention to the system PSF of interferometric imaging systems for which an undistorted wavefront from a reference beam interferes with the distorted wavefront of the object beam. To express the unique behavior of FFOCT that uses spatially incoherent sources we will successively consider the cases of scanning OCT with spatially coherent illumination, WFOCT with spatially coherent illumination and FFOCT with spatially incoherent illumination. Usually when scanning the field of view for a flying spot image, each acquisition (voxel or line) is an independent event and this is equivalent to an incoherent illumination with various CAs. Surprisingly scanning OCT and incoherent illumination FFOCT are not equivalent in presence of aberrations: Indeed, in spatially incoherent full-field interferometer, the system PSF width

is almost insensitive to aberrations and only the signal amplitude is reduced by the wavefront distortions.

In order to stick to the PSF definition, we will consider a point scatterer as our object and will analyze the response of the imaging system to such object. Suppose the sample arm PSF of the interferometer is h_s , the reference arm PSF of the interferometer is h_r and the single point scatterer in the detection plane is at position $(x, y) = (a, b)$. For simplification, we ignore all the constant factors in the following expressions. So in all the three cases, the sample field at the detection plane would be

$$g_s = h_s(x - a, y - b). \quad (5.3)$$

5.4.1 Scanning OCT with spatially coherent illumination

In the case of traditional scanning OCT, the reference field of each scanning position at the detection plane would be $h_r(x, y)$. Since coherent illumination is used, interference happens at each scanning position that can be indicated as a multiplication of the sample field and reference field. To form the full image of the point scatterer which represent the system PSF, the interference field of each scanning position should be summed up. Thus the final field is a integral of the interference field at each position across the scanning filed that can be represented in a convolution of the two fields:

$$\langle g_s \cdot g_r \rangle_{\text{scanningOCT}} = \int \int h_s(x' - a, y' - b) \cdot h_r(x - x', y - y') dx' dy' = h_s(x - a, y - b) * h_r(x, y), \quad (5.4)$$

in which x' and y' are dummy variables limiting by the imaging field. Thus, the system PSF of scanning OCT system is actually a convolution of the sample arm PSF and the reference arm PSF as shown in figure 5.5(a-c). When aberrations exist, the convolution of the aberrated sample arm PSF with the diffraction-limited reference arm PSF results in an aberrated system PSF for the scanning OCT systems (figure 5.5(d-f)).

5.4.2 WFOCT with spatially coherent illumination

In the case of WFOCT, as coherent sources are used, the optical beams are typically broadened by lenses to form parallel illuminations on both arms of the interferometer(see section 1.5.2). Thus plane waves impinge on both the object and the reference mirror. In the sample arm, the point scatterer will send a spherical wave back that will be focus on the camera plane that can be described by expression 5.3. For the reference arm, consider it as homogeneous illumination, a plane wave will be reflected back by the reference mirror and form a uniform field at the camera plane. Thus the interference happen between the two arms would be

$$\langle g_s \cdot g_r \rangle_{\text{WFOCT}} = h_s(x - a, y - b) \quad (5.5)$$

as constant value is ignored. So the system PSF is actually defined by the sample PSF. It is illustrated in figure 5.5(g-i). When aberrations distort the backscattered wavefront of the sample arm, the aberrated sample arm PSF and the uniform reference field interfere, resulting in an aberrated system PSF for the wide-filed OCT systems (figure 5.5(j-l)).

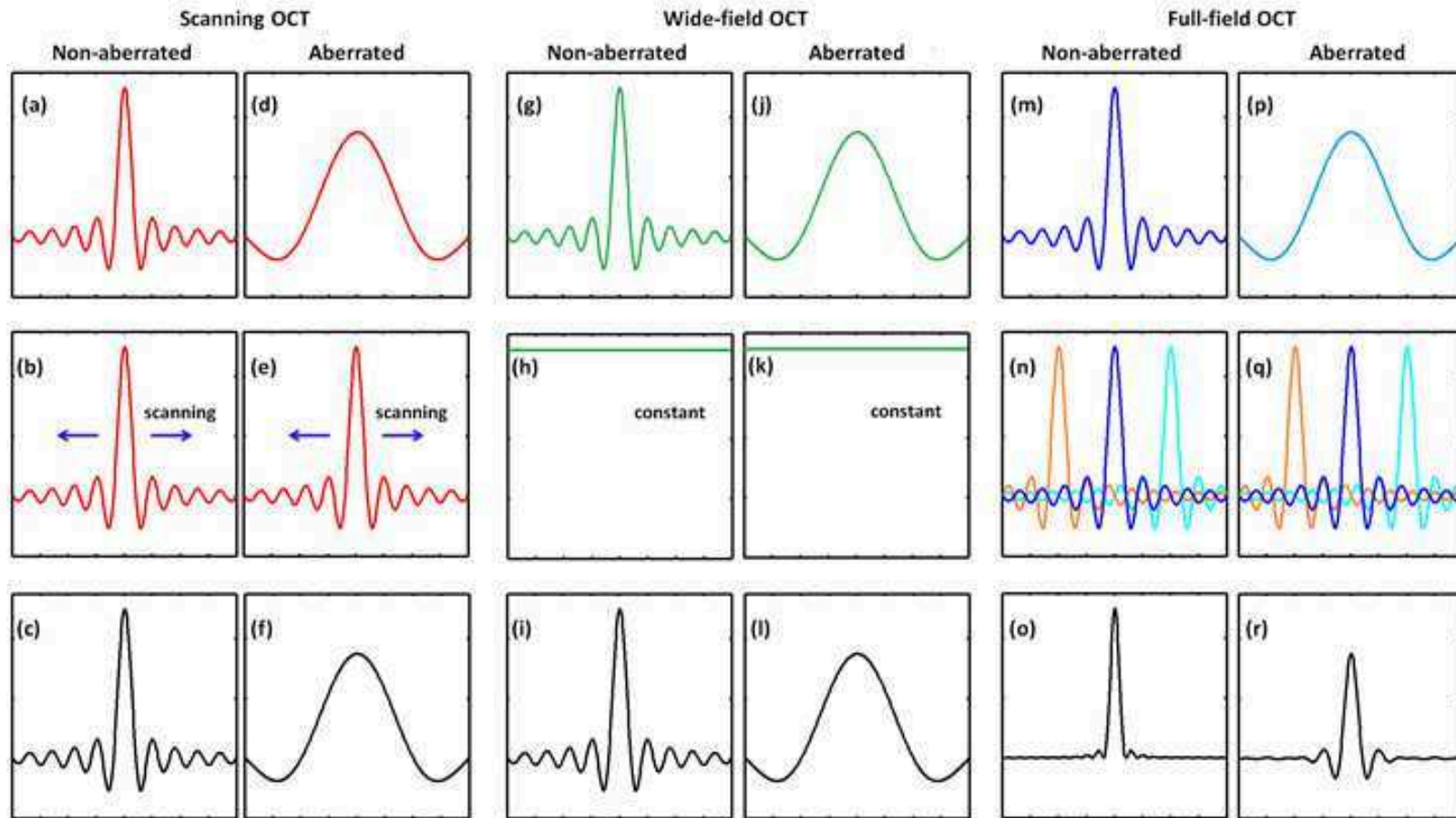


Figure 5.5 – Illustration of single point scatterer (PSF) interferences in both non-aberrated and aberrated sample arm PSF situations for scanning OCT and wide-field OCT with spatially coherent illumination and FFOCT with spatially incoherent illumination [210]. (a), (g), and (m) Non-aberrated sample arm PSF. (d), (j), and (p) Aberrated sample arm PSF. (b) and (e) Scanning reference arm PSF for scanning OCT. (h) and (k) Constant reference field for WFOCT. (n) and (q) Reference arm PSFs for FFOCT. (c), (f), (i), (l), (o), and (r) The corresponding interference signal (system PSF). Different colors in (n) and (q) indicate the spatial incoherence from each other.

5.4.3 FFOCT with spatially incoherent illumination

When we deal with the case of full-field OCT with spatially incoherent illumination, we have to go back to the basic definition of the spatial coherence of the beams that impinge the reference arm as well as the sample arm of the interferometer. As shown in figure 5.6, let's consider a circular uniform incoherent source located in the image focal plane of a microscope objective with a focal length of f_0 , which could be obtained with a standard Koehler illumination with LED or halogen lamp illuminations. The source illuminates the field of view of the microscope objective.

One first step is to determine the spatial coherence length in the field of view. As discussed before, based on the Van Cittert-Zernike theorem, if the pupil diameter is D , according to equation 5.1, the coherence angle would be

$$\alpha \approx \frac{\lambda}{D}. \quad (5.6)$$

According to equation 5.2, the radius of the CA at the level of focal plane would be

$$\rho = 1.22 \cdot \frac{\lambda \cdot f_0}{D} \approx 1.22 \cdot \frac{\lambda}{2 \cdot NA}. \quad (5.7)$$

We can say that, in absence of aberrations, the focal plane is “paved” by small CAs of radius ρ . This radius is also the radius of the diffraction spot that limits the resolution of the microscope objective in absence of aberrations. When going from one diffraction spot to the next adjacent diffraction spots the incoherent plane waves impinging the objective are separated by $\pm\lambda$ on the edges of the pupil.

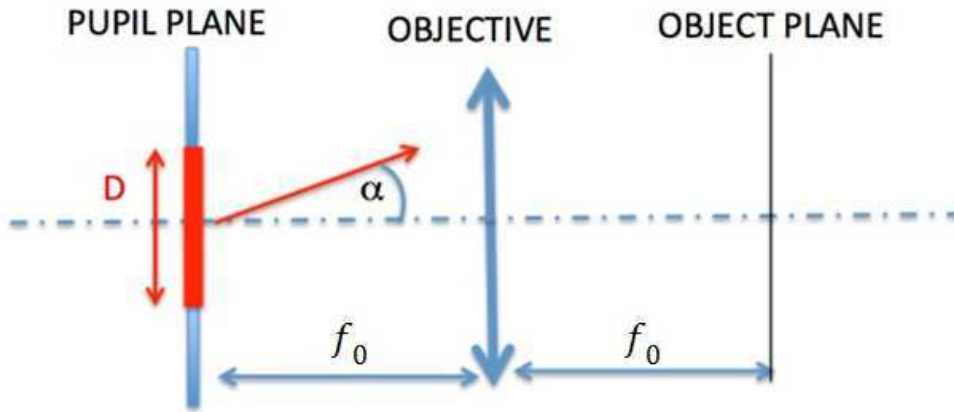


Figure 5.6 – Illustration of the Van Cittert-Zernike theorem defining the coherence angle α in the case of an objective with a focal length f_0 and pupil diameter D [215].

Non-aberrated condition

In absence of aberrations for an interferometry like full-field OCT, the single point scatterer at the object plane of the sample arm lies in a single CA (figure 5.7(a)) and the backscattered signal will only interfere with signal reflected from the corresponding CA in the reference arm

(figure 5.7(c)). Note that the size of the CAs is the same as the diffraction spot, the signal from one CA at the camera plane could be expressed as the reference PSF. Thus the interference would be

$$\langle g_s \cdot g_r \rangle_{FFOCT} = h_s(x - a, y - b) \cdot h_r(x - a, y - b) \quad (5.8)$$

The system PSF is actually the dot product of the sample PSF and the reference PSF as shown in figure 5.5(m-o). The overall signal reflected from the reference mirror at the camera is still homogenous but we displayed it by combining multiple reference PSFs reflected from different CAs that have different spatial modes.

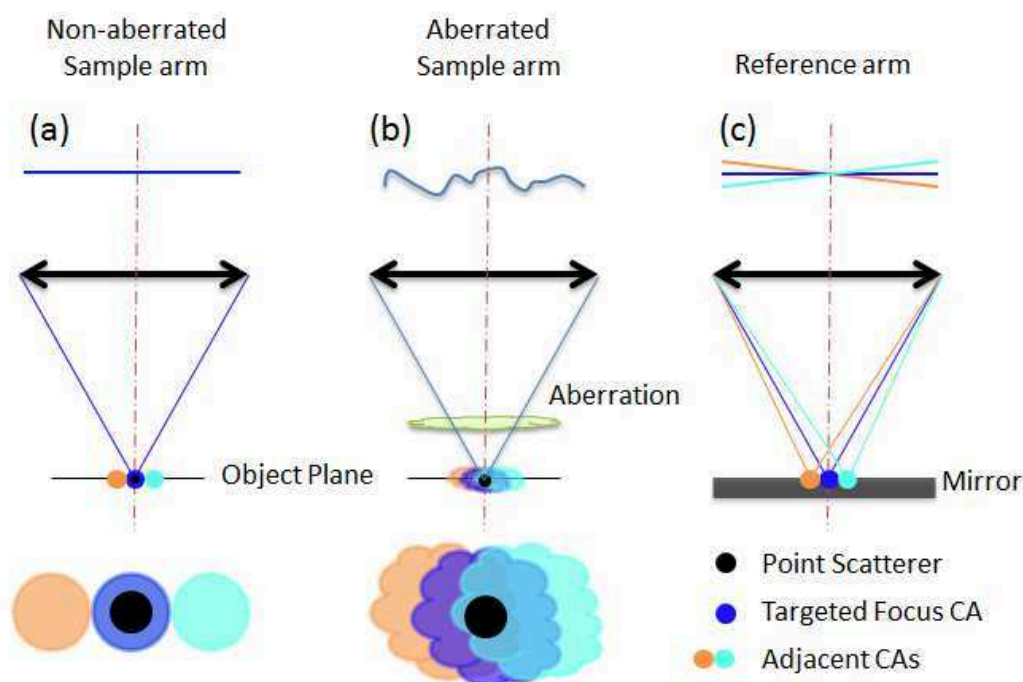


Figure 5.7 – Illustration of the sample and reference wavefronts in spatially incoherent interferometer with a single point scatterer in cases of non-aberrated and aberrated sample arm [210]. Different colors in CAs and wavefronts indicate different spatial modes.

Aberrated condition

When aberrations exist in the sample arm, the various CAs in the object plane will have larger sizes and will overlap each other (figure 5.7(b)). This results in the backscattered signal of the single point scatterer in the sample arm containing not only the spatial mode of the targeted focus CA but also the modes from the overlapped adjacent CAs. Thus with aberrations that create a broadened sample PSF, interference will happen not only with the reference beam corresponding to the targeted CA, but also with the beams corresponding to the adjacent CAs. What we want to demonstrate and to illustrate by an experiment is that the interference signal with the targeted focus CA gives a much stronger signal than the one with the adjacent CAs resulting in an “interference” PSF that is much thinner than the one of the classical broadened sample PSF. At the level of the image plane, the interference between the sample aberrated beam and the non aberrated reference beam is only constructive in a zone limited by the spatial

coherence of the reference beam. In order to be more quantitative we are going to compare this by the Strehl ratio approach(section 2.3).

The “best focus” signal intensity damping compared to the diffraction limited PSF is given (for small aberrations) by the Strehl ratio that is proportionnal to the peak aberrated image intensity. As equation 2.7

$$S \approx e^{-\sigma^2}$$

where σ is the root mean square deviation over the aperture of the wavefront phase defined by equation 2.4

$$\sigma^2 = (std(\phi))^2.$$

In our case, suppose ϕ is the phase of the interference wavefront between the sample signal and the reference signal corresponding to the targeted focus CA, then the phase of the interference wavefront with the reference signals corresponding to an adjacent CAs is $\phi + \phi_1$, where ϕ_1 is a phase that varies linearly from one edge of the pupil to the other in the range of $\pm 2\pi$. A comparison between the signal ratio of the interference signal with the targeted CA and the one with an adjacent CAs

$$S_{targeted} = e^{-((std(\phi))^2)} \gg S_{adjacent} = e^{-((std(\phi+\phi_1))^2)} \quad (5.9)$$

shows that the influence of off axis CAs is negligible.

Let’s consider various aberrations leading to a significant Strehl ratio of 0.3, numerical calculations results are shown in figure 5.8. For defocus, the intensity ratio of the interference with adjacent CAs is damped for about 740 times compared with the interference with the targeted focus CA, resulting in a signal damping or an amplitude damping of 27.1 times. The amplitude damping ratio is calculated by

$$Amplitude\ damping = \sqrt{\frac{S_{targeted}}{S_{adjacent}}} \quad (5.10)$$

as amplitude instead of intensity is obtained in full-field OCT signal.

It’s easy to prove that this value is fixed for all the axisymmetric aberrations like defocus, astigmatism, spherical aberrations, etc. While for coma with a Strehl ratio of 0.3, the simulated amplitude damping ratio is 13.4 – 53.0 times depending on the spatial position of the adjacent CAs. In another word, the interference signal was severally damped going from the targeted CA to the adjacent CAs. Thus in the camera plane, as shown in figure 5.5(p-r), the interference signal results in a dot product of the aberrated sample PSF with the reference PSF corresponding to the targeted focus CA since the interference with the reference PSFs corresponding to the adjacent CAs are significantly degraded. This actually matches with equation 5.8 for non-aberrated situation, the system PSF could be calculated by the dot product of the sample PSF and the reference PSF. For distorted sample PSF (mostly broadened), its interference with the reference channel conserves the main feature of an unperturbed PSF with only a reduction in the full-fiel OCT signal level. We mentioned “almost” for the resolution conservation, because there are situations in which the product of the reference arm PSF with off-center aberrated sample arm PSF may results in losing some sharpness due to the high side lobes of the Bessel PSF function.

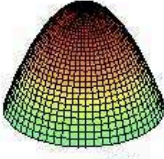
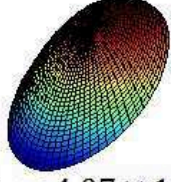
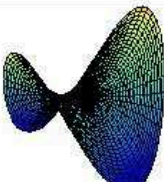
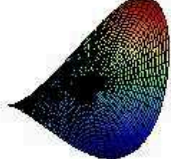
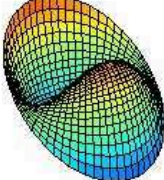
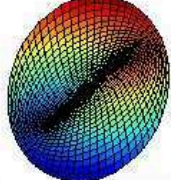
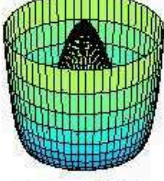
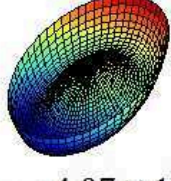
Zernike Mode	Targeted Focus wavefront	Adjacent Wavefront	Amplitude Damping Ratio
Defocus	 $s_t = 0.3$	 $s_a = 4.07 \times 10^{-4}$	27.1
Astigmatism	 $s_t = 0.3$	 $s_a = 4.07 \times 10^{-4}$	27.1
Coma	 $s_t = 0.3$	 $s_a = 4.07 \times 10^{-4}$	13.4 - 53.0
Spherical Aberration	 $s_t = 0.3$	 $s_a = 4.07 \times 10^{-4}$	27.1

Figure 5.8 – Aberrated interference wavefronts and numerical simulations of the Strehl ratio and amplitude damping for interference with targeted CA and adjacent CAs [210]. Defocus, astigmatism, coma and spherical aberration are considered. The damping for coma varies depending on the spatial position of the adjacent CAs.

5.5 Experimental confirmation with extended object

To further validate the theoretical analysis of the lateral resolution merit of FFOCT with spatially incoherent illumination, an USAF resolution target setting at the best focus position is used as an extended sample for FFOCT imaging with different aberrations induced into the FFOCT sample arm. Besides the FFOCT image, the direct reflectance image of the USAF is also recorded simply by blocking the FFOCT reference arm, working as a wide-field microscope. The system resolution and sample arm resolution is then compared through these images.

5.5.1 USAF imaging with defocus

Figure 5.9 shows the experiment results of imaging an USAF resolution target with a FFOCT system that is developed by O. Thouvenin and described in [178]. In this FFOCT system, 40X 0.8NA microscope objectives are used. Defocus aberration is added by shifting the USAF

for $20\mu\text{m}$ ($\text{RMS}=1.85\mu\text{m}$) in the sample arm while the whole reference arm is also shifted for the same amount of length to match the coherence plane with the USAF. The shifting of $20\mu\text{m}$ corresponding to about 6 times of the depth of focus of the objective, thus the direct reflectance image of the USAF shows blur of the patterns after defocus is added. On the contrary, the FFOCT image of the USAF shows that all the patterns are well resolved, meaning that the system resolution is preserved even in presence of important defocus.

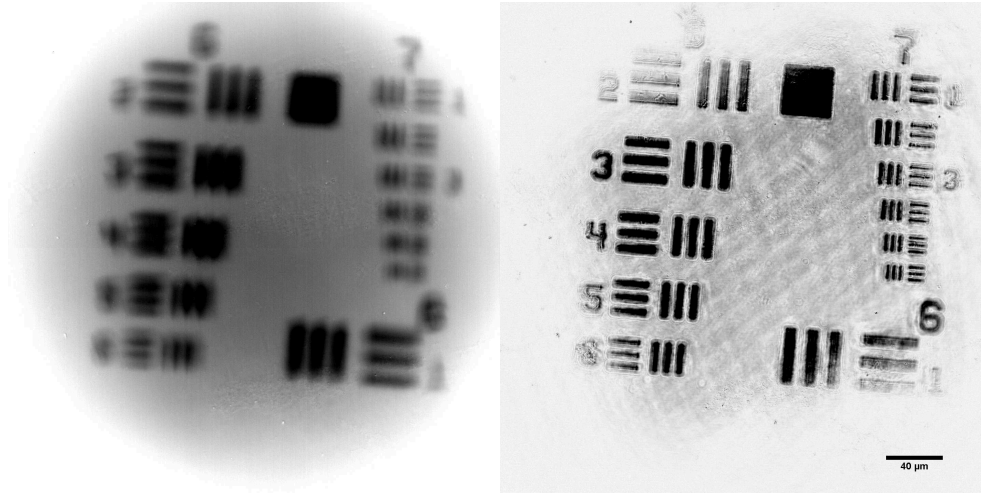


Figure 5.9 – Comparison of the direct reflectance image and FFOCT image of an USAF resolution target after inducing defocus aberration in the sample arm [185]. The direct reflectance image(left) shows the blur of the small patterns on the target while the FFOCT image shows all the patterns are resolved even with defocus added. Scale bar: $40\ \mu\text{m}$.

5.5.2 USAF imaging with random aberration

With a customized AO-FFOCT system, of which the system design will be discussed in details in chapter 6, experiments were also done with USAF by inducing random aberration into the FFOCT sample arm with a LCSLM. Here, a random aberration (root-mean-square (RMS) wavefront error= 0.27λ , corresponding to a Strehl ratio= 0.06 , (see figure 5.10(g)) was induced with the LCSLM in the sample arm by generating and applying random voltages within the adjusting range across the LCSLM pixels. Based on equation ??, the Strehl ratio is calculated by the square of the ratio of mean FFOCT image intensity after and before the aberration was applied. Figure 5.10 shows the sample reflectance images and FFOCT images of the USAF resolution target before and after the random aberration was induced. The reflectance image is blurred after the aberration is added, while there is no obvious blurring of the line patterns in the FFOCT image but only a reduction of the image intensity. The normalized intensity of the selected line in the reflectance image shows a distortion after the aberration was added, while it shows a conservation of the shape for the FFOCT image.

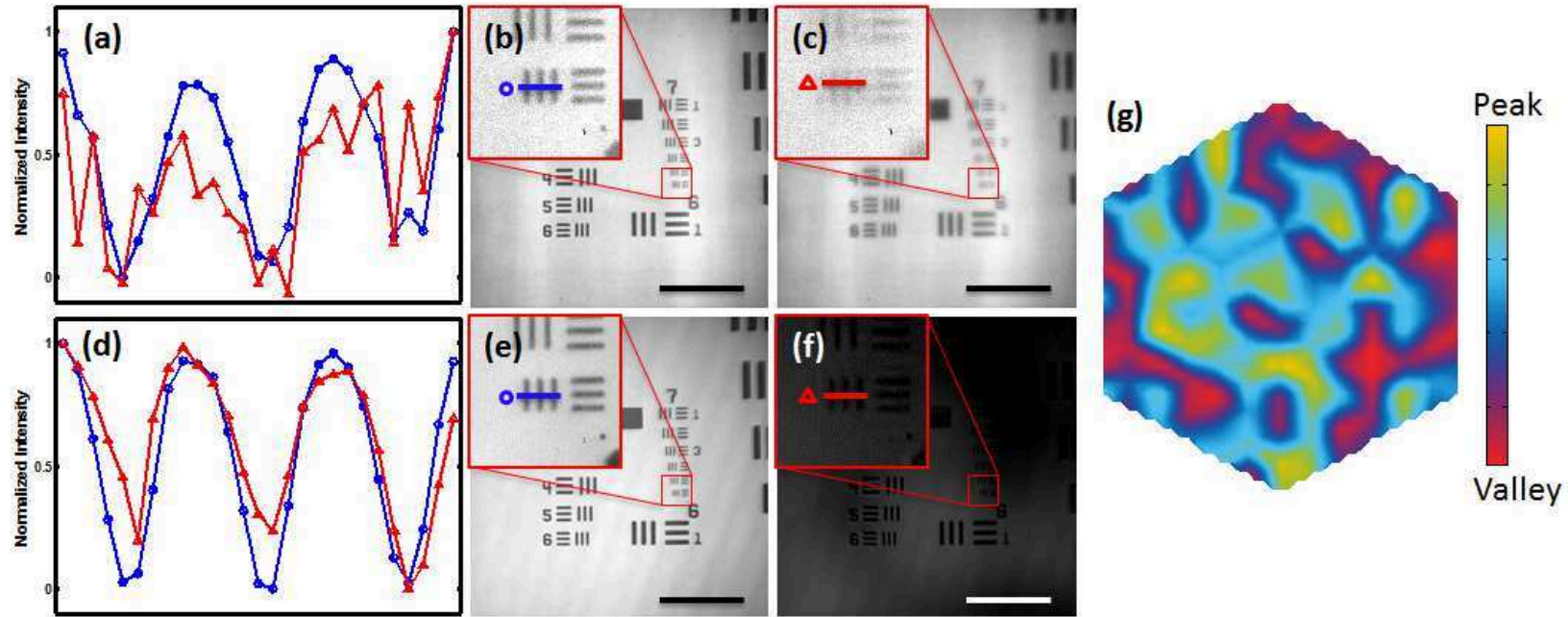


Figure 5.10 – Comparison of the direct reflectance images (b,c) and FFOCT images (e,f) of an USAF resolution target before (b,e) and after (c,f) inducing a random aberration in the sample arm [216]. (a,d) The comparison of the normalized reflectance intensity and FFOCT signal of the selected line without (blue) and with (red) aberration added. The plot of the random aberration pattern is shown in (g). Scale bar: 100 μm .

Adaptive optics FFOCT (AO-FFOCT)

Table of contents

6.1	Simplifying AO for low order aberrations in FFOCT	76
6.1.1	Plane conjugation in AO induce system complexity	76
6.1.2	Non-conjugate AO for eye's low order aberration correction	77
6.1.3	Wavefront sensorless method further simplify the system	77
6.2	The compact AO-FFOCT setup	78
6.3	Aberration correction algorithm	79
6.4	LCSLM-induced aberration correction	80
6.4.1	Non-conjugate AO	80
6.4.2	Conjugate AO	83
6.5	Sample induced aberration correction	83
6.5.1	Ficus leaf experiment: weak aberration correction	83
6.5.2	Mouse brain slice: strong aberration correction	84
6.6	AO-FFOCT retinal imaging of artificial eye model	86

6.1 Simplifying AO for low order aberrations in FFOCT

The ultimate goal of my project is to apply FFOCT for human retinal examinations. As already discussed in section 3.1.2, despite of scattering problems inside the retinal tissues, there are also multi-scale aberrating structures in the eye that could degrade the optical image quality when doing retinal examinations. Thus a wavefront adaptive system is typically needed to achieve diffraction-limited imaging. The basic concept of AO has been discussed in chapter 2. Originally proposed and developed for astronomical optical telescopes to correct the atmosphere-induced aberrations, adaptive optics (AO) has found valuable applications to correct biological tissue-induced aberrations in biological and medical imaging, especially for retinal imaging to visualize cellular structures. AO assisted fundus photography (section 3.2.1), scanning laser ophthalmoscopy (section 3.2.2) and OCT (section 3.2.3) systems have achieved reliable images of cones and rods photoreceptors.

6.1.1 Plane conjugation in AO induce system complexity

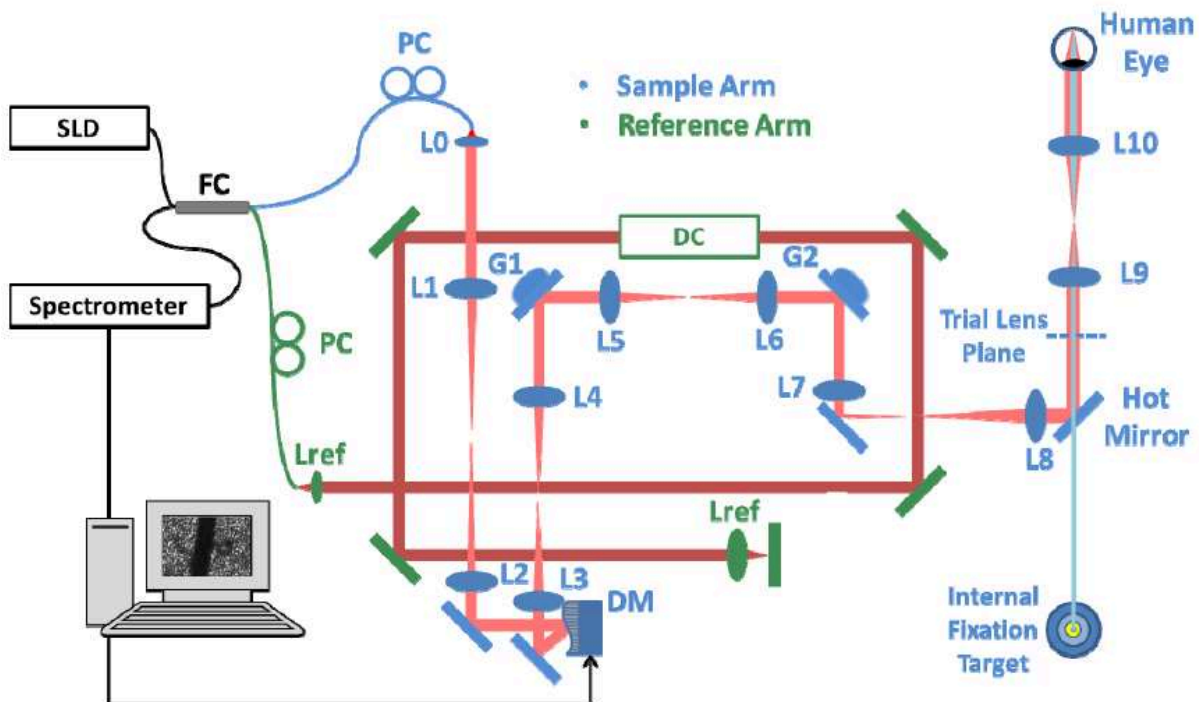


Figure 6.1 – Schematic of a wavefront sensorless AO-OCT system for *in vivo* human retinal imaging [170]. The deformable mirror plane and trial lens plane are all conjugated to the eye pupil plane with lens pairs, increasing the optical path length and system complexity.

In general, the AO part in many systems such as two-photon microscopy [104] or AO-OCT systems (see figure 6.1) [75,170,174,175,217,218] has strict conjugation of the image focal plane of the microscope objective or of the eye pupil with the wavefront sensors or correction devices. For both pupil AO, in which conjugation is done to the pupil plane, and conjugate AO, in which conjugation is done to the plane where the aberrations dominate, a plane is needed for wavefront measurement and the inverse phase mask needs to be applied to the same plane with the conjugated wavefront correctors. The advantages and disadvantages of both conjugations have been discussed in [219]. For high order aberrations, due to the diffractive effects of wave propagation, one cannot rely on simple geometrical optics propagation of the wavefront. In these cases, strict pupil conjugation appears to be mandatory. However, the telescopic systems needed to achieve strict pupil conjugation would increase the system complexity and the optical path length, which would be really difficult for FFOCT system since the two arms in FFOCT have to be balanced within less than one micrometer due to the axial sectioning of FFOCT.

6.1.2 Non-conjugate AO for eye's low order aberration correction

The requirements of strict plane conjugation would appear differently for low order aberrations. As showed already in section 3.1.2, for eye aberrations, the low order Zernike polynomials are actually dominate, meaning that the aberrated wavefront passing though the eye would look like the same during its propagation. So, to develop an AO-FFOCT for human retina examinations, we propose that a transmissive wavefront corrector that could be roughly set in the beam path without strict conjugation would be enough for eye's low order aberration corrections, analogous to commonly used spectacles for correcting eye's myopia and astigmatism. In this way, we would be able to overcome the complex setups realizations for AO-FFOCT.

While different wavefront correctors have been developed and applied for eye's diffraction-limited imaging, they all have pros and cons when considering parameters like temporal bandwidth, reflectivity, mirror diameter, number of actuators, etc [220]. Transmissive liquid crystal spatial light modulator (LCSLM)(section 2.4.2) [92,221–224] would fit for our application. With a large number of pixels and a low control voltage, it can alter the wavefront in transmissive way when light passing through. LCSLMs have already been used in some studies to change the refractive state [223] or to correct the aberrations of the eye [224], but in these cases pupil conjugation using telescopes have been used as this is done in astronomy for a small field of view. The confined 2π phase-modulation range of LCSLM might limit the correction of aberrations with large magnitudes. But the adjusting range would be doubled as the incoming and outgoing beams both induce optical path difference. Finally either phase wrapping could be used to extend the dynamic range [91, 223] or simple visual corrections for defocus and astigmatism could be added to the sample optical path.

6.1.3 Wavefront sensorless method further simplify the system

In most AO systems, direct wavefront measurements are usually demonstrated with a wavefront sensor or coherence-gated wavefront sensing. But due to the lack of generally adaptable wavefront sensors and the inherent complexity of the coherent wavefront sensing, wavefront sensorless methods have also been developed such as metric-based sensorless algorithms, phase

diversity, pupil segmentation, etc (section 2.4.4). As we already discussed in the chapter 5, in FFOCT, aberrations actually do not affect the width of the system PSF but rather the signal level, which is an unexpected property of full-field spatially incoherent interferometry. Therefore, a wavefront sensorless method that relies on the improvement of image quality would be used for the optimization process. The algorithm would be explained in section 6.3. No wavefront sensor is needed which further simplified the AO-FFOCT system.

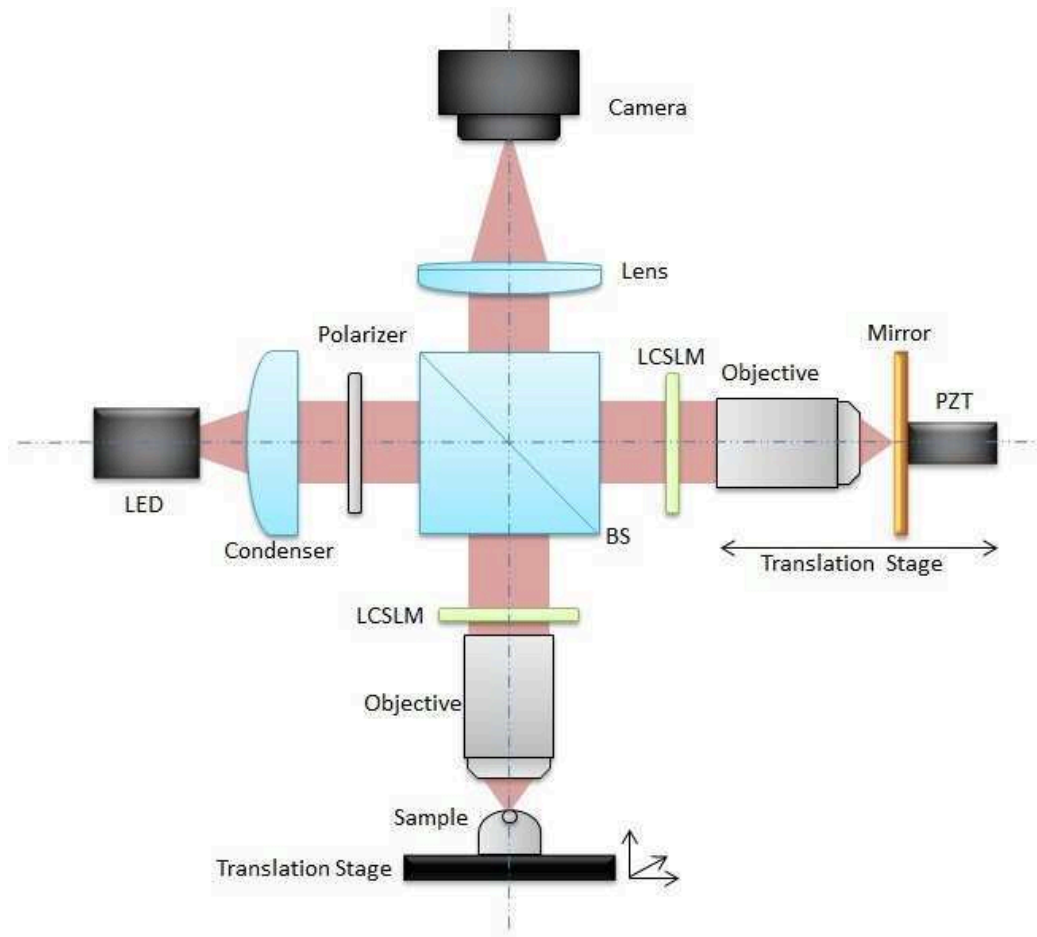


Figure 6.2 – Schematic of AO-FFOCT system coupled with LCSLMs [216]. BS: beamsplitter, LCSLM: liquid crystal spatial light modulator, PZT: piezoelectric transducer.

6.2 The compact AO-FFOCT setup

The AO-FFOCT system schematic is shown in figure 6.2. Based on a Linnik interferometer, a LED with 660nm center wavelength and 25nm bandwidth (Thorlabs) is used as the incoherent light source. The illumination beam is split into the reference arm and the sample arm at a ratio of 50 : 50 with a non-polarizing beamsplitter. Two $4X/0.2NA$ Plan APO objectives (Nikon) are used, one is in the sample arm to simulate the open pupil human eye and the other is in the reference arm. A reference mirror attached to a piezoelectric transducer (PZT) is placed at the focal plan of the objective in the reference arm while the imaging sample would be placed in the sample arm. The back-reflected beams from the reference mirror and the sample are recombined by the beamsplitter and focused with an achromatic doublet lens onto a fast

(150fps) CMOS camera (MV-D1024E-160-CL-12, PhotonFocus). The setup is well aligned to ensure that the focusing of the two arms and their optical paths are matched. The PZT creates a four-phase modulation of the reference mirror and a FFOCT image can be reconstructed with these four corresponding images. Usually several FFOCT images are averaged to improve the signal to noise ratio (SNR). 5 images were used for the experiments described here, requiring about 150ms in total. The system has a field of view of $1.7 \times 1.7 \text{mm}^2$ with the theoretical resolutions of $2 \mu\text{m}$ (lateral) and $7.7 \mu\text{m}$ (axial).

To conduct the wavefront correction, a transmissive LCSLM is inserted into the sample arm beam path at about 2.5cm after the back aperture of the objective lens. Hence no strict plane conjugations are utilized. Another identical LCSLM is also set in the reference arm beam path for dispersion correction. A polarizer is inserted in the illumination path since the LCSLM works only with polarized light. By electronically varying the orientation of the molecules inside the pixels of the LCSLM, the refractive index of the pixels is altered independently from each other, generating variable phase masks to correct the wavefront of the polarized light passing through them.

6.3 Aberration correction algorithm

Since aberrations affect only the signal level without reducing the image resolution in FFOCT, a wavefront sensorless approach based on the FFOCT signal level is used for aberration correction. This method consists of the sequential adjustment of the coefficients of low order orthogonal Zernike polynomial functions applied to the LCSLM to optimize the metric function. The mean intensity of FFOCT image was used as the metric function for LCSLM-induced aberration correction with USAF resolution target as the sample. For in-depth sample-induced aberration correction, the average intensity of the 300 pixels with maximum intensity values in the FFOCT image was used as the metric function. This is due to the mean intensity of the overall image would be less sensitive to the AO process since most parts of the FFOCT image has very low or even no signal. Of course the optimization process could also be restricted to specific region of interest. Indeed anisoplanatism does exist as demonstrated later in figure 6.4, but the experiment results show acceptable correction with this simple AO algorithm. No phase wrapping was used for experiments discussed in this chapter because the magnitude of the wavefront distortions to be compensated was within the dynamical range of the SLM. Coefficients were indeed selected within the adjusting range of the LCSLM. The orthogonality of different Zernike modes ensures that the coefficient of each mode for optimal correction is determined independently [76, 225]. This algorithm has been proposed and used by many groups with different wavefront shaping methods and optimization metrics in specific applications [117, 118, 170], including in FFOCT for defocus aberration correction [181]. For the aberration correction experiments mentioned in this these, only Zernike modes 3 to 8 were optimized just to demonstrate the feasibility of our system and method. For each mode, FFOCT images were taken for 7 different coefficients within the adjusting range. With the extracted metric function values, B-spline interpolations were done and the coefficient that produced the highest metric function was chosen as the correction value.

6.4 LCSLM-induced aberration correction

6.4.1 Non-conjugate AO

To test the performances of the AO-FFOCT system with non-conjugate AO and wavefront sensorless algorithm, experiments of LCSLM-induced aberration correction were first conducted by imaging a negative USAF resolution target. As shown in figure 6.3, in this experiment LCSLM2 were inserted into the sample arm for aberration introduction at about 5cm after the original LCSLM1 which was used for aberration correction, thus there is no well-defined conjugation between the aberration introduction plane and the correction plane. A glass slide was inserted into the reference arm for dispersion compensation. The USAF target was set at the best focus position in the sample arm and a random aberration mask ($\text{RMS}=0.23\lambda$, $\text{Strehl ratio}=0.12$) was generated and applied to the LCSLM2. Figure 6.4(a) shows the original FFOCT image with the added aberration. By using the wavefront correction algorithm and applying the correction phase mask onto LCSLM1, defocus, astigmatism, coma and spherical aberration were corrected successively. Figure 6.4(b)-(g) show the images after each correction with a clearly visible improvement of image quality after each optimization process. The curves in Figure 6.4(h) shows the increase of the metric function and also the mean intensity changes of the corresponding selected regions indicated in Figure 6.4(a,g). The fact that different levels of improvement were achieved for different regions with the same correction phase mask for each Zernike mode implies the existence of anisoplanatism in our experiment. Nevertheless, the mean intensity of the FFOCT image got an increase of 135% after the overall correction, reaching 80% of the non-aberrated FFOCT image, while having diffraction-limited resolution. The experiment was repeated for 3 times with different random aberrations and it results in an average increase of the mean intensity to $78.0\% \pm 2.2\%$ of the non-aberrated image, corresponding to a Strehl ratio of 0.61 ± 0.035 .

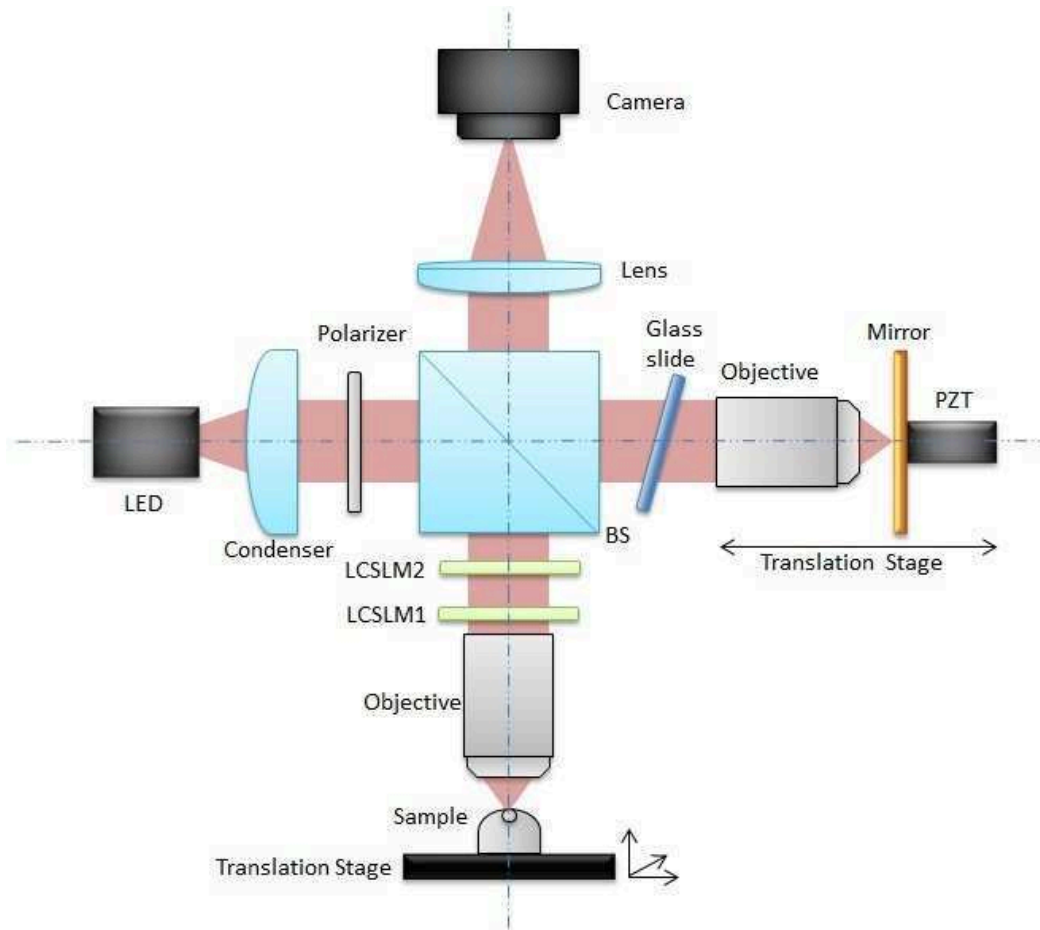


Figure 6.3 – Schematic of adaptive optics FFOCT system for LCSLM-induced aberration correction [216]. LCSLM2 was inserted at 50mm after LCSLM1. For non-conjugate AO experiment, LCSLM2 was used for aberration introduction and LCSLM1 was used for aberration correction. For conjugate AO experiment, LCSLM2 is used for both aberration introduction and correction.

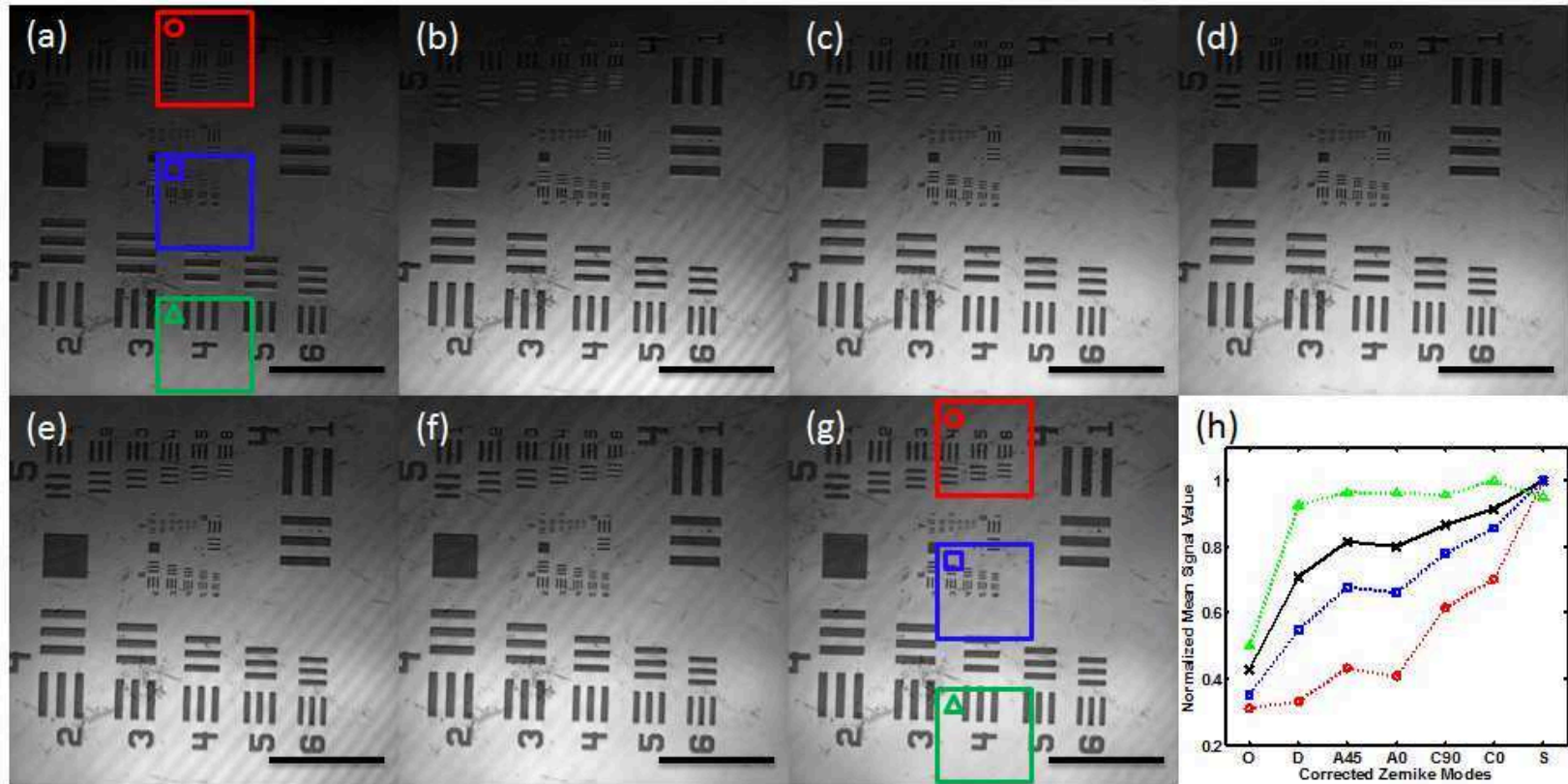


Figure 6.4 – FFOCT images of a negative USAF resolution target during the non-conjugate AO correction process of a random aberration [216]. (a) original image with a random aberration added, (b)-(g) images after defocus, astigmatism 45, astigmatism 0, coma 90, coma 0 and spherical aberration were corrected respectively, (h) graph of the metric function (black curve) increase after each correction step and mean intensity changes (red, blue and green dashed curves) of the corresponding selected regions indicated in (a,g). Scale bar: 350 μ m.

6.4.2 Conjugate AO

For comparison, conjugate AO experiment was conducted by using the same LCSLM for aberration introduction and correction. With the same random aberration induced by LCSLM2, aberration correction was demonstrated also on LCSLM2 itself. With the same algorithm, Zernike modes 3-8 was corrected by applying net voltages of random pattern plus the Zernike modes to LCSLM2. As shown in figure 6.5, the whole correction result in the mean intensity of the FFOCT image reaching 86% of the non-aberrated FFOCT image. Again, the three repeated experiments result in an average increase of the mean intensity to $84.3\% \pm 2.1\%$ of the non-aberrated image, corresponding to a Strehl ratio of 0.71 ± 0.036 .

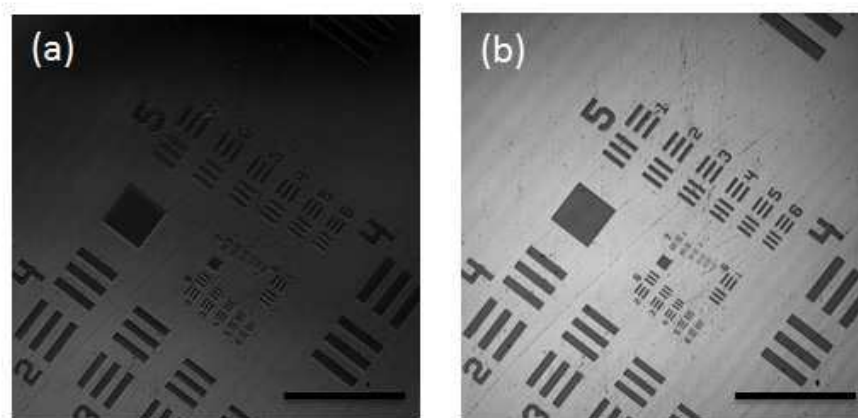


Figure 6.5 – FFOCT images of a negative USAF resolution target before and after the conjugate AO correction process of a random aberration [216]. (a) original image with a random aberration added, (b) image after defocus, astigmatism 45, astigmatism 0, coma 90, coma 0 and spherical aberration were corrected. Scale bar: $350\mu\text{m}$.

6.5 Sample induced aberration correction

6.5.1 Ficus leaf experiment: weak aberration correction

Due to the spatial variations of refractive index within biological samples and surface topography, aberration distortion is severe when imaging into the sample volume. In order to further demonstrate the feasibility of our system and method even for weak aberrations correction, experiments of sample induced aberrations corrections were done with a ficus leaf. The system setup described in figure 6.2 was used here. By imaging at a depth of $75\mu\text{m}$ under the leaf surface only weak aberrations are induced and we can thus check the sensitivity of our correction approach; the low order contents of the self-induced sample aberrations were corrected step by step with the aforementioned methods. As showed in figure 6.6, the optimized image (figure 6.6(b)) shows an intensity increase compared with the original image (figure 6.6(a)) and from the zoomed in images, more structured information appears. This is due to the fact that the correction process increased the SNR and more signals that were buried by the noise before appear after the AO correction. The graph of the metric function while adjusting the coefficients of each Zernike mode is displayed in figure 6.6(c). The highest positions of each curve

correspond to the coefficients used for the optimal correction of each mode. Figure 6.6(d) shows the increase of metric function. The whole correction process results in 13.3% improvement of the metric function. The metric function improvement increases to 35.5% when imaging deeper at $120\mu\text{m}$ under the leaf surface in another experiment.

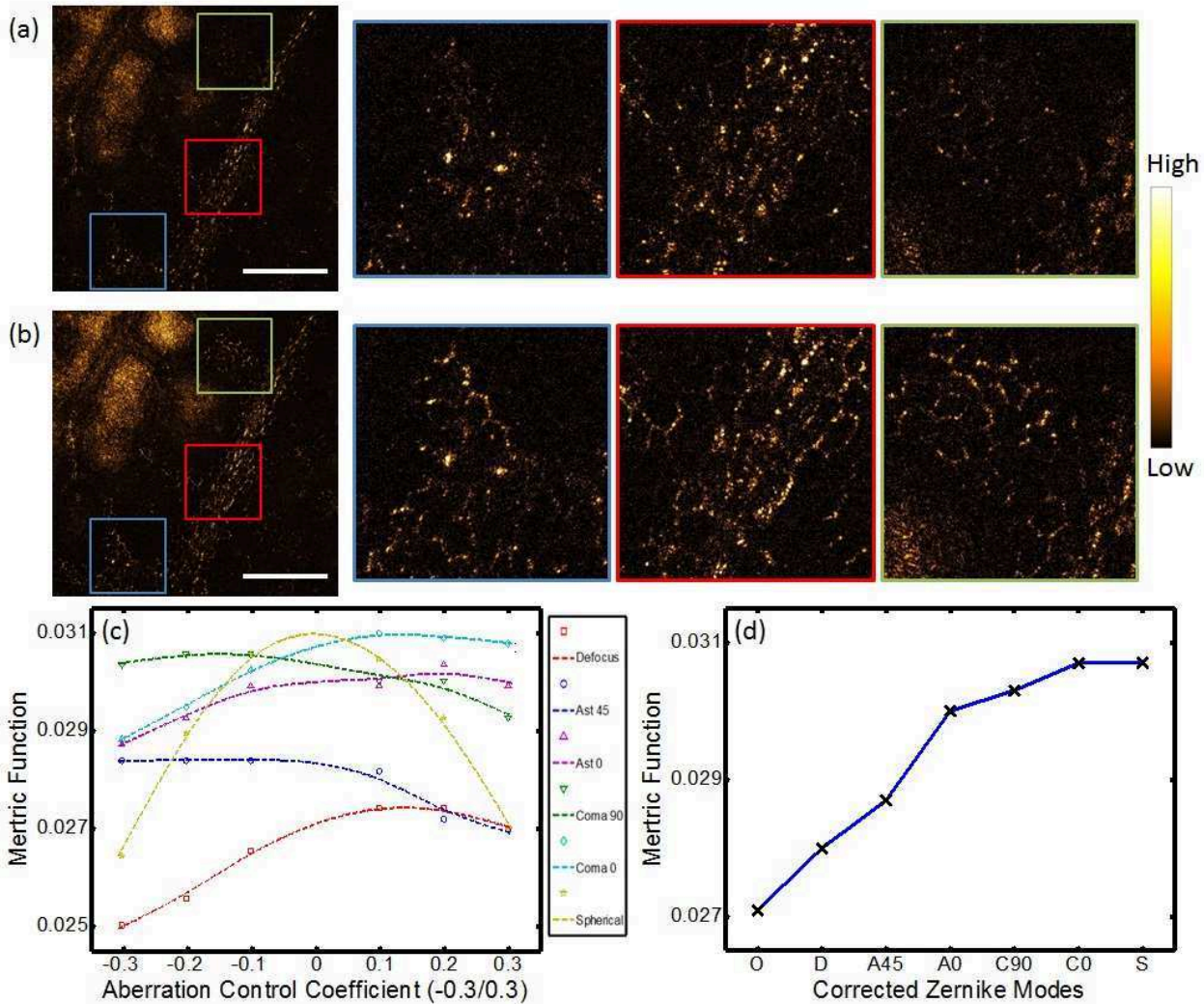


Figure 6.6 – Comparison of FFOCT images of a ficus leaf (a) before and (b) after sample self-induced aberration was corrected when imaging at a depth of $75\mu\text{m}$. [216]. (c) Graph of the metric function during the optimization process and (d) graph of the metric function increase after each correction step. Scale bar: $500\mu\text{m}$, Zoomed in area: $425 \times 425\mu\text{m}$.

6.5.2 Mouse brain slice: strong aberration correction

After showing the ability of this AO-FFOCT approach to optimize the signal even with a low level of aberration, we checked another biological tissue of relevance that suffers from strong scattering and stronger aberrations: the brain tissue, where FFOCT signal is usually strongly reduced when imaging deep in the sample. Experiments were conducted with a fixed mouse brain tissue slice to correct the wavefront distortion. Imaging was performed at $50\mu\text{m}$ under the brain tissue surface without liquid matching fluid and the results are shown in figure 6.7. The

high-signal fiber-like myelin structures appeared much more clearly after the whole correction process because of the increased SNR; indeed the metric function was increased by 121%.

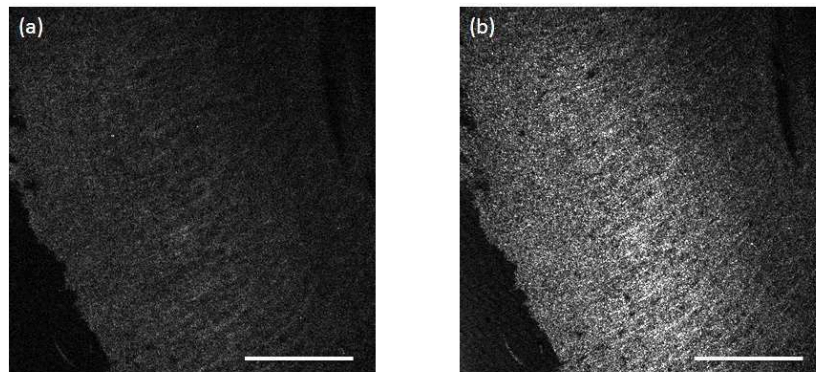


Figure 6.7 – Comparison of FFOCT images of fixed mouse brain tissue slice before (a) and after (b) sample self-induced aberration was corrected when imaging at a depth of $50\mu m$ [216]. Scale bar: $500\mu m$.

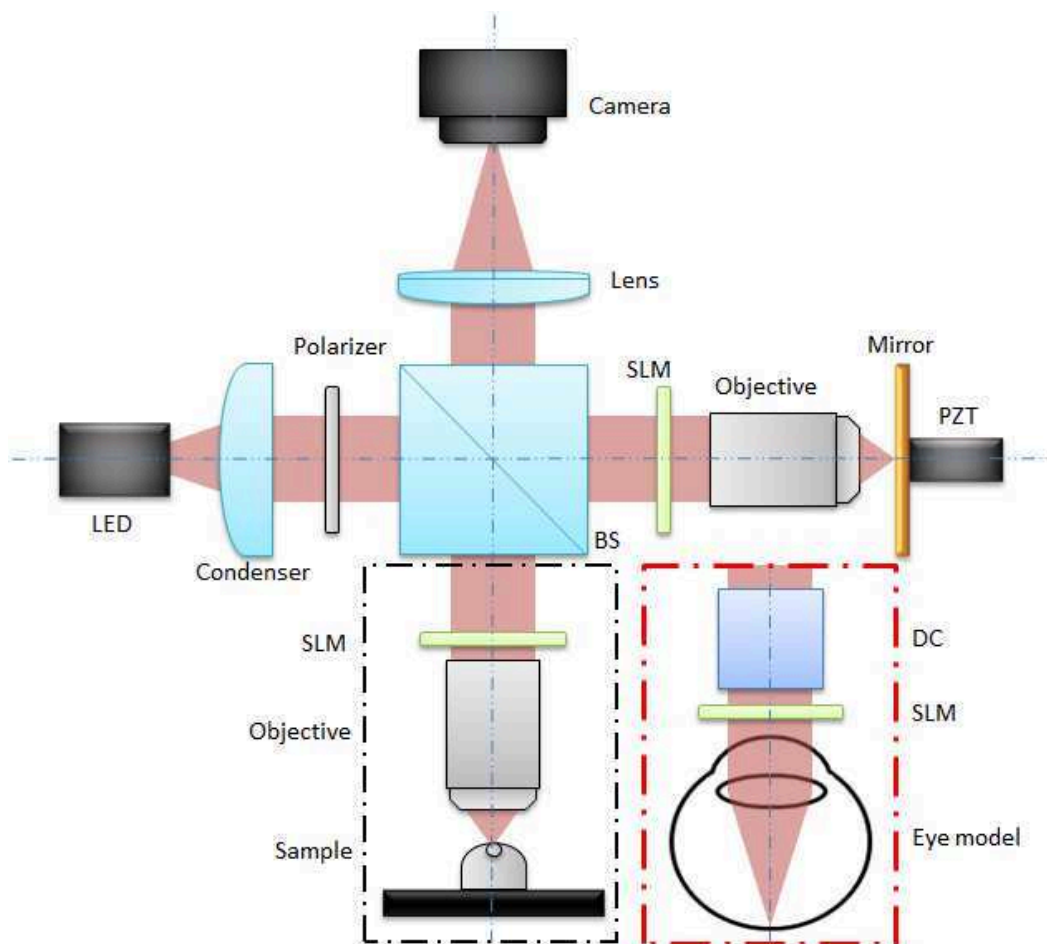


Figure 6.8 – Schematic of the AO-FFOCT system for retinal imaging with an artificial eye model [226]. the original sample arm (black dashed line box) is replaced by the artificial eye model with a dispersion compensation (DC) block (red dashed line box).

6.6 AO-FFOCT retinal imaging of artificial eye model

The above studies that showing low order aberration correction in a simple manner for FFOCT opens the path to a straightforward implementation of AO-FFOCT for retinal examinations in the future. In the case of retinal examinations, we can restrict aberration correction to the main aberrations (e.g. focus and astigmatism) that will improve the SNR and skip the high order aberrations. Ultimately, the lens in the eyeball will play the role of the objective used in the sample arm in our experiments, therefore path and dispersion compensation [227] will need to be applied taking into consideration of the eye characteristics. To demonstrate the feasibility of the our FFOCT system for retinal imaging and also the AO part for eye aberration correction, an artificial eye model [228] with solid-state tissue phantom that have realistic artificial retinal layers are used for the first demonstration of retinal imaging.

Since the eye lens would be used as the objective in the sample arm in FFOCT for beam focusing to the retina, as shown in figure 6.8, the AO-FFOCT setup would need to be modified. Compare with the setup shown in figure 6.2, the original sample arm (figure 6.8 (black dashed line box)) will be replaced by the artificial eye model and a tube of water is inserted in front for the dispersion compensation with the reference arm (figure 6.8 (red dashed line box)).

By translating the model eye along the optical axis, three retina layers were detected. The corresponding FFOCT images are displayed in figure 6.9(a-c). Based on the second layer, the model eye self-induced aberrations corrections were done to improve the image signal level by using the same algorithm as described in section 6.3. After the optimization process, the improved FFOCT retinal images are shown in figure 6.9(d-f). The curves in figure 6.9(g) shows the average image intensity of the FFOCT images along different depth while the peaks indicating the three detected layers. The signal level for all the layers is increased after aberration correction. Taking the second layer as an example, the signal level has increased by 48% after subtracting the background noise.

Although we could successively achieve the FFOCT imaging of various retinal layers in this artificial eye model, it is really time consuming for the OPL matching as we have to translate the eye model along the optical axis with micrometer steps. To apply FFOCT for *in vivo* human retinal imaging, this would be impossible as the eye itself has uncontrollable motions. Thus, easy and fast OPL matching would be essential for *in vivo* human retinal imaging, which will be discussed in the following part of this these.

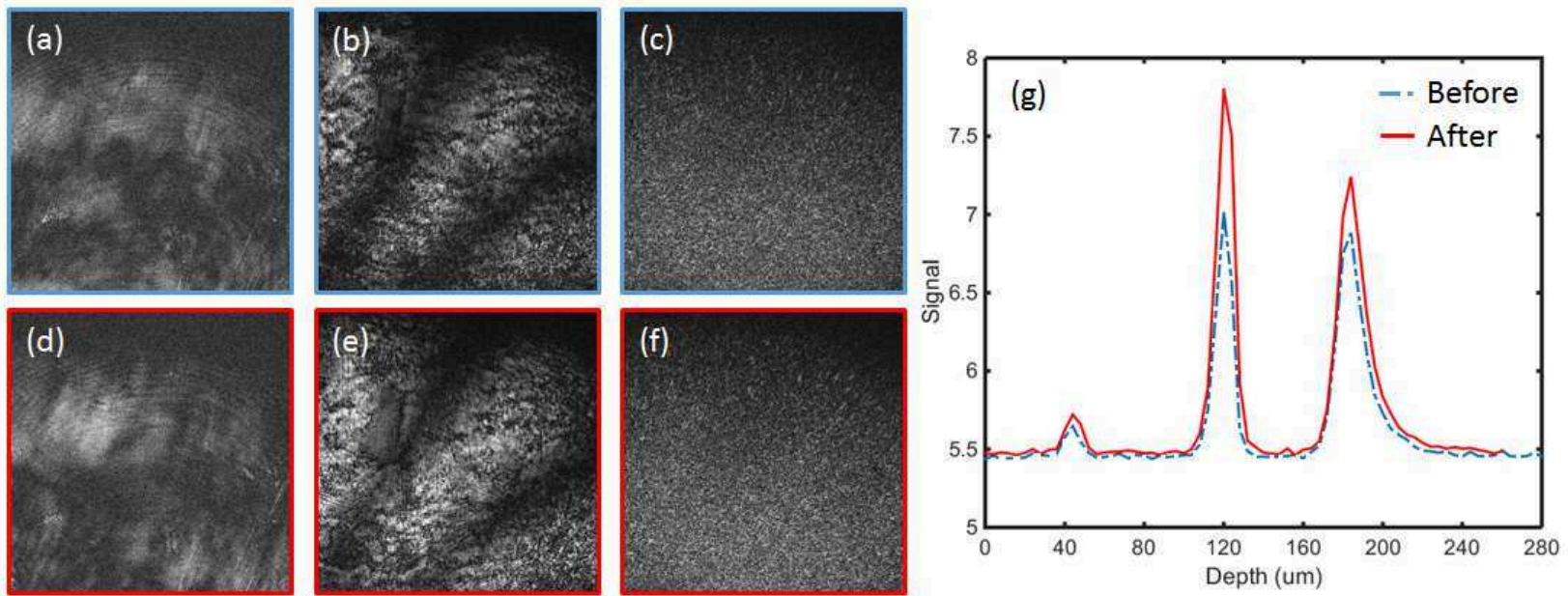


Figure 6.9 – AO-FFOCT retinal image of an artificial eye before and after aberration correction [215].(a-c) FFOCT images of three retinal layers before aberration correction. (d-f) FFOCT images of the corresponding three retinal layers after aberration correction with the LCSLM. (g) The curves showing the average signal level along different depth in the retinal layers before and after aberration correction.

Part III

In vivo Human Retinal Imaging with FFOCT

Combing FFOCT with SDOCT for *in vivo* human retinal imaging

Table of contents

7.1	Introduction	92
7.2	Combining FFOCT with SDOCT	93
7.3	Eye safety analysis	96
7.4	System performance validation with artificial eye model	99
7.5	<i>In vivo</i> human retinal imaging	100
7.5.1	FFOCT retinal imaging of the fovea	100
7.5.2	FFOCT retinal imaging of retinal near periphery	103

7.1 Introduction

Following all the studies we have demonstrated in part II of this thesis, the final goal is to apply FFOCT for *in vivo* high resolution human retinal imaging. In chapter 5, both theoretical analysis and experimental validation have shown the spatial resolution merit of FFOCT that the PSF width is independent of geometrical aberrations with only the signal level reduction by using the spatially incoherent illumination. Thus in terms of human retinal imaging that aberration would exist due to the imperfections of the cornea and lens, FFOCT should keep the near diffraction-limited lateral resolution to resolve cellular structures. Since FFOCT is detecting the amplitude, the signal reduction ratio is proportional to the square root of the Strehl ratio. Therefore, only aberrations with large values would affect the FFOCT image quality. The studies showed in chapter 6 provide a much simplified AO-FFOCT system design, that no strict pupil conjugation is implemented for the wavefront corrector with the aberration origin plane with a wavefront sensorless method. This design is proposed for low order aberration correction like human eye. The system is quite compact with a transmissive wavefront corrector implemented, which is essential for FFOCT imaging to balance the sample arm and reference arm within micrometers. For human eyes, in which only low order aberrations like defocus and astigmatism dominate, AO-FFOCT imaging by correcting large defocus and astigmatism would be enough to retrieve back the image quality. While for good eyes that no obvious aberrations exist, high resolution FFOCT retinal imaging would be possible even without wavefront correction.

To successfully apply FFOCT for *in vivo* human retinal imaging, there are still several obstacles that need to be resolved besides eye aberration: the OPL matching and eye motions. As discussed in section 6.6, while imaging different layers of artificial retinal layers, it is really time consuming to translate the model eye along the optical axis with micrometer steps to match the OPL of the reference arm with various retinal layers. This manipulation is obviously impossible for *in vivo* experiments as the eye itself exhibits various motions and it cannot be really static for minutes during OPL matching process. What we need would be a real-time indicator of the OPL matching with different retinal layers during *in vivo* experiments. For this reason, we proposed a combination of FFOCT with traditional SDOCT so that the OPL could be matched by overlapping the images of the FFOCT reference mirror with different retinal layers through the cross-sectional OCT image by translating the imaging system. With a new fast speed camera working up to 750 Hz implemented, the eye motions are considered to be stabilized enough during the image acquisition, meaning that the OPL difference does not exceed a small fraction of the wavelength (1/10 typically).

7.2 Combining FFOCT with SDOCT

The combined system schematic is showed in figure 7.1: A customized FFOCT system is combined with the Thorlabs GANYMEDE-II SDOCT system. In the FFOCT part, a LED with $\lambda = 850nm$ center wavelength and $30nm$ bandwidth (Thorlabs) is used as the incoherent light source, giving an axial resolution of $8\mu m$ in water. An Olympus 10X/0.25NA Plan Achromat objective is used in the reference arm with a silicon mirror supported by a piezoelectric transducer placed at the focal plan of the objective. Since the FFOCT resolution is not sensitive to aberrations and only the signal level is damped while only low order aberrations dominate in human eyes, a transmissive adaptive liquid lens [99], which is for only defocus and astigmatism correction, is designed to be installed in the sample arm (not used for the experiments demonstrated in this thesis). The human eye is supposed to be aligned in the sample arm along the optical axis with the human head pressed against the headrest for minimizing head movements. Dispersion is balanced with a glass window between the microscope objective in the reference arm and the human eye. The back-reflected beams from the two arms are combined and imaged onto a high-speed ($750fps$) CMOS camera (Q-2A750-Hm/CXP-6, ADIMEC) for FFOCT imaging, the system sensitivity is about $77dB$ as calculated in section 4.3.3. The Thorlabs GANYMEDE-II SDOCT system uses a broadband SLD with centre wavelength of $930nm$, giving an axial resolution in water of $4.5\mu m$. The system comes with a scanning system kit that contains X and Y scanners while the reference arm is customizable. With the system working at the highest scan rates of $36kHz$, the SDOCT has a sensitivity of about $96dB$.

As it is illustrated in figure 7.1, the two OCTs are combined by joining the sample arm of the SDOCT system with the illumination path of the FFOCT through a dichroic mirror. The reason why we are not combing the SDOCT sample arm through the FFOCT sample arm in front of the eye is that, the dichroic mirror used for beam combination has various coating films that will induce multiple reflections for only one arm of the FFOCT. This results in the unbalance of the wavefront property between the sample arm and reference arm in FFOCT, degrading the FFOCT imaging performance. Thus adding the dichroic mirror in the illumination path will avoid this unbalance effects. The drawback of the system design is that the eye pupil would be far from the scanners in the SDOCT, limiting the SDOCT beam scanning range on the human retina. The combined system is mounted on a platform with 3-dimensional mobility offered by precise translating motors. The OPL of SDOCT customized reference arm is matched with the OPL of the SDOCT sample arm to the silicon mirror in the FFOCT reference arm. In this way, we are able to take advantages of the larger depth of field of SDOCT cross-sectional image for real-time matching the OPL of the FFOCT, which is relatively difficult to be balanced within $1\mu m$ for the two arms with different geometries, by overlapping the SDOCT image of the FFOCT reference mirror and the various retinal layers through moving the whole system while the human eye is looked into the system on axis. Theoretically, by simultaneously recording with both FFOCT and SDOCT, the SDOCT cross-sectional images will offer the depth information where *en face* FFOCT images are taken. For in vivo experiments we have conducted, the FFOCT camera is working at a speed of $400Hz$. With 2-phase modulation, the FFOCT images can be recorded at a frequency of $200Hz$, which is fast enough to freeze the eye motion during an image acquisition according to the studies demonstrated in [147, 229]. The effects of the lateral eye movements on an image stack are then corrected with ImageJ plugin "Template Matching" [230] and several images are averaged to improve the SNR.

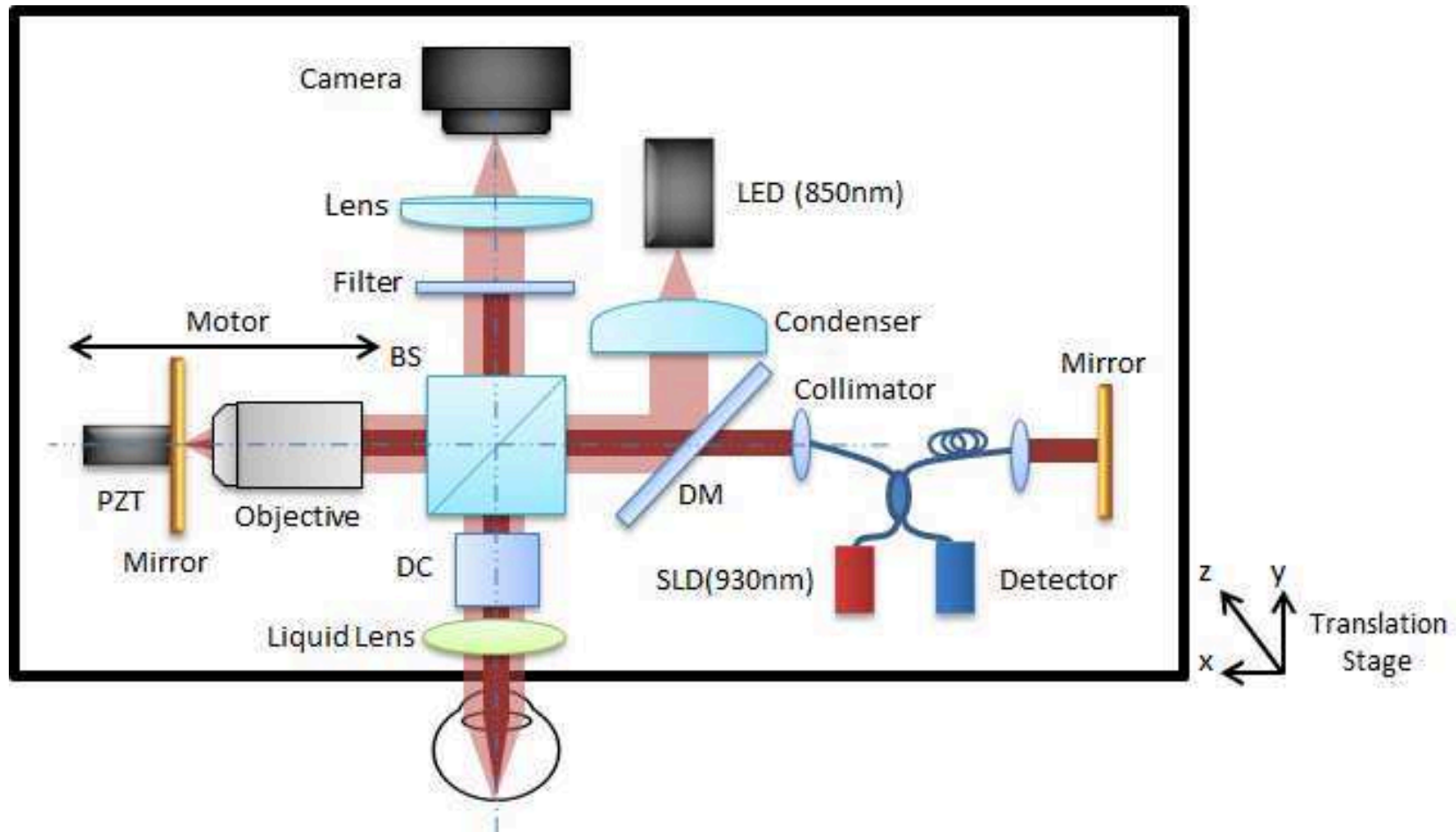


Figure 7.1 – Schematic of the combined system of FFOCT with SDOCT [231]. The SDOCT sample arm is combined with FFOCT illumination path with a dichroic mirror. OPLs are matched between the SDOCT reference arm with SDOCT sample arm to the FFOCT reference mirror. Both systems can work independently but simultaneously. The combined system is mounted on a platform with 3-dimensional translating mobility. BS: beamsplitter; DC: dispersion compensation; DM: dichroic mirror.

Table 7.1 – Maximum Permissible Exposure (MPE) for Extended Source Ocular Exposure to a Laser Beam for Wavelengths from 700nm to 1400nm [232]

	Wavelength λ (nm)	Exposure Duration t (s)	MPE		Notes	
			Retina (J·cm ⁻²)	Cornea (W·cm ⁻²) (J·cm ⁻²) except as noted		
Near Infrared	700 to 1050	10 ⁻¹³ to 10 ⁻¹¹	1.0 C _E × 10 ⁻⁷	-	-	NOTE 1 NOTE 2 NOTE 3
		10 ⁻¹¹ to 5 × 10 ⁻⁶	2.0 C _A C _E × 10 ⁻⁷	-	-	
		5 × 10 ⁻⁶ to T ₂	1.8 C _A C _E t ^{0.75} × 10 ⁻³	-	-	
		T ₂ to 30,000	-	1.8 C _A C _E T ₂ ^{-0.25} × 10 ⁻³	-	
	1050 to 1200	10 ⁻¹³ to 10 ⁻¹¹	1.0 C _C C _E × 10 ⁻⁷	-	-	NOTE 1 NOTE 2 NOTE 3
		10 ⁻¹¹ to 13 × 10 ⁻⁶	2.0 C _C C _E × 10 ⁻⁶	-	-	
		13 × 10 ⁻⁶ to T ₂	9.0 C _C C _E t ^{0.75} × 10 ⁻³	-	-	
		T ₂ to 30,000	-	9.0 C _C C _E T ₂ ^{-0.25} × 10 ⁻³	-	
	1200 to 1400	10 ⁻¹³ to 10 ⁻¹¹	1.0 C _C C _E × 10 ⁻⁷	-	-	NOTE 1 NOTE 2 NOTE 3 NOTE 5
		10 ⁻¹¹ to 13 × 10 ⁻⁶	2.0 C _C C _E × 10 ⁻⁶	-	0.3 K _λ	
		13 × 10 ⁻⁶ to 10 ⁻³	9.0 C _C C _E t ^{0.75} × 10 ⁻³	-	0.3 K _λ + 0.56 t ^{0.25} - 0.1	
		10 ⁻³ to 4		-	0.3 K _λ + 0.7	
		4 to 10		-		
		10 to T ₂		-		
T ₂ to 30,000		-	9.0 C _C C _E T ₂ ^{-0.25} × 10 ⁻³	0.03K _λ + 0.07 [W·cm ⁻²]	NOTE 6	

NOTE 1—See Table 8a and Table 8b for limiting aperture and Table 9 for measurement aperture.
 NOTE 2—See Table 6a for the wavelength dependent correction factors C_A and C_C and parameter K_λ.
 NOTE 3—See Table 6b for the extended source correction factor C_E and time T₂.
 NOTE 4—The MPE for 10⁻¹³ s to 10⁻¹¹ s does not include the factor C_A for this wavelength range.
 NOTE 5—The lower MPE considering retinal and corneal effects must be chosen. The MPEs must be in the same units.
 NOTE 6—For durations greater than T₂, these limits must not exceed the applicable skin MPE.

7.3 Eye safety analysis

The instrument safety analysis is crucial as we are going to apply the system for *in vivo* human retinal imaging. Based on the American National Standard for Safe Use of Lasers (ANSI Z136.1-2014) [232], the ocular exposure safety is carefully analysed. Since both FFOCT and SDOCT is used in our system, the maximum permissible exposures (MPE) for both light sources are calculated.

For FFOCT imaging, the extended light source has a wavelength of $\lambda = 850nm$ with a bandwidth of $30nm$. As the wavelength is within the range of $700nm$ to $1400nm$, only thermal hazard need to be considered based on table 7.1. Before calculate the MPE, several parameters need to be decided. According to table 7.2, with a center wavelength of $850nm$ (the shortest wavelength is $825nm$), the wavelength correction factor:

$$C_A = 10^{0.002(\lambda-700)} = 1.78 \quad (7.1)$$

With the current system design, the FFOCT system magnification is:

$$M = \frac{f_{lens}}{f_{eye}} = \frac{400mm}{16.7mm} \approx 24times, \quad (7.2)$$

in which f_{lens} is the focal length of the tube lens in front the camera and f_{eye} is object focal length of a human eye [233]. With the Adimec CMOS camera, the active sensor area size is:

$$A_{camera} = (1440pixels \times 12um)^2 = 17.28mm \times 17.28mm \quad (7.3)$$

as the camera have 1440×1440 pixels with a pixel size of $12um$. With a field stop in the illumination path, we have limiting a circular imaging area on the retina that just fills the camera sensor area. Thus, the illumination area on the retinal would have a diameter of:

$$d_r = \frac{17.28mm}{24} = 720um. \quad (7.4)$$

Thus, the full angular subtense of retinal area would be calculated as:

$$\alpha = \arctan \frac{720um}{16.7mm} = 43mrad. \quad (7.5)$$

As $\alpha_{min} = 1.5mrad < \alpha = 43mrad < \alpha_{max} = 100mrad$, according to table 7.3, the extended source correction factor:

$$C_E = \frac{\alpha}{\alpha_{min}} = \frac{43}{1.5} = 28.67. \quad (7.6)$$

And the parameter T_2 , the exposure duration beyond which the thermal MPE for an extended source is constant in term of irradiance, is:

$$T_2 = 10 \times 10^{(\alpha-1.5)/98.5} = 26.38s. \quad (7.7)$$

Thus, the MPE for FFOCT illumination could be calculated based on table 7.1.

- If we consider the extreme case that the illumination is continuous up to 30000s,

$$MPE_c = 1.8C_A C_E T_2^{-0.25} \times 10^{-3} = 1.8 \times 1.78 \times 28.67 \times 26.38^{-0.25} = 40.53 mW/cm^2. \quad (7.8)$$

- If the illumination is less than T_2 , suppose 10s,

$$MPE_{10} = 1.8C_A C_E t^{-0.25} \times 10^{-3} = 1.8 \times 1.78 \times 28.67 \times 10^{-0.25} = 51.66 mW/cm^2. \quad (7.9)$$

- In the *in vivo* human retinal imaging experiments, 40 tomographic images will be acquired continuously with 2-phase modulation and 400Hz camera speed, the imaging time would be 0.2s, which is less than T_2 ,

$$MPE_{0.2} = 1.8C_A C_E t^{-0.25} \times 10^{-3} = 1.8 \times 1.78 \times 28.67 \times 0.2^{-0.25} = 137.36 mW/cm^2. \quad (7.10)$$

For our experiment setup, the irradiance is measured to be only $8 mW/cm^2$ in front of the human cornea, more than 5 times lower than the MPE for continuous illumination and more than 17 times lower than the MPE for a illumination duration of an imaging period. Note that, this calculations also satisfied with the newly released American National Standard for Ophthalmics - Light Hazard Protection for Ophthalmic Instruments (ANSI Z80.36-2016) [234].

Table 7.2 – Wavelength Dependent Parameters and Correction Factors [232]

Parameter/Correction Factor	Wavelength λ (nm)	Graph	Notes
C_A	1.0	400 to 700	Fig. 8a NOTE 2
	$10^{0.002(\lambda-700)}$	700 to 1050	
	5.0	1050 to 1400	
C_B	1.0	400 to 450	Fig. 8b NOTE 2
	$10^{0.02(\lambda-450)}$	450 to 600	
C_C	1.0	1050 to 1150	Fig. 8c NOTE 2
	$10^{0.018(\lambda-1150)}$	1150 to 1200	
	$8 + 10^{0.04(\lambda-1250)}$	1200 to 1400	
T_1	$10 \times 10^{0.02(\lambda-450)}$	450 to 500	Fig. 9a NOTES 1, 2
K_λ	$10^{0.01(1400-\lambda)}$	1200 to 1400	Fig. 15 NOTE 2
NOTE 1— $T_1 = 10$ s for $\lambda = 450$ nm and $T_1 = 100$ s for $\lambda = 500$ nm.			
NOTE 2—Wavelengths must be expressed in nanometers for calculations.			

Table 7.3 – Extended Source Parameters and Correction Factors for Wavelengths from 400nm to 1400nm [232]

Parameter/Correction Factor		Graph	Notes
α_{min}	1.5 mrad		
α_{max}	5 mrad	$t < 625 \mu s$	Fig. 14 NOTES 1, 2
	$200 t^{0.5}$ mrad	$625 \mu s \leq t < 0.25 s$	
	100 mrad	$0.25 s \leq t$	
C_E	1.0	$\alpha < \alpha_{min}$	Circular Sources NOTES 1, 4
	α / α_{min}	$\alpha_{min} \leq \alpha < \alpha_{max}$	
	$\alpha^2 / (\alpha_{max} \alpha_{min})$	$\alpha_{max} \leq \alpha$	
C_E^*	1.0	$\alpha_x < \alpha_{min}$ and $\alpha_y < \alpha_{min}$	*Non-Circular Sources NOTES 1, 4, 5
	$(\alpha_x + \alpha_y) / (2 \cdot \alpha_{min})$	$\alpha_x < \alpha_{max}$ and $\alpha_y < \alpha_{max}$	
	$\alpha_x \cdot (\alpha_{max} + \alpha_y) / (2 \cdot \alpha_{max} \cdot \alpha_{min})$	$\alpha_x \geq \alpha_{max}$ and $\alpha_y < \alpha_{max}$	
	$\alpha_x \cdot \alpha_y / (\alpha_{max} \cdot \alpha_{min})$	$\alpha_x \geq \alpha_{max}$ and $\alpha_y \geq \alpha_{max}$	
T_2	$10 \times 10^{(\alpha-1.5)/98.5}$	Fig. 9b	NOTES 1, 3

NOTE 1— α , α_{min} and α_{max} are expressed in mrad.
 NOTE 2—Express exposure duration t in seconds to calculate α_{max} .
 NOTE 3— $T_2 = 10$ s for $\alpha < 1.5$ mrad and $T_2 = 100$ s for $\alpha > 100$ mrad. For elongated sources, T_2 is based on the arithmetic mean of the two source dimensions with each limited to a minimum of α_{min} and a maximum of 100 mrad.
 NOTE 4—When either source dimension is larger than α_{max} measurement of the corneal radiant exposure to compare with the calculated MPE must be made with an open field detector since the effective source radiance does not exceed that calculated for a source size of α_{max} .
 NOTE 5— α_x and α_y define the full angle dimensions of the source at 1/e peak of irradiance points. α_x is the larger dimension and α_y is the smaller. When either dimension is smaller than α_{min} , it is set equal to α_{min} .

For SDOCT, the illumination has a wavelength of 930nm. According to section 5.2.1 in ANSI standard for Ophthalmics - Light Hazard Protection for Ophthalmic Instruments [234], for an ophthalmic instrument that images the retina or the anterior segment of the eye by using a small moving irradiated area, for the thermal hazard prevention, the radiation energy entering the eye shall be less than or equal to 1.32mW. In our combine system, the energy entering the eye is only 250uW. Thus it is far more than safe for SDOCT illumination.

While imaging the retina by the combined system of FFOCT and SDOCT simultaneously, not only each light source alone should be below the applicable limits, also it should be satisfied with the requirements based on section 5.4.3 in ANSI standard for Ophthalmics - Light Hazard Protection for Ophthalmic Instruments [234] for multiple source instruments:

$$\frac{E_{SDOCT}}{MPE_{SDOCT}} + \frac{E_{FFOCT}}{MPE_{FFOCT}} = \frac{0.25mW}{1.32mW} + \frac{8mW/cm^2}{40.53mW/cm^2} = 0.387 \leq 1, \quad (7.11)$$

meaning that our system illumination is under the safety limitation level.

7.4 System performance validation with artificial eye model

With the system and methods described above, retinal imaging is first done with the artificial eye model to validate the system performance before moving to *in vivo* human experiments. The artificial eye model is mounted on axial in the FFOCT sample arm. By translating the system along the optical axis, cross-sectional SDOCT image starts to show the artificial retinal layers (figure 7.2 (a)). Since the OPL of the SDOCT reference arm is mached with its sample arm until the FFOCT reference mirror, thus the SDOCT image of the FFOCT reference mirror always exist at a fixed location (figure 7.2 (b)). The OPL of FFOCT is matched by overlapping the SDOCT mirror image with the SDOCT image of different artificial retinal layers by translating the system (figure 7.2 (c)). And in the cases when the OPL is matched, the FFOCT *en face* images are recorded. Figure 7.2 (d-f) are the *en face* FFOCT retinal images of the artificial eye model corresponding to the retinal layers showing in figure 7.2 (a) from the top to the bottom. Compared with the artificial eye model retinal imaging showed in section 6.6, which takes much longer time to blindly scan along the depth with micrometer steps to search for the retinal layers, the method demonstrated here with the combined system offers a real-time method for the OPL matching, which would help a lot for *in vivo* experiments.

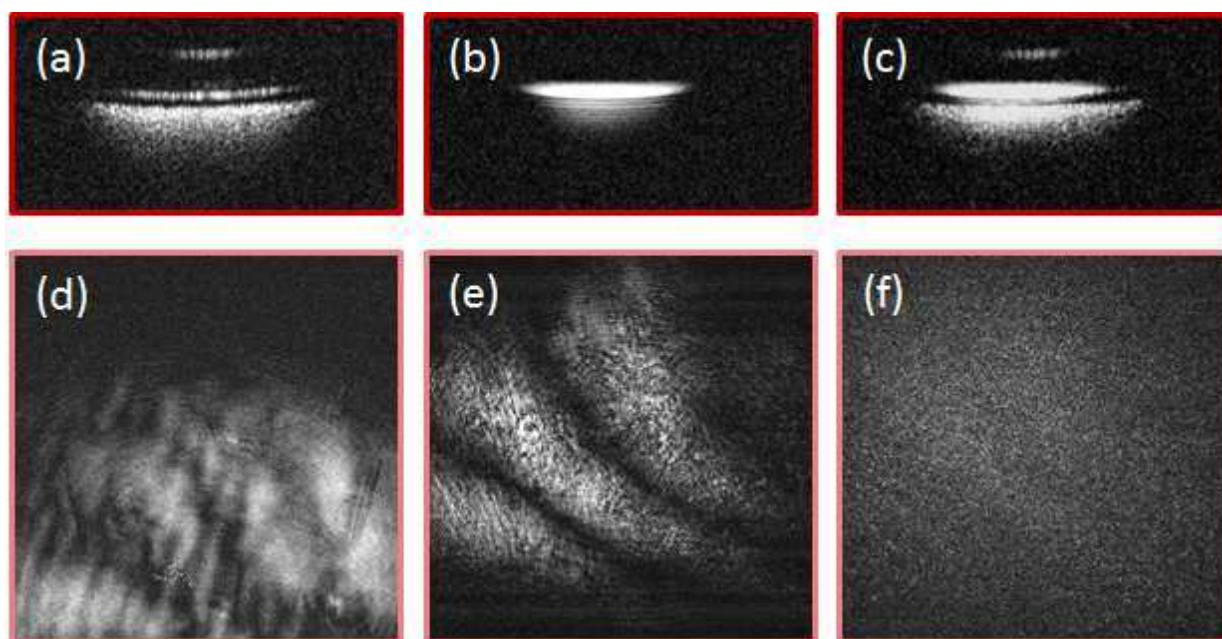


Figure 7.2 – Retinal imaging results with the combined system on artificial eye model [231]. (a-c) show the cross-sectional SDOCT images of artificial retinal layers (a), the FFOCT reference mirror (b) and the overlap of the FFOCT reference mirror image with an artificial retinal layer (c). (d-f) show the corresponding *en face* FFOCT images of the three different artificial retinal layers.

7.5 *In vivo* human retinal imaging

All the preliminary studies show that FFOCT is promising for high resolution *en face* retinal imaging and the combined system is able to overcome the difficulties for fast OPL matching for *in vivo* experiments, we finally applied our system for *in vivo* human retinal imaging. Informed consent was obtained for the subject and the experimental procedures adhered to the tenets of the Declaration of Helsinki.

7.5.1 FFOCT retinal imaging of the fovea

Experiment is first performed in the fovea area to image the IS/OS photoreceptor layer. The head of the subject is placed on a chin platform and pressed against a self-designed headrest. The SDOCT starts to do real-time line scanning of the retina. By looking into the scanning line of SDOCT as a fixation target, the imaging is done at the fovea area. The SDOCT image of the retinal fovea is showed in figure 7.3(a), which shows the IS/OS layer and RPE layer of the retina. By translating the system along the optical axis, the SDOCT image of IS/OS layer is overlapped with the SDOCT image of the FFOCT reference mirror (indicating as the red dashed line in figure 7.3(a)). In the meantime, the FFOCT imaging is launched and 40 FFOCT images are taken during a period of 200ms. The black box in the fundus photography (acquired with SPECTRALIS retinal imaging platform [235]) shown in figure 7.3(b) indicates the FFOCT imaging region with a green dashed line indicating the SDOCT scanning location. The acquired FFOCT images is processed by ImageJ with the plugin "Template matching" for lateral motion correction through cross correlation of the detected structural signals, and the stack is averaged to improve the image SNR. The final FFOCT image of the fovea is shown in figure 7.3(c) with zoomed in areas at about 1° eccentricity from the fovea (figure 7.3(d)) and the fovea center (figure 7.3(e)). Note that the subject has a pupil of 4.5mm during the experiment, no pupil dilation is applied and no AO correction is conducted. The theoretical resolution would be 4um, which is not enough to resolve all of the cone cells in the fovea center. Thus, the 2D power spectra got by Fourier transform (figure 7.3(f)) of the FFOCT image shows no Yellot's ring, the radius of which is proportional to the detected cone photoreceptor spacing [176, 236, 237]. Nevertheless, some cone cells with bigger signal are detectable and appears in the image, which offers the basis for the cross correlation to correct the lateral motion artefacts before averaging. The imaging location of this experiment is further confirmed by doing the fovea imaging around the photoreceptor layer with an AO-microscope (RTX1TM Adaptive Optics Retinal Camera, Imagine eyes [238]), and the images is shown in figure 7.3(g-j) for comparison. Note that even with AO, the AO retinal camera is also not able to resolve the cone photoreceptor at the fovea center as no Yellot's ring appears in the 2D power spectra (figure 7.3(j)).

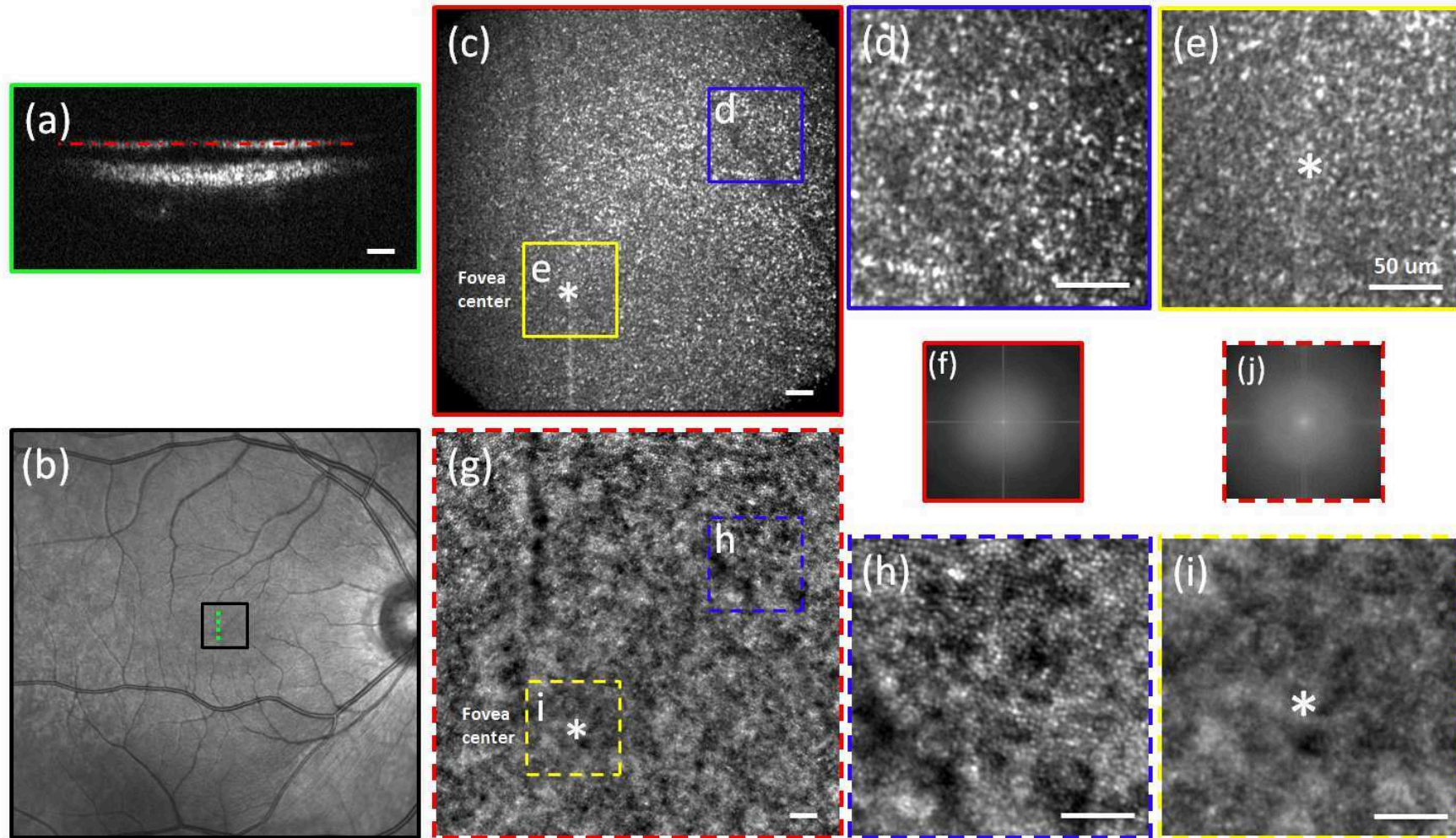


Figure 7.3 – In vivo human retinal imaging at the fovea. (a) The SDOCT cross-sectional image of the retinal fovea center with the red dashed line indicates the depth where FFOCT image is taken. (b) Fundus photography with the black box indicating the FFOCT imaging area and the green dashed line showing the SDOCT scanning position. (c) *In vivo* FFOCT image of the human retinal fovea without AO and the zoomed in areas at about 1° eccentricity from the fovea (d) and the fovea center (e). (f) The 2D power spectra of (c). (g-i) The AO-microscope image of the same fovea area as (c-e) for comparison. (j) The 2D power spectra of (g). Scale bar: $50\mu\text{m}$.

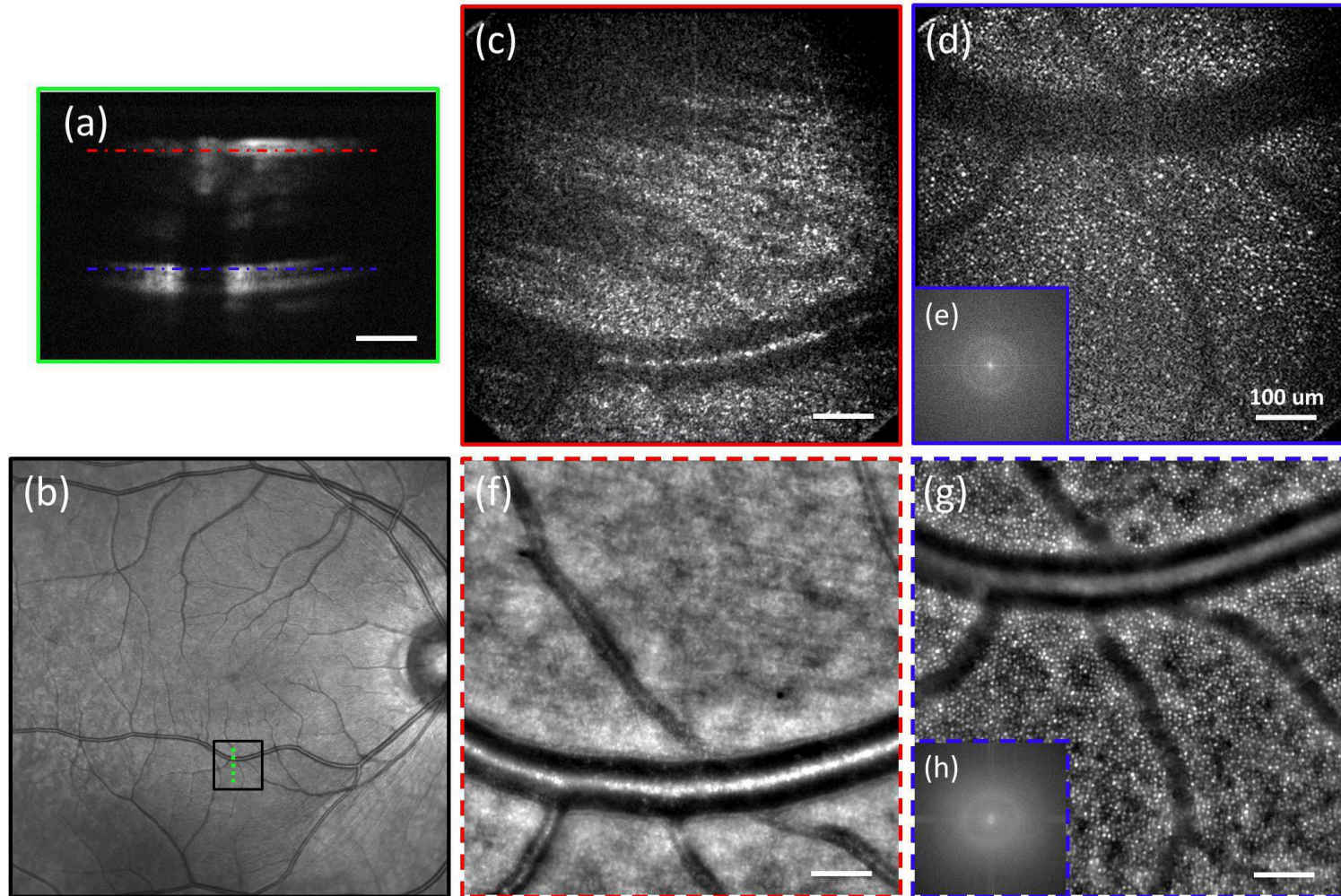


Figure 7.4 – *In vivo* human retinal imaging of retinal near periphery at 6° eccentricity down from the fovea center with a field of view of $2.4^\circ \times 2.4^\circ$. (a) The SDOCT cross-sectional image of the imaging position with the red (RNFL) and blue (IS/OS) dashed line indicating the FFOCT imaging depth. (b) Fundus photography with the black box indicating the the FFOCT imaging area and the green dashed line showing the SDOCT scanning position. (c-d) *In vivo* FFOCT image of the human retinal periphery at 6° eccentricity at the RNFL (c) and IS/OS photoreceptor layer (d) without AO. (e) The 2D power spectra of the (d) showing the Yellot's ring, indicating the cone photoreceptor spacing.(f-h) The AO-microscope image around the RNFL (f) and IS/OS photoreceptor layer (g) at the same retinal area and the 2D power spectra (h) of (g). Scale bar: $100\mu m$.

7.5.2 FFOCT retinal imaging of retinal near periphery

Experiment on *in vivo* human retinal imaging is further done to image the retinal near periphery. Here, by changing the position of the fixation target, retinal imaging is done at about 6° eccentricity down from the fovea center. Experimental results are shown in figure 7.4. Figure 7.4(a) shows the cross-sectional SDOCT image of the imaging area with the red (RNFL) and blue (IS/OS) dashed line indicating the overlapped positions with the FFOCT reference mirror image for *en face* FFOCT imaging. Here, two retinal layers are imaged with FFOCT sequentially (each with a stack of 40 images) by translating the system along the optical axis: the retinal nerve fibre layer (RNFL) and the IS/OS photoreceptor layer. Figure 7.4(b) shows the fundus photography again with the black box indicating the FFOCT imaging region and the green dashed line indicating the SDOCT scanning location. Figure 7.4(c) is the averaged FFOCT image of the RNFL, in which, the orientation of the nerve fibres are visible as well as a large blood vessel. Figure 7.4(d) is the FFOCT image of the IS/OS photoreceptor layer shows clearly the retinal cone photoreceptor mosaic as well as the shadows of the distribution of blood vessels. The images of the cone photoreceptors have an averaged size of about $5.5 - 6\mu\text{m}$ in diameter, corresponding to a real cone photoreceptor size of around $4\mu\text{m}$ in diameter with a FFOCT lateral resolution of $4\mu\text{m}$. The 2D power spectra of the FFOCT image of the IS/OS layer shows the Yellot's ring (figure 7.4(e)), which corresponding to the spatial frequency of the cone photoreceptor, meaning that we are resolving the cone photoreceptors in this FFOCT image. The circumferential-averaged power spectra give a maxima at 31.6cyc/degree , corresponds to a cone spacing of about $9.5\mu\text{m}$. This matches with the values given in references [176, 236] for cone spacing at around $6^\circ - 7^\circ$ eccentricity.

Again, retinal imaging by the AO-microscope is done around the same retinal layers at the same retinal area. The images are shown in figure 7.4(f,g). The 2D power spectra (figure 7.4(h)) shows the Yellot's ring with the circumferential-averaged power spectra give a maxima at 31.9cyc/degree , corresponds to a cone spacing of about $9.4\mu\text{m}$. This is close to what we have got with FFOCT image. The FFOCT RNFL image (figure 7.4(c)) shows obvious advantage compared with AO-microscope RNFL image (figure 7.4(f)) as the axial sectioning ability is poorer in the AO-microscope, making it difficult to select only specific retinal layers. Thus the small blood vessels, which supposed to be under the RNFL appears in the AO-microscope image. For the IS/OS photoreceptor layer image, FFOCT image SNR is lower compared with the AO-microscope image (figure 7.4(g)). This might due to the fact that we are not correcting the aberrations in the eye, which supposed to affects the signal level of FFOCT as explained in chapter 5. Also, the smaller axial sectioning offered by FFOCT selects the signal from a thinner retinal layer, which would give a relative lower signal.

Conclusions and perspectives

In this thesis, I have mainly discussed most of my work on a sub-project of ERC HELMHOLTZ that aims to apply FFOCT for high resolution human retinal examination. It starts from the evaluation of the effects of aberrations on FFOCT, followed by the development of a compact AO-FFOCT system, and finally ended by the application of FFOCT for the very first high resolution *in vivo en face* FFOCT human retinal imaging without AO. All these researches have proven that FFOCT could be a highly promising high resolution *in vivo en face* retinal imaging modality for clinical studies and medical diagnosis.

- I have first tried to quantify how FFOCT performances vary when aberration exists. It has been shown that, in FFOCT system, due to the use of a spatially incoherent illumination, the lateral resolution is almost insensitive to geometrical aberrations while only the signal level is reduced. This is demonstrated by theoretical analysis which compared FFOCT with traditional scanning OCTs and WFOCTs that use spatially coherent illuminations, followed by a numerical simulations with various basic Zernike polynomials applied to FFOCT. Experimental confirmations were conducted with nanoparticles as well as extended objects with defocus and random aberrations. More precisely, aberrations induce no obvious lateral resolution degradation with only the signal reduction proportional to the square root of the Strehl ratio. Let us consider the realistic case of a diffraction-limited imaging system with a PSF width of $2\mu\text{m}$ that allows for instance resolving the cones in retinal imaging. With a Strehl ratio of 0.1, which is considered to give a low quality image, the PSF would be broadened to about $6\mu\text{m}$ that would mask the cell structures. But in full-field OCT system, the same Strehl ratio would only reduce the signal by a factor of 3.1 while keeping the image sharpness.
- Secondly, A compact AO-FFOCT has been developed with an transmissive LCSLM as the wavefront corrector by adapting non-conjugate AO, meaning no strict plane conjugation between the wavefront corrector with the plane of aberration origin or pupil plane, for low order aberrations correction. A wavefront sensorless algorithm by using the FFOCT signal level as the correction metric has been applied, which further simplified the system. Our experiments on correcting a random aberration induced by LCSLM has shown that the corrected FFOCT image signal level with non-conjugate AO reaches $78.0\% \pm 2.2\%$ of the non-aberrated situation, which is slightly inferior but still acceptable compared

with a conjugate AO experiment which results in a corrected FFOCT image signal level reaching $84.3\% \pm 2.1\%$ of the non-aberrated image. The AO-FFOCT has been applied to sample-induced aberration correction of a ficus leaf and a fixed mouse brain tissue slice to improve the SNR of the FFOCT images when doing in-depth imaging. These experiments that simulate eye aberration correction in a simpler manner open the path to a straightforward implementation of AO-FFOCT for retinal imaging. AO-FFOCT retinal imaging has then been demonstrated in an artificial eye model showing signal improvement for all the detected retinal layers. Nevertheless, this experiment exposed the difficulties for the OPL matching for retinal imaging as the two arms of FFOCT has different optical geometries.

- At last, I have shown in this thesis the application of FFOCT for high resolution *in vivo* human retinal imaging. To solve the OPL matching difficulties, a commercial SDOCT system has been combined with our customized FFOCT to offer real-time OPL match through the cross-sectional SDOCT image. To resolve the eye motion problem during FFOCT image acquisition, a new fast CMOS camera working at a highest speed of $750Hz$ has been implemented. The feasibility has been validated with the artificial eye model. *In vivo en face* FFOCT human retinal imaging has been performed for the first time on an healthy eye without AO of both the RNFL and the IS/OS photoreceptor layer. The orientation of the retinal nerve fibres, the distribution of the retinal blood vessels as well as the cone photoreceptor mosaic are all detected in the high resolution FFOCT retinal images. No AO correction has been used in these experiments thanks to the resolution merit of FFOCT, and the better axial sectioning ability of FFOCT shows better retinal layer selection compared with AO-microscope used in the hospitals nowadays.

To successfully transform FFOCT to a clinical imaging modality for retinal examination, there are still several tasks ahead:

- The system we have now shows relatively low SNR for retinal imaging thus we were not able to image several other retinal layers that has lower reflectivity. This might due to the fact that we did not conduct aberration correction to improve the FFOCT signal level. As shown in chapter 7, an adaptive liquid lens is actually designed be installed in the FFOCT sample arm to correct the defocus and astigmatism, which would be help to improve the SNR. Then the dispersion would need to be compensated between all the arms of the combined system. The aberration of the eye to be imaged could be measured by an autorefractor to avoid the time needed for the AO process during the imaging process.
- Currently, the FFOCT system is not able to take 3D image stack for *in vivo* retinal imaging due to the eye motions. The axial eye movements would stop the FFOCT from doing precise depth scanning for each *en face* image. To resolve this issue, we suggest again to utilise the depth information that could be offered by the SDOCT cross-sectional image. By synchronize the data acquisition of SDOCT and FFOCT, for each FFOCT *en face* image, the depth information could be retraced through the overlapped location of SDOCT image of the FFOCT mirror with the SDOCT image of the cross-sectional

retinal layers. In this way, we might also be possible to take advantage of the axial eye motions to scanning across the full retina and reconstruct the FFOCT 3D image based on the depth information gained from SDOCT images.

- The *en face* FFOCT imaging of different retinal layers have been demonstrated on *ex vivo* retina tissue to characterize various retinal structures [239,240]. In the near future, more *in vivo* studies would also be indispensable to understand not only the histology of healthy retina but also the pathology of different retinal diseases to provide high sensitivity and specificity for future clinical diagnosis.
- Last but not least, our group is also working on applying FFOCT for *in vivo* human cornea imaging in a non-contact approach. From what we have acquired, FFOCT offers a comparable resolution as SLO while having a much larger imaging field. The system will also be combined with a SDOCT to do *in vivo* 3D imaging. Thus, in the future, we can expect an FFOCT system that could perform high resolution *in vivo en face* imaging on both human cornea and retina.

Peng Xiao, Viacheslav Mazlin, Mathis Fink, and A. Claude Boccara. "In vivo high resolution human retinal imaging with wavefront correctionless full-field OCT," *Optica*, (Under review)

Peng Xiao, Mathis Fink, and A. Claude Boccara. "Chapter 16: Incoherent illumination tomography and adaptive optics," *Wavefront shaping for biomedical imaging*, Cambridge University Press (In publishing)

Peng Xiao, Mathis Fink, and A. Claude Boccara. "Combining FF-OCT with SD-OCT for retinal imaging." *Optical Coherence Imaging Techniques and Imaging in Scattering Media II*. Vol. 10416. International Society for Optics and Photonics, (2017)

Peng Xiao, Mathis Fink, Amir H. Gandjbakhche, and A. Claude Boccara. "A resolution insensitive to geometrical aberrations by using incoherent illumination and interference imaging," *Eur. Phys. J. Spec. Top.* 226(7), 1603 (2017)

Peng Xiao, Mathias Fink, and A. Claude Boccara, "Retinal Imaging with Adaptive Optics Full-field OCT," *Proc. of SPIE Vol. 10053 (100530K-1)*, (2017)

Peng Xiao, Mathias Fink, and A. Claude Boccara, "A PSF width independent of aberrations in spatially incoherent interferometry," Paper 10073-37, *SPIE Photonic West 2017, USA*, (2017)

Olivier Touvenin, Kate Grieve, **Peng Xiao**, et al. "En face coherence microscopy [Invited]," *Biomedical Optics Express* 8(2), 622-639 (2017)

Peng Xiao, Mathis Fink, and A. Claude Boccara. "Adaptive optics full-field optical coherence tomography," *Journal of Biomedical Optics* 21(12), 121505 (2016)

Peng Xiao, Mathis Fink, and A. Claude Boccara. "Full-field spatially incoherent illumination interferometry: a spatial resolution almost insensitive to aberrations," *Optics Letters* 41(17), 3920-3923 (2016)

Peng Xiao, Mathias Fink, and A. Claude Boccara, "Adaptive Optics Full-field OCT: a Resolution Almost Insensitive to Aberrations," Paper 9697-33, *SPIE Photonic West 2016, USA*, (Feb. 2016)

Peng Xiao, Mathias Fink, and A. Claude Boccara, "An Optical Tomography PSF Almost Insensitive to Aberrations: the Benefit of a Spatial Incoherent Illumination," Paper 9717-17, *SPIE Photonic West 2016, USA*, (2016)

Peng Xiao, Mathias Fink, and A.Claude Boccaro, "Transmission Glass-Like Aberrations Correction for Full-Field OCT Imaging," Paper AOT3D.4, Imaging and Applied Optics 2015, OSA Technical Digest (online), USA, (2015)

Peng Xiao, Mathias Fink, and A.Claude Boccaro, "Pre-study of Retinal Imaging by Adaptive Optics Full-Field OCT with Transmissive Liquid Crystal Spatial Light Modulator," Paper 72197, Adaptive Optics and Wavefront Control in Microscopy and Ophthalmology, France, (2015)

References

- [1] David Huang, Eric A Swanson, Charles P Lin, Joel S Schuman, William G Stinson, Warren Chang, Michael R Hee, Thomas Flotte, Kenton Gregory, Carmen A Puliafito, et al. Optical coherence tomography. *Science (New York, NY)*, 254(5035):1178, 1991.
- [2] Joseph A Izatt, Stephen Boppart, Brett Bouma, Johannes de Boer, Wolfgang Drexler, Xingde Li, and Yoshiaki Yasuno. Introduction to the feature issue on the 25 year anniversary of optical coherence tomography. *Biomedical Optics Express*, 8(7):3289–3291, 2017.
- [3] E Beaurepaire, A Claude Boccara, M Lebec, L Blanchot, and H Saint-Jalmes. Full-field optical coherence microscopy. *Optics letters*, 23(4):244–246, 1998.
- [4] Laurent Vabre, Arnaud Dubois, and A Claude Boccara. Thermal-light full-field optical coherence tomography. *Optics letters*, 27(7):530–532, 2002.
- [5] Alfred Vogel and Vasani Venugopalan. Mechanisms of pulsed laser ablation of biological tissues. *Chemical reviews*, 103(2):577–644, 2003.
- [6] W Rudolph and M Kempe. Trends in optical biomedical imaging. *journal of modern optics*, 44(9):1617–1642, 1997.
- [7] BA Van Tiggelen. Green function retrieval and time reversal in a disordered world. *Physical review letters*, 91(24):243904, 2003.
- [8] Amaury Badon, Dayan Li, Geoffroy Lerosey, A Claude Boccara, Mathias Fink, and Alexandre Aubry. Smart optical coherence tomography for ultra-deep imaging through highly scattering media. *Science advances*, 2(11):e1600370, 2016.
- [9] Guy Indebetouw and Prapong Klysubun. Imaging through scattering media with depth resolution by use of low-coherence gating in spatiotemporal digital holography. *Optics Letters*, 25(4):212–214, 2000.
- [10] JB Pawley and Barry R Masters. Handbook of biological confocal microscopy. *Optical Engineering*, 35(9):2765–2766, 1996.
- [11] Adolf F Fercher. Optical coherence tomography. *Journal of Biomedical Optics*, 1(2):157–173, 1996.
- [12] Wolfgang Drexler and James G Fujimoto. Optical coherence tomography: Technology and applications, 2015.

- [13] Wayne R Hedrick, David L Hykes, and Dale E Starchman. Ultrasound physics and instrumentation. 2005.
- [14] Joel S Schuman, Carmen A Puliafito, James G Fujimoto, and Jay S Duker. *Optical coherence tomography of ocular diseases*. Slack Thorofare, NJ, 2004.
- [15] Carmen A Puliafito, Michael R Hee, Charles P Lin, Elias Reichel, Joel S Schuman, Jay S Duker, Joseph A Izatt, Eric A Swanson, and James G Fujimoto. Imaging of macular diseases with optical coherence tomography. *Ophthalmology*, 102(2):217–229, 1995.
- [16] Thomas J Wolfensberger and Michel Gonvers. Optical coherence tomography in the evaluation of incomplete visual acuity recovery after macula-off retinal detachments. *Graefe's archive for clinical and experimental ophthalmology*, 240(2):85–89, 2002.
- [17] Felipe A Medeiros, Linda M Zangwill, Christopher Bowd, Roberto M Vessani, Remo Sussanna, and Robert N Weinreb. Evaluation of retinal nerve fiber layer, optic nerve head, and macular thickness measurements for glaucoma detection using optical coherence tomography. *American journal of ophthalmology*, 139(1):44–55, 2005.
- [18] Pei-Lin Hsiung, Darshan R Phatak, Yu Chen, Aaron D Aguirre, James G Fujimoto, and James L Connolly. Benign and malignant lesions in the human breast depicted with ultrahigh resolution and three-dimensional optical coherence tomography 1. *Radiology*, 244(3):865–874, 2007.
- [19] Freddy T Nguyen, Adam M Zysk, Eric J Chaney, Jan G Kotynek, Uretz J Oliphant, Frank J Bellafiore, Kendrith M Rowland, Patricia A Johnson, and Stephen A Boppart. Intraoperative evaluation of breast tumor margins with optical coherence tomography. *Cancer research*, 69(22):8790–8796, 2009.
- [20] Chao Zhou, David W Cohen, Yihong Wang, Hsiang-Chieh Lee, Amy E Mondelblatt, Tsung-Han Tsai, Aaron D Aguirre, James G Fujimoto, and James L Connolly. Integrated optical coherence tomography and microscopy for ex vivo multiscale evaluation of human breast tissues. *Cancer research*, 70(24):10071–10079, 2010.
- [21] Julia Welzel, Eva Lankenau, Reginald Birngruber, and Ralf Engelhardt. Optical coherence tomography of the human skin. *Journal of the American Academy of Dermatology*, 37(6):958–963, 1997.
- [22] Cedric Blatter, Jessika Weingast, Aneesh Alex, Branislav Grajciar, Wolfgang Wieser, Wolfgang Drexler, Robert Huber, and Rainer A Leitgeb. In situ structural and microangiographic assessment of human skin lesions with high-speed oct. *Biomedical optics express*, 3(10):2636–2646, 2012.
- [23] Kevin G Phillips, Yun Wang, David Levitz, Niloy Choudhury, Emily Swanzey, James Lagowski, Molly Kulesz-Martin, and Steven L Jacques. Dermal reflectivity determined by optical coherence tomography is an indicator of epidermal hyperplasia and dermal edema within inflamed skin. *Journal of biomedical optics*, 16(4):040503–040503, 2011.
- [24] Hanan Morsy, Soren Kamp, Lars Thrane, Nille Behrendt, Birgit Saunder, Hisham Zayan, Ensaf Abd Elmagid, and Gregor BE Jemec. Optical coherence tomography imaging of psoriasis vulgaris: correlation with histology and disease severity. *Archives of dermatological research*, 302(2):105–111, 2010.

- [25] Mark C Pierce, John Strasswimmer, B Hyle Park, Barry Cense, and Johannes F de Boer. Advances in optical coherence tomography imaging for dermatology. *Journal of investigative dermatology*, 123(3):458–463, 2004.
- [26] Ki Hean Kim, Mark C Pierce, Gopi Maguluri, B Hyle Park, Sang June Yoon, Martha Lydon, Robert Sheridan, and Johannes F de Boer. In vivo imaging of human burn injuries with polarization-sensitive optical coherence tomography. *Journal of biomedical optics*, 17(6):066012–066012, 2012.
- [27] Bill W Colston, Ujwal S Sathyam, Luiz B DaSilva, Matthew J Everett, Pieter Stroeve, and LL Otis. Dental oct. *Optics express*, 3(6):230–238, 1998.
- [28] Toshihiko Yoshioka, Hitoshi Sakaue, Hitomi Ishimura, Arata Ebihara, Hideaki Suda, and Yasunori Sumi. Detection of root surface fractures with swept-source optical coherence tomography (ss-oct). *Photomedicine and laser surgery*, 31(1):23–27, 2013.
- [29] Guillermo J Tearney, Mark E Brezinski, Brett E Bouma, Stephen A Boppart, Costas Pitris, James F Southern, and James G Fujimoto. In vivo endoscopic optical biopsy with optical coherence tomography. *Science*, 276(5321):2037–2039, 1997.
- [30] Yingtian Pan, Huikai Xie, and Gary K Fedder. Endoscopic optical coherence tomography based on a microelectromechanical mirror. *Optics letters*, 26(24):1966–1968, 2001.
- [31] Patrick R Pfau, Michael V Sivak, Amitabh Chak, Margaret Kinnard, Richard CK Wong, Gerard A Isenberg, Joseph A Izatt, Andrew Rollins, and Volker Westphal. Criteria for the diagnosis of dysplasia by endoscopic optical coherence tomography. *Gastrointestinal endoscopy*, 58(2):196–202, 2003.
- [32] Joseph M Schmitt. Oct elastography: imaging microscopic deformation and strain of tissue. *Optics express*, 3(6):199–211, 1998.
- [33] Xing Liang, Marko Orescanin, Kathleen S Toohey, Michael F Insana, and Stephen A Boppart. Acoustomotive optical coherence elastography for measuring material mechanical properties. *Optics letters*, 34(19):2894–2896, 2009.
- [34] Steven G Adie, Brendan F Kennedy, Julian J Armstrong, Sergey A Alexandrov, and David D Sampson. Audio frequency in vivo optical coherence elastography. *Physics in medicine and biology*, 54(10):3129, 2009.
- [35] Chunhui Li, Zhihong Huang, and Ruikang K Wang. Elastic properties of soft tissue-mimicking phantoms assessed by combined use of laser ultrasonics and low coherence interferometry. *Optics express*, 19(11):10153–10163, 2011.
- [36] Thu-Mai Nguyen, Ali Zorgani, Maxime Lescanne, Claude Boccara, Mathias Fink, and Stefan Catheline. Diffuse shear wave imaging: toward passive elastography using low-frame rate spectral-domain optical coherence tomography. *Journal of Biomedical Optics*, 21(12):126013–126013, 2016.
- [37] Johannes F De Boer, Thomas E Milner, Martin JC van Gemert, and J Stuart Nelson. Two-dimensional birefringence imaging in biological tissue by polarization-sensitive optical coherence tomography. *Optics letters*, 22(12):934–936, 1997.
- [38] Mathieu G Ducros, Johannes F de Boer, Huai-En Huang, Lawrence C Chao, Zhongping Chen, J Stuart Nelson, Thomas E Milner, and H Grady Rylander. Polarization sensi-

- tive optical coherence tomography of the rabbit eye. *IEEE Journal of Selected Topics in Quantum Electronics*, 5(4):1159–1167, 1999.
- [39] Christoph K Hitzenberger, Erich Götzinger, Markus Sticker, Michael Pircher, and Adolf F Fercher. Measurement and imaging of birefringence and optic axis orientation by phase resolved polarization sensitive optical coherence tomography. *Optics Express*, 9(13):780–790, 2001.
- [40] Ruikang K Wang and Alfred L Nuttall. Phase-sensitive optical coherence tomography imaging of the tissue motion within the organ of corti at a subnanometer scale: a preliminary study. *Journal of biomedical optics*, 15(5):056005–056005, 2010.
- [41] Taner Akkin, Digant P Davé, Thomas E Milner, and H Grady Rylander III. Detection of neural activity using phase-sensitive optical low-coherence reflectometry. *Optics Express*, 12(11):2377–2386, 2004.
- [42] Emily J McDowell, Audrey K Ellerbee, Michael A Choma, Brian E Applegate, and Joseph A Izatt. Spectral domain phase microscopy for local measurements of cytoskeletal rheology in single cells. *Journal of biomedical optics*, 12(4):044008–044008, 2007.
- [43] Yali Jia, Ou Tan, Jason Tokayer, Benjamin Potsaid, Yimin Wang, Jonathan J Liu, Martin F Kraus, Hrebesh Subhash, James G Fujimoto, Joachim Hornegger, et al. Split-spectrum amplitude-decorrelation angiography with optical coherence tomography. *Optics express*, 20(4):4710–4725, 2012.
- [44] Yali Jia, Steven T Bailey, David J Wilson, Ou Tan, Michael L Klein, Christina J Flaxel, Benjamin Potsaid, Jonathan J Liu, Chen D Lu, Martin F Kraus, et al. Quantitative optical coherence tomography angiography of choroidal neovascularization in age-related macular degeneration. *Ophthalmology*, 121(7):1435–1444, 2014.
- [45] Richard F Spaide, James G Fujimoto, and Nadia K Waheed. Optical coherence tomography angiography. *Retina (Philadelphia, Pa.)*, 35(11):2161, 2015.
- [46] Zhongping Chen, Thomas E Milner, Digant Dave, and J Stuart Nelson. Optical doppler tomographic imaging of fluid flow velocity in highly scattering media. *Optics letters*, 22(1):64–66, 1997.
- [47] Joseph A Izatt, Manish D Kulkarni, Siavash Yazdanfar, Jennifer K Barton, and Ashley J Welch. In vivo bidirectional color doppler flow imaging of picoliter blood volumes using optical coherence tomography. *Optics letters*, 22(18):1439–1441, 1997.
- [48] Yimin Wang, Bradley A Bower, Joseph A Izatt, Ou Tan, and David Huang. In vivo total retinal blood flow measurement by fourier domain doppler optical coherence tomography. *Journal of biomedical optics*, 12(4):041215–041215, 2007.
- [49] Ruikang K Wang and Lin An. Doppler optical micro-angiography for volumetric imaging of vascular perfusion in vivo. *Optics express*, 17(11):8926–8940, 2009.
- [50] Shuo Tang, Tatiana B Krasieva, Zhongping Chen, and Bruce J Tromberg. Combined multiphoton microscopy and optical coherence tomography using a 12-fs broadband source. *Journal of biomedical optics*, 11(2):020502–020502, 2006.

- [51] E Beaurepaire, L Moreaux, F Amblard, and J Mertz. Combined scanning optical coherence and two-photon-excited fluorescence microscopy. *Optics Letters*, 24(14):969–971, 1999.
- [52] Shuai Yuan, Celeste A Roney, Jeremiah Wierwille, Chao-Wei Chen, Biying Xu, Gary Griffiths, James Jiang, Hongzhou Ma, Alex Cable, Ronald M Summers, et al. Co-registered optical coherence tomography and fluorescence molecular imaging for simultaneous morphological and molecular imaging. *Physics in medicine and biology*, 55(1):191, 2009.
- [53] Bosu Jeong, Byunghak Lee, Min Seong Jang, Hyoseok Nam, Sang June Yoon, Taejun Wang, Junsang Doh, Bo-Gie Yang, Myoung Ho Jang, and Ki Hean Kim. Combined two-photon microscopy and optical coherence tomography using individually optimized sources. *Optics express*, 19(14):13089–13096, 2011.
- [54] Jessica Barrick, Ana Doblaz, Michael R Gardner, Patrick R Sears, Lawrence E Ostrowski, and Amy L Oldenburg. High-speed and high-sensitivity parallel spectral-domain optical coherence tomography using a supercontinuum light source. *Optics Letters*, 41(24):5620–5623, 2016.
- [55] Aaron D Aguirre, Yu Chen, Bradley Bryan, Hiroshi Mashimo, Qin Huang, James L Connolly, and James G Fujimoto. Cellular resolution ex vivo imaging of gastrointestinal tissues with optical coherence microscopy. *Journal of biomedical optics*, 15(1):016025–016025, 2010.
- [56] Johannes F De Boer, Barry Cense, B Hyle Park, Mark C Pierce, Guillermo J Tearney, and Brett E Bouma. Improved signal-to-noise ratio in spectral-domain compared with time-domain optical coherence tomography. *Optics letters*, 28(21):2067–2069, 2003.
- [57] Michael A Choma, Marinko V Sarunic, Changhuei Yang, and Joseph A Izatt. Sensitivity advantage of swept source and fourier domain optical coherence tomography. *Optics express*, 11(18):2183–2189, 2003.
- [58] R Leitgeb, CK Hitzenberger, and Adolf F Fercher. Performance of fourier domain vs. time domain optical coherence tomography. *Optics express*, 11(8):889–894, 2003.
- [59] Nader Nassif, Barry Cense, B Hyle Park, Seok H Yun, Teresa C Chen, Brett E Bouma, Guillermo J Tearney, and Johannes F de Boer. In vivo human retinal imaging by ultrahigh-speed spectral domain optical coherence tomography. *Optics letters*, 29(5):480–482, 2004.
- [60] Maciej Wojtkowski, Vivek J Srinivasan, Tony H Ko, James G Fujimoto, Andrzej Kowalczyk, and Jay S Duker. Ultrahigh-resolution, high-speed, fourier domain optical coherence tomography and methods for dispersion compensation. *Optics express*, 12(11):2404–2422, 2004.
- [61] Barry Cense, Nader A Nassif, Teresa C Chen, Mark C Pierce, Seok-Hyun Yun, B Hyle Park, Brett E Bouma, Guillermo J Tearney, and Johannes F de Boer. Ultrahigh-resolution high-speed retinal imaging using spectral-domain optical coherence tomography. *Optics Express*, 12(11):2435–2447, 2004.
- [62] SR Chinn, EA Swanson, and JG Fujimoto. Optical coherence tomography using a frequency-tunable optical source. *Optics letters*, 22(5):340–342, 1997.

- [63] F Lexer, Christoph K Hitzenberger, AF Fercher, and M Kulhavy. Wavelength-tuning interferometry of intraocular distances. *Applied Optics*, 36(25):6548–6553, 1997.
- [64] Adrian Mariampillai, Beau A Standish, Eduardo H Moriyama, Mamta Khurana, Nigel R Munce, Michael KK Leung, James Jiang, Alex Cable, Brian C Wilson, I Alex Vitkin, et al. Speckle variance detection of microvasculature using swept-source optical coherence tomography. *Optics letters*, 33(13):1530–1532, 2008.
- [65] S Bourquin, P Seitz, and RP Salathé. Optical coherence topography based on a two-dimensional smart detector array. *Optics Letters*, 26(8):512–514, 2001.
- [66] A Knüttel, JM Schmitt, and JR Knutson. Low-coherence reflectometry for stationary lateral and depth profiling with acousto-optic deflectors and a ccd camera. *Optics Letters*, 19(4):302–304, 1994.
- [67] E Bordenave, E Abraham, G Jonusauskas, N Tsurumachi, J Oberle, C Rulliere, PE Minot, M Lassegues, and JE Surleve Bazeille. Wide-field optical coherence tomography: imaging of biological tissues. *Applied optics*, 41(10):2059–2064, 2002.
- [68] Markus Laubscher, Mathieu Ducros, Boris Karamata, Theo Lasser, and René Salathé. Video-rate three-dimensional optical coherence tomography. *Optics Express*, 10(9):429–435, 2002.
- [69] Yuuki Watanabe and Manabu Sato. Three-dimensional wide-field optical coherence tomography using an ultrahigh-speed cmos camera. *Optics Communications*, 281(7):1889–1895, 2008.
- [70] B Karamata, P Lambelet, M Laubscher, RP Salathé, and T Lasser. Spatially incoherent illumination as a mechanism for cross-talk suppression in wide-field optical coherence tomography. *Optics letters*, 29(7):736–738, 2004.
- [71] Boris Karamata, Patrick Lambelet, Markus Laubscher, Marcel Leutenegger, Stéphane Bourquin, and Theo Lasser. Multiple scattering in optical coherence tomography. i. investigation and modeling. *JOSA A*, 22(7):1369–1379, 2005.
- [72] Boris Karamata, Patrick Lambelet, Marcel Leutenegger, Markus Laubscher, Stéphane Bourquin, and Theo Lasser. Multiple scattering in optical coherence tomography. ii. experimental and theoretical investigation of cross talk in wide-field optical coherence tomography. *JOSA A*, 22(7):1380–1388, 2005.
- [73] Alfredo Dubra and Yusufu Sulai. Reflective afocal broadband adaptive optics scanning ophthalmoscope. *Biomedical optics express*, 2(6):1757–1768, 2011.
- [74] Zhuolin Liu, Omer P Kocaoglu, and Donald T Miller. In-the-plane design of an off-axis ophthalmic adaptive optics system using toroidal mirrors. *Biomedical optics express*, 4(12):3007–3030, 2013.
- [75] Sang-Hyuck Lee, John S Werner, and Robert J Zawadzki. Improved visualization of outer retinal morphology with aberration cancelling reflective optical design for adaptive optics-optical coherence tomography. *Biomedical optics express*, 4(11):2508–2517, 2013.
- [76] Robert J Noll. Zernike polynomials and atmospheric turbulence. *JOsA*, 66(3):207–211, 1976.

- [77] Guang-ming Dai. Modal compensation of atmospheric turbulence with the use of zernike polynomials and karhunen–loève functions. *JOSA A*, 12(10):2182–2193, 1995.
- [78] Junzhong Liang, Bernhard Grimm, Stefan Goelz, and Josef F Bille. Objective measurement of wave aberrations of the human eye with the use of a hartmann–shack wavefront sensor. *JOSA A*, 11(7):1949–1957, 1994.
- [79] Junzhong Liang and David R Williams. Aberrations and retinal image quality of the normal human eye. *JOSA A*, 14(11):2873–2883, 1997.
- [80] Zernike polynomials. http://www.telescope-optics.net/zernike_coefficients.htm.
- [81] Max Born and Emil Wolf. *Principles of optics: electromagnetic theory of propagation, interference and diffraction of light*. Elsevier, 1980.
- [82] Horace W Babcock. The possibility of compensating astronomical seeing. *Publications of the Astronomical Society of the Pacific*, 65(386):229–236, 1953.
- [83] F Rigaut, G Rousset, P Kern, JC Fontanella, JP Gaffard, F Merkle, and P Léna. Adaptive optics on a 3.6-m telescope-results and performance. *Astronomy and Astrophysics*, 250:280–290, 1991.
- [84] Claire Max. Lawrence Livermore National Laboratory and NSF Center for Adaptive Optics. http://www.ucolick.org/~max/History_AO_Max.htm.
- [85] Junzhong Liang, David R Williams, and Donald T Miller. Supernormal vision and high-resolution retinal imaging through adaptive optics. *JOSA A*, 14(11):2884–2892, 1997.
- [86] Austin Roorda, Fernando Romero-Borja, William J Donnelly III, Hope Queener, Thomas J Hebert, and Melanie CW Campbell. Adaptive optics scanning laser ophthalmoscopy. *Optics express*, 10(9):405–412, 2002.
- [87] Robert K Tyson. *Principles of adaptive optics*. CRC press, 2015.
- [88] Ronald P Grosso and Martin Yellin. The membrane mirror as an adaptive optical element. *JOSA*, 67(3):399–406, 1977.
- [89] Ehud Steinhaus and SG Lipson. Bimorph piezoelectric flexible mirror. *JOSA*, 69(3):478–481, 1979.
- [90] Anthony Fuschetto. Three-actuator deformable water-cooled mirror. In *Technical Symposium East*, pages 17–27. International Society for Optics and Photonics, 1979.
- [91] Donald T Miller, Larry N Thibos, and Xin Hong. Requirements for segmented correctors for diffraction-limited performance in the human eye. *Optics express*, 13(1):275–289, 2005.
- [92] D3128 spatial light modulator. Meadowlark Optics, <http://www.meadowlark.com>.
- [93] Bruno Berge and Jérôme Peseux. Variable focal lens controlled by an external voltage: An application of electrowetting. *The European Physical Journal E*, 3(2):159–163, 2000.
- [94] Chih-Cheng Cheng, C Alex Chang, and J Andrew Yeh. Variable focus dielectric liquid droplet lens. *Optics Express*, 14(9):4101–4106, 2006.
- [95] Weisong Wang and Ji Fang. Design, fabrication and testing of a micromachined integrated tunable microlens. *Journal of Micromechanics and Microengineering*, 16(7):1221, 2006.

- [96] Seok Woo Lee and Seung S Lee. Focal tunable liquid lens integrated with an electromagnetic actuator. *Applied physics letters*, 90(12):121129, 2007.
- [97] Arnaud Pouydebasque, Claudine Bridoux, Fabrice Jacquet, Stéphane Moreau, Eric Sage, Damien Saint-Patrice, Christophe Bouvier, Christophe Kopp, Gilles Marchand, Sébastien Bolis, et al. Varifocal liquid lenses with integrated actuator, high focusing power and low operating voltage fabricated on 200mm wafers. *Sensors and actuators A: physical*, 172(1):280–286, 2011.
- [98] Hiromasa Oku and Masatoshi Ishikawa. High-speed liquid lens with 2 ms response and 80.3 nm root-mean-square wavefront error. *Applied Physics Letters*, 94(22):221108, 2009.
- [99] Adaptive liquid lens. Varioptic, <http://www.varioptic.com>.
- [100] Francois Roddier. Curvature sensing and compensation: a new concept in adaptive optics. *Applied Optics*, 27(7):1223–1225, 1988.
- [101] Francois J Roddier, J Elon Graves, and Eric J Limburg. Seeing monitor based on wavefront curvature sensing. In *Astronomy'90, Tucson AZ, 11-16 Feb 90*, pages 474–479. International Society for Optics and Photonics, 1990.
- [102] R Ragazzoni and D Bonaccini. The adaptive optics system for the telescopio nazionale galileo. In *European Southern Observatory Conference and Workshop Proceedings*, volume 54, page 17, 1996.
- [103] Donald W Phillion and Kevin Baker. Two-sided pyramid wavefront sensor in the direct phase mode. In *SPIE Astronomical Telescopes+ Instrumentation*, pages 627228–627228. International Society for Optics and Photonics, 2006.
- [104] Markus Rueckel, Julia A Mack-Bucher, and Winfried Denk. Adaptive wavefront correction in two-photon microscopy using coherence-gated wavefront sensing. *Proceedings of the National Academy of Sciences*, 103(46):17137–17142, 2006.
- [105] Wavefront Sensing. Coherence-gated wavefront sensing. *Adaptive Optics for Biological Imaging*, page 253, 2013.
- [106] Ben C Platt and Roland Shack. History and principles of shack-hartmann wavefront sensing. *Journal of Refractive Surgery*, 17(5):S573–S577, 2001.
- [107] Sandrine Thomas. Optimized centroid computing in a shack-hartmann. *Cerro Tololo Inter-American Observatories, Casilla*, 603.
- [108] Ronald Cubalchini. Modal wave-front estimation from phase derivative measurements. *JOSA*, 69(7):972–977, 1979.
- [109] Yifan Jian. Adaptive optics optical coherence tomography for in vivo retinal imaging. *PhD these, Simon fraser university*, 2014.
- [110] PN Marsh, D Burns, and JM Girkin. Practical implementation of adaptive optics in multiphoton microscopy. *Optics Express*, 11(10):1123–1130, 2003.
- [111] L Sherman, JY Ye, O Albert, and TB Norris. Adaptive correction of depth-induced aberrations in multiphoton scanning microscopy using a deformable mirror. *Journal of microscopy*, 206(1):65–71, 2002.

- [112] Kayvan F Tehrani, Jianquan Xu, Yiwen Zhang, Ping Shen, and Peter Kner. Adaptive optics stochastic optical reconstruction microscopy (ao-storm) using a genetic algorithm. *Optics express*, 23(10):13677–13692, 2015.
- [113] JR Fienup and JJ Miller. Aberration correction by maximizing generalized sharpness metrics. *JOSA A*, 20(4):609–620, 2003.
- [114] Delphine Débarre, Edward J Botcherby, Tomoko Watanabe, Shankar Srinivas, Martin J Booth, and Tony Wilson. Image-based adaptive optics for two-photon microscopy. *Optics letters*, 34(16):2495–2497, 2009.
- [115] Martin J Booth, Mark AA Neil, and Tony Wilson. New modal wave-front sensor: application to adaptive confocal fluorescence microscopy and two-photon excitation fluorescence microscopy. *JOSA A*, 19(10):2112–2120, 2002.
- [116] Martin J Booth. Wave front sensor-less adaptive optics: a model-based approach using sphere packings. *Optics express*, 14(4):1339–1352, 2006.
- [117] S Bonora and RJ Zawadzki. Wavefront sensorless modal deformable mirror correction in adaptive optics: optical coherence tomography. *Optics letters*, 38(22):4801–4804, 2013.
- [118] Delphine Débarre, Martin J Booth, and Tony Wilson. Image based adaptive optics through optimisation of low spatial frequencies. *Optics Express*, 15(13):8176–8190, 2007.
- [119] Norio Baba, Kazuhiro Terayama, Toshihiro Yoshimizu, Norihiko Ichise, and Nobuo Tanaka. An auto-tuning method for focusing and astigmatism correction in haadfstem, based on the image contrast transfer function. *Journal of Electron Microscopy*, 50(3):163–176, 2001.
- [120] Bridget M Hanser, Mats GL Gustafsson, DA Agard, and John W Sedat. Phase-retrieved pupil functions in wide-field fluorescence microscopy. *Journal of microscopy*, 216(1):32–48, 2004.
- [121] Robert A Gonsalves. Phase retrieval and diversity in adaptive optics. *Optical Engineering*, 21(5):829–832, 1982.
- [122] Richard G Paxman, Timothy J Schulz, and James R Fienup. Joint estimation of object and aberrations by using phase diversity. *JOSA A*, 9(7):1072–1085, 1992.
- [123] Na Ji, Daniel E Milkie, and Eric Betzig. Adaptive optics via pupil segmentation for high-resolution imaging in biological tissues. *Nature methods*, 7(2):141–147, 2010.
- [124] Daniel E Milkie, Eric Betzig, and Na Ji. Pupil-segmentation-based adaptive optical microscopy with full-pupil illumination. *Optics letters*, 36(21):4206–4208, 2011.
- [125] Rui Liu, Daniel E Milkie, Aaron Kerlin, Bryan MacLennan, and Na Ji. Direct phase measurement in zonal wavefront reconstruction using multidither coherent optical adaptive technique. *Optics express*, 22(2):1619–1628, 2014.
- [126] Steven G Adie, Benedikt W Graf, Adeel Ahmad, P Scott Carney, and Stephen A Boppart. Computational adaptive optics for broadband optical interferometric tomography of biological tissue. *Proceedings of the National Academy of Sciences*, 109(19):7175–7180, 2012.

- [127] Abhishek Kumar, Wolfgang Drexler, and Rainer A Leitgeb. Subaperture correlation based digital adaptive optics for full field optical coherence tomography. *Optics express*, 21(9):10850–10866, 2013.
- [128] Steven G Adie, Nathan D Shemonski, Benedikt W Graf, Adeel Ahmad, P Scott Carney, and Stephen A Boppart. Guide-star-based computational adaptive optics for broadband interferometric tomography. *Applied physics letters*, 101(22):221117, 2012.
- [129] Nathan D Shemonski, Fredrick A South, Yuan-Zhi Liu, Steven G Adie, P Scott Carney, and Stephen A Boppart. Computational high-resolution optical imaging of the living human retina. *Nature photonics*, 9(7):440–443, 2015.
- [130] Dierck Hillmann, Hendrik Spahr, Carola Hain, Helge Sudkamp, Gesa Franke, Clara Pfäffle, Christian Winter, and Gereon Hüttmann. Aberration-free volumetric high-speed imaging of in vivo retina. *Scientific reports*, 6:35209, 2016.
- [131] Abhishek Kumar, Lara M Wurster, Matthias Salas, Laurin Ginner, Wolfgang Drexler, and Rainer A Leitgeb. In-vivo digital wavefront sensing using swept source oct. *Biomedical Optics Express*, 8(7):3369–3382, 2017.
- [132] Paul L Kaufman, Francis Heed Adler, Leonard A Levin, and Albert Alm. *Adler’s Physiology of the Eye*. Elsevier Health Sciences, 2011.
- [133] Pablo Artal. Optics of the eye and its impact in vision: a tutorial. *Advances in Optics and Photonics*, 6(3):340–367, 2014.
- [134] FW Campbell and RW Gubisch. Optical quality of the human eye. *The Journal of Physiology*, 186(3):558–578, 1966.
- [135] Glyn Walsh, HC Howland, and WN Charman. Objective technique for the determination of monochromatic aberrations of the human eye. *JOSA A*, 1(9):987–992, 1984.
- [136] William J Donnelly and Austin Roorda. Optimal pupil size in the human eye for axial resolution. *JOSA A*, 20(11):2010–2015, 2003.
- [137] A Roorda, CA Garcia, JA Martin, S Poonja, H Queener, F Romero-Borja, R Sepulveda, K Venkateswaran, and Y Zhang. What can adaptive optics do for a scanning laser ophthalmoscope? *BULLETIN-SOCIETE BELGE D OPHTALMOLOGIE*, 302:231, 2006.
- [138] Jason Porter, Antonio Guirao, Ian G Cox, and David R Williams. Monochromatic aberrations of the human eye in a large population. *JOSA A*, 18(8):1793–1803, 2001.
- [139] José Francisco Castejón-Mochón, Norberto López-Gil, Antonio Benito, and Pablo Artal. Ocular wave-front aberration statistics in a normal young population. *Vision Research*, 42(13):1611–1617, 2002.
- [140] Xin Hong, Larry Thibos, Arthur Bradley, Donald Miller, Xu Cheng, and Nikole Himebaugh. Statistics of aberrations among healthy young eyes. In *Vision Science and its Applications*, page SuA5. Optical Society of America, 2001.
- [141] Jessica Jarosz, Pedro Mécê, Jean-Marc Conan, Cyril Petit, Michel Paques, and Serge Meimon. High temporal resolution aberrometry in a 50-eye population and implications for adaptive optics error budget. *Biomedical Optics Express*, 8(4):2088–2105, 2017.

- [142] WN Charman and G Heron. Fluctuations in accommodation: a review. *Ophthalmic and Physiological Optics*, 8(2):153–164, 1988.
- [143] Heidi Hofer, Pablo Artal, Ben Singer, Juan Luis Aragón, and David R Williams. Dynamics of the eye’s wave aberration. *JOSA A*, 18(3):497–506, 2001.
- [144] Luis Diaz-Santana, Cristiano Torti, Ian Munro, Paul Gasson, and Chris Dainty. Benefit of higher closed-loop bandwidths in ocular adaptive optics. *Optics express*, 11(20):2597–2605, 2003.
- [145] Lorrin A Riggs, John C Armington, and Floyd Ratliff. Motions of the retinal image during fixation. *JOSA*, 44(4):315–321, 1954.
- [146] M Ezenman, PE Hallett, and RC Frecker. Power spectra for ocular drift and tremor. *Vision research*, 25(11):1635–1640, 1985.
- [147] Roy de Kinkelder, Jeroen Kalkman, Dirk J Faber, Olaf Schraa, Pauline HB Kok, Frank D Verbraak, and Ton G van Leeuwen. Heartbeat-induced axial motion artifacts in optical coherence tomography measurements of the retina. *Investigative ophthalmology & visual science*, 52(6):3908–3913, 2011.
- [148] David Lafaille. *Optical Coherence Tomography and Adaptive Optics. Study of a prototype applicable to ophthalmology*. Theses, Université Paris-Diderot - Paris VII, July 2005.
- [149] Donald T Miller, David R Williams, G Michael Morris, and Junzhong Liang. Images of cone photoreceptors in the living human eye. *Vision research*, 36(8):1067–1079, 1996.
- [150] Austin Roorda and David R Williams. The arrangement of the three cone classes in the living human eye. *Nature*, 397(6719):520, 1999.
- [151] M Glanc, E Gendron, F Lacombe, D Lafaille, J-F Le Gargasson, and P Léna. Towards wide-field retinal imaging with adaptive optics. *Optics Communications*, 230(4):225–238, 2004.
- [152] Stacey S Choi, Nathan Doble, Joseph L Hardy, Steven M Jones, John L Keltner, Scot S Olivier, and John S Werner. In vivo imaging of the photoreceptor mosaic in retinal dystrophies and correlations with visual function. *Investigative ophthalmology & visual science*, 47(5):2080–2092, 2006.
- [153] Yoshiyuki Kitaguchi, Kenichiro Bessho, Tatsuo Yamaguchi, Naoki Nakazawa, Toshifumi Mihashi, and Takashi Fujikado. In vivo measurements of cone photoreceptor spacing in myopic eyes from images obtained by an adaptive optics fundus camera. *Japanese journal of ophthalmology*, 51(6):456–461, 2007.
- [154] Normal fundus photograph. https://en.wikipedia.org/wiki/Fundus_photography.
- [155] Fundus photograph with glaucoma. <https://drsinashool.files.wordpress.com/2011/12/21.jpg>.
- [156] Fundus photograph with diabetic retinopathy. http://www.gogieyeclinic.com/diabetic_retinopathy.html.
- [157] Robert H Webb, George W Hughes, and Francois C Delori. Confocal scanning laser ophthalmoscope. *Applied optics*, 26(8):1492–1499, 1987.

- [158] R Daniel Ferguson, Zhangyi Zhong, Daniel X Hammer, Mircea Mujat, Ankit H Patel, Cong Deng, Weiyao Zou, and Stephen A Burns. Adaptive optics scanning laser ophthalmoscope with integrated wide-field retinal imaging and tracking. *JOSA A*, 27(11):A265–A277, 2010.
- [159] Alfredo Dubra, Yusufu Sulai, Jennifer L Norris, Robert F Cooper, Adam M Dubis, David R Williams, and Joseph Carroll. Noninvasive imaging of the human rod photoreceptor mosaic using a confocal adaptive optics scanning ophthalmoscope. *Biomedical optics express*, 2(7):1864–1876, 2011.
- [160] EM Wells-Gray, SS Choi, A Bries, and N Doble. Variation in rod and cone density from the fovea to the mid-periphery in healthy human retinas using adaptive optics scanning laser ophthalmoscopy. *Eye*, 30(8):1135–1143, 2016.
- [161] Austin Roorda, Yuhua Zhang, and Jacque L Duncan. High-resolution in vivo imaging of the rpe mosaic in eyes with retinal disease. *Investigative Ophthalmology & Visual Science*, 48(5):2297–2303, 2007.
- [162] Maciej Wojtkowski, Vivek Srinivasan, James G Fujimoto, Tony Ko, Joel S Schuman, Andrzej Kowalczyk, and Jay S Duker. Three-dimensional retinal imaging with high-speed ultrahigh-resolution optical coherence tomography. *Ophthalmology*, 112(10):1734–1746, 2005.
- [163] Wolfgang Drexler, U Morgner, FX Kärtner, C Pitris, SA Boppart, XD Li, EP Ippen, and JG Fujimoto. In vivo ultrahigh-resolution optical coherence tomography. *Optics letters*, 24(17):1221–1223, 1999.
- [164] Wolfgang Drexler, Uwe Morgner, Ravi K Ghanta, Franz X Kärtner, Joel S Schuman, and James G Fujimoto. Ultrahigh-resolution ophthalmic optical coherence tomography. *Nature medicine*, 7(4):502, 2001.
- [165] Wolfgang Drexler. Ultrahigh-resolution optical coherence tomography. *Journal of biomedical optics*, 9(1):47–74, 2004.
- [166] Gadi Wollstein, Leila A Paunescu, Tony H Ko, James G Fujimoto, Andrew Kowalevicz, Ingmar Hartl, Siobahn Beaton, Hiroshi Ishikawa, Cynthia Mattox, Omah Singh, et al. Ultrahigh-resolution optical coherence tomography in glaucoma. *Ophthalmology*, 112(2):229–237, 2005.
- [167] Tony H Ko, James G Fujimoto, Jay S Duker, Lelia A Paunescu, Wolfgang Drexler, Caroline R Baumal, Carmen A Puliafito, Elias Reichel, Adam H Rogers, and Joel S Schuman. Comparison of ultrahigh-and standard-resolution optical coherence tomography for imaging macular hole pathology and repair. *Ophthalmology*, 111(11):2033–2043, 2004.
- [168] Tony H Ko, James G Fujimoto, Joel S Schuman, Lelia A Paunescu, Andrew M Kowalevicz, Ingmar Hartl, Wolfgang Drexler, Gadi Wollstein, Hiroshi Ishikawa, and Jay S Duker. Comparison of ultrahigh-and standard-resolution optical coherence tomography for imaging macular pathology. *Ophthalmology*, 112(11):1922–e1, 2005.
- [169] DT Miller, OP Kocaoglu, Q Wang, and S Lee. Adaptive optics and the eye (super resolution oct). *Eye*, 25(3):321, 2011.

- [170] Kevin SK Wong, Yifan Jian, Michelle Cua, Stefano Bonora, Robert J Zawadzki, and Marinko V Sarunic. In vivo imaging of human photoreceptor mosaic with wavefront sensorless adaptive optics optical coherence tomography. *Biomedical optics express*, 6(2):580–590, 2015.
- [171] Robert J Zawadzki, Barry Cense, Yan Zhang, Stacey S Choi, Donald T Miller, and John S Werner. Ultrahigh-resolution optical coherence tomography with monochromatic and chromatic aberration correction. *Optics express*, 16(11):8126–8143, 2008.
- [172] Donald T Miller, Junle Qu, Ravi S Jonnal, Karan Thorn, et al. Coherence gating and adaptive optics in the eye. In *Proc. SPIE*, volume 4956, pages 65–72, 2003.
- [173] B Hermann, EJ Fernández, A Unterhuber, H Sattmann, AF Fercher, W Drexler, PM Prieto, and P Artal. Adaptive-optics ultrahigh-resolution optical coherence tomography. *Optics letters*, 29(18):2142–2144, 2004.
- [174] Yan Zhang, Jungtae Rha, Ravi S Jonnal, and Donald T Miller. Adaptive optics parallel spectral domain optical coherence tomography for imaging the living retina. *Optics Express*, 13(12):4792–4811, 2005.
- [175] Robert J Zawadzki, Steven M Jones, Scot S Olivier, Mingtao Zhao, Bradley A Bower, Joseph A Izatt, Stacey Choi, Sophie Laut, and John S Werner. Adaptive-optics optical coherence tomography for high-resolution and high-speed 3d retinal in vivo imaging. *Optics express*, 13(21):8532–8546, 2005.
- [176] Zhuolin Liu, Omer P Kocaoglu, and Donald T Miller. 3d imaging of retinal pigment epithelial cells in the living human retina. *Investigative ophthalmology & visual science*, 57(9):OCT533–OCT543, 2016.
- [177] Arnaud Dubois, Kate Grieve, Gael Moneron, Romain Lecaque, Laurent Vabre, and Claude Boccara. Ultrahigh-resolution full-field optical coherence tomography. *Applied optics*, 43(14):2874–2883, 2004.
- [178] Olivier Thouvenin, Mathias Fink, and Claude Boccara. Dynamic multimodal full-field optical coherence tomography and fluorescence structured illumination microscopy. *Journal of Biomedical Optics*, 22(2):026004–026004, 2017.
- [179] Arnaud Dubois, Gael Moneron, and Claude Boccara. Thermal-light full-field optical coherence tomography in the 1.2 μm wavelength region. *Optics Communications*, 266(2):738–743, 2006.
- [180] WY Oh, BE Bouma, N Iftimia, SH Yun, R Yelin, and GJ Tearney. Ultrahigh-resolution full-field optical coherence microscopy using ingaas camera. *Optics express*, 14(2):726–735, 2006.
- [181] S Labiau, G David, S Gigan, and AC Boccara. Defocus test and defocus correction in full-field optical coherence tomography. *Optics letters*, 34(10):1576–1578, 2009.
- [182] Arnaud Dubois. *Handbook of full-field optical coherence microscopy: technology and applications*. Pan Stanford Publishing, 2016.
- [183] Olivier Thouvenin. *Optical 3D imaging of subcellular dynamics in biological cultures and tissues: Applications to ophthalmology and neuroscience*. Theses, Université Paris-Diderot - Paris VII, July 2017.

- [184] Egidijus Auksorius and A Claude Boccara. Dark-field full-field optical coherence tomography. *Optics letters*, 40(14):3272–3275, 2015.
- [185] Olivier Thouvenin, Kate Grieve, Peng Xiao, Clement Apelian, and A Claude Boccara. En face coherence microscopy. *Biomedical optics express*, 8(2):622–639, 2017.
- [186] Llttech lightct scanner. <http://www.lltechimaging.com/>.
- [187] Osnath Assayag, Kate Grieve, Bertrand Devaux, Fabrice Harms, Johan Pallud, Fabrice Chretien, Claude Boccara, and Pascale Varlet. Imaging of non-tumorous and tumorous human brain tissues with full-field optical coherence tomography. *NeuroImage: Clinical*, 2:549–557, 2013.
- [188] Manu Jain, Nidhi Shukla, Maryem Manzoor, Sylvie Nadolny, and Sushmita Mukherjee. Modified full-field optical coherence tomography: A novel tool for rapid histology of tissues. *Journal of pathology informatics*, 2, 2011.
- [189] Kate Grieve, Karima Mouslim, Osnath Assayag, Eugénie Dalimier, Fabrice Harms, Alexis Bruhat, Claude Boccara, and Martine Antoine. Assessment of sentinel node biopsies with full-field optical coherence tomography. *Technology in cancer research & treatment*, 15(2):266–274, 2016.
- [190] Manu Jain, Brian D Robinson, Bekheit Salamoon, Olivier Thouvenin, Claude Boccara, and Sushmita Mukherjee. Rapid evaluation of fresh ex vivo kidney tissue with full-field optical coherence tomography. *Journal of pathology informatics*, 6, 2015.
- [191] Osnath Assayag, Martine Antoine, Brigitte Sigal-Zafrani, Michael Riben, Fabrice Harms, Adriano Burcheri, Kate Grieve, Eugénie Dalimier, Bertrand Le Conte de Poly, and Claude Boccara. Large field, high resolution full-field optical coherence tomography: a pre-clinical study of human breast tissue and cancer assessment. *Technology in cancer research & treatment*, 13(5):455–468, 2014.
- [192] Inge TA Peters, Paulien L Stegehuis, Ronald Peek, Florine L Boer, Erik W van Zwet, Jeroen Eggermont, Johan R Westphal, Peter JK Kuppen, J Baptist Trimbos, Carina GJM Hilders, et al. Noninvasive detection of metastases and follicle density in ovarian tissue using full-field optical coherence tomography. *Clinical Cancer Research*, 22(22):5506–5513, 2016.
- [193] Clement Apelian, Fabrice Harms, Olivier Thouvenin, and A Claude Boccara. Dynamic full field optical coherence tomography: subcellular metabolic contrast revealed in tissues by interferometric signals temporal analysis. *Biomedical optics express*, 7(4):1511–1524, 2016.
- [194] Jonas Binding, Juliette Ben Arous, Jean-François Léger, Sylvain Gigan, Claude Boccara, and Laurent Bourdieu. Brain refractive index measured in vivo with high-na defocus-corrected full-field oct and consequences for two-photon microscopy. *Optics express*, 19(6):4833–4847, 2011.
- [195] Amir Nahas, Morgane Bauer, Stéphane Roux, and A Claude Boccara. 3d static elastography at the micrometer scale using full field oct. *Biomedical optics express*, 4(10):2138–2149, 2013.
- [196] Aitana Perea-Gomez, Anne Camus, Anne Moreau, Kate Grieve, Gael Moneron, Arnaud Dubois, Christian Cibert, and Jérôme Collignon. Initiation of gastrulation in the

- mouse embryo is preceded by an apparent shift in the orientation of the anterior-posterior axis. *Current Biology*, 14(3):197–207, 2004.
- [197] Jing-gao Zheng, Danyu Lu, Tianyuan Chen, Chengming Wang, Ning Tian, Fengying Zhao, Tiancheng Huo, Ning Zhang, Dieyan Chen, Wanyun Ma, et al. Label-free sub-cellular 3d live imaging of preimplantation mouse embryos with full-field optical coherence tomography. *Journal of biomedical optics*, 17(7):0705031–0705033, 2012.
- [198] Karin Wiesauer, Michael Pircher, Erich Götzinger, Siegfried Bauer, Rainer Engelke, Gisela Ahrens, Gabi Grützner, Christoph K Hitzenberger, and David Stifter. En-face scanning optical coherence tomography with ultra-high resolution for material investigation. *Optics Express*, 13(3):1015–1024, 2005.
- [199] Egidijus Auksorius and A Claude Boccara. Fingerprint imaging from the inside of a finger with full-field optical coherence tomography. *Biomedical optics express*, 6(11):4465–4471, 2015.
- [200] Olivier Thouvenin, Clement Apelian, Amir Nahas, Mathias Fink, and Claude Boccara. Full-field optical coherence tomography as a diagnosis tool: Recent progress with multimodal imaging. *Applied Sciences*, 7(3):236, 2017.
- [201] Clinical atlas lltech. <http://www.lltechimaging.com/image-gallery/atlas-of-images/>.
- [202] Egidijus Auksorius, Yaron Bromberg, Rūta Motiejūnaitė, Alberto Pieretti, Linbo Liu, Emmanuel Coron, Jorge Aranda, Allan M Goldstein, Brett E Bouma, Andrius Kazlauskas, et al. Dual-modality fluorescence and full-field optical coherence microscopy for biomedical imaging applications. *Biomedical optics express*, 3(3):661–666, 2012.
- [203] Amir Nahas, Mariana Varna, Emmanuel Fort, and A Claude Boccara. Detection of plasmonic nanoparticles with full field-oct: optical and photothermal detection. *Biomedical optics express*, 5(10):3541–3546, 2014.
- [204] Gael Moneron, Albert-Claude Boccara, and Arnaud Dubois. Polarization-sensitive full-field optical coherence tomography. *Optics letters*, 32(14):2058–2060, 2007.
- [205] Lingfeng Yu and MK Kim. Full-color three-dimensional microscopy by wide-field optical coherence tomography. *Optics express*, 12(26):6632–6641, 2004.
- [206] Arnaud Dubois, Julien Moreau, and Claude Boccara. Spectroscopic ultrahigh-resolution full-field optical coherence microscopy. *Optics express*, 16(21):17082–17091, 2008.
- [207] Anke Bossen, Roland Lehmann, and Christoph Meier. Internal fingerprint identification with optical coherence tomography. *IEEE photonics technology letters*, 22(7):507–509, 2010.
- [208] Max Born and Emil Wolf. *Principles of optics: electromagnetic theory of propagation, interference and diffraction of light*. Elsevier, 2013.
- [209] Joseph W Goodman. *Introduction to Fourier optics*. Roberts and Company Publishers, 2005.
- [210] Peng Xiao, Mathias Fink, and A Claude Boccara. Full-field spatially incoherent illumination interferometry: a spatial resolution almost insensitive to aberrations. *Optics letters*, 41(17):3920–3923, 2016.

- [211] Michelson interferometer. <https://skullsinthestars.files.wordpress.com/2008/09/michelson.jpg>.
- [212] Young's two-pinhole interferometer. <https://skullsinthestars.files.wordpress.com/2010/06/youngsschematicddetail2.jpg>.
- [213] Pieter Hendrik van CITTERT. Die wahrscheinliche schwingungsverteilung in einer von einer lichtquelle direkt oder mittels einer linse beleuchteten ebene. *Physica*, 1(1-6):201–210, 1934.
- [214] Frits Zernike. The concept of degree of coherence and its application to optical problems. *Physica*, 5(8):785–795, 1938.
- [215] Peng Xiao, Mathias Fink, Amir H Gandjbakhche, and A Claude Boccara. A resolution insensitive to geometrical aberrations by using incoherent illumination and interference imaging. *The European Physical Journal Special Topics*, 226(7):1603–1621, 2017.
- [216] Peng Xiao, Mathias Fink, and Albert Claude Boccara. Adaptive optics full-field optical coherence tomography. *Journal of biomedical optics*, 21(12):121505–121505, 2016.
- [217] Enrique J Fernández, Boris Hermann, Boris Považay, Angelika Unterhuber, Harald Sattmann, Bernd Hofer, Peter K Ahnelt, and Wolfgang Drexler. Ultrahigh resolution optical coherence tomography and pancorrection for cellular imaging of the living human retina. *Optics Express*, 16(15):11083–11094, 2008.
- [218] Omer P Kocaoglu, R Daniel Ferguson, Ravi S Jonnal, Zhuolin Liu, Qiang Wang, Daniel X Hammer, and Donald T Miller. Adaptive optics optical coherence tomography with dynamic retinal tracking. *Biomedical optics express*, 5(7):2262–2284, 2014.
- [219] Jerome Mertz, Hari Paudel, and Thomas G Bifano. Field of view advantage of conjugate adaptive optics in microscopy applications. *Applied optics*, 54(11):3498–3506, 2015.
- [220] Nathan Doble, Donald T Miller, Geunyoung Yoon, and David R Williams. Requirements for discrete actuator and segmented wavefront correctors for aberration compensation in two large populations of human eyes. *Applied optics*, 46(20):4501–4514, 2007.
- [221] Gordon D Love. Wave-front correction and production of zernike modes with a liquid-crystal spatial light modulator. *Applied optics*, 36(7):1517–1524, 1997.
- [222] Akondi Vyas, MB Roopashree, Ravinder Kumar Banyal, and B Raghavendra Prasad. Spatial light modulator for wavefront correction. *arXiv preprint arXiv:0909.3413*, 2009.
- [223] Larry N Thibos and Arthur Bradley. Use of liquid-crystal adaptive-optics to alter the refractive state of the eye. *Optometry & Vision Science*, 74(7):581–587, 1997.
- [224] Fernando Vargas-Martin, Pedro M Prieto, and Pablo Artal. Correction of the aberrations in the human eye with a liquid-crystal spatial light modulator: limits to performance. *JOSA A*, 15(9):2552–2562, 1998.
- [225] Guang-ming Dai. *Wavefront optics for vision correction*, volume 179. SPIE press, 2008.
- [226] Peng Xiao, Mathias Fink, and A Claude Boccara. Retinal imaging with adaptive optics full-field oct. In *Proc. of SPIE Vol*, volume 10053, pages 100530K–1, 2017.
- [227] Christoph K Hitzenberger, Angela Baumgartner, Wolfgang Drexler, and Adolf F Fercher. Dispersion effects in partial coherence interferometry: implications for intraocular ranging. *Journal of Biomedical Optics*, 4(1):144–151, 1999.

- [228] Artificial eye model. http://www.rowetechnical.com/retina_oct_phantom.html.
- [229] Christy K Sheehy, Qiang Yang, David W Arathorn, Pavan Tiruveedhula, Johannes F de Boer, and Austin Roorda. High-speed, image-based eye tracking with a scanning laser ophthalmoscope. *Biomedical optics express*, 3(10):2611–2622, 2012.
- [230] Template matching and slice alignment. <https://sites.google.com/site/qingzongtseng/template-matching-ij-plugin>.
- [231] Peng Xiao, Mathias Fink, and A Claude Boccara. Combining ff-oct with sd-oct for retinal imaging. In *Optical Coherence Imaging Techniques and Imaging in Scattering Media II*, volume 10416, page 104160K. International Society for Optics and Photonics, 2017.
- [232] ANSI Standard. Z136. 1. american national standard for the safe use of lasers. american national standards institute. *Inc., New York*, 2014.
- [233] Yves Le Grand. *Light, colour, and vision*. Wiley, 1957.
- [234] ANSI Standard. Z80. 36. american national standard for ophthalmics-light hazard protection for ophthalmic instruments. american national standards institute. *Inc., New York*, 2016.
- [235] Spectralis imaging platform. <https://business-lounge.heidelbergengineering.com/fr/en/products/spectralis/>.
- [236] John I Yellott. Spectral analysis of spatial sampling by photoreceptors: topological disorder prevents aliasing. *Vision research*, 22(9):1205–1210, 1982.
- [237] Laurin Ginner, Abhishek Kumar, Daniel Fechtig, Lara M Wurster, Matthias Salas, Michael Pircher, and Rainer A Leitgeb. Noniterative digital aberration correction for cellular resolution retinal optical coherence tomography in vivo. *Optica*, 4(8):924–931, 2017.
- [238] Adaptive optics retinal camera. <http://www.imagine-eyes.com/product/rtx1/>.
- [239] Kate Grieve, Olivier Thouvenin, Abhishek Sengupta, Vincent M Borderie, and Michel Paques. Appearance of the retina with full-field optical coherence tomographyffoct and the retina. *Investigative ophthalmology & visual science*, 57(9):OCT96–OCT104, 2016.
- [240] Olivier Thouvenin, Claude Boccara, Mathias Fink, Jose Sahel, Michel Pâques, and Kate Grieve. Cell motility as contrast agent in retinal explant imaging with full-field optical coherence tomography. *Investigative Ophthalmology & Visual Science*, 58(11):4605–4615, 2017.

Bliblio.bib

Résumé

Cette thèse traite de l'étude et du développement d'un système d'optique adaptative pour la tomographie par cohérence optique plein champ (AO-FFOCT en anglais) appliquée à l'imagerie haute résolution de la rétine. L'analyse de l'effet des aberrations géométriques sur les performances en FFOCT a montré que pour une illumination spatialement incohérente, la résolution transverse est insensible aux aberrations et ne fait que diminuer le niveau du signal. Comme ce sont des aberrations de bas ordres comme la myopie et l'astigmatisme qui prédominent pour l'œil humain, une méthode d'optique adaptative avec une configuration sans conjugaison qui utilise une correction de front d'onde en transmission est suggérée, puis appliquée à la correction de ces ordres afin de simplifier le système d'AO-FFOCT. Des corrections de front d'onde sont effectuées sans analyseur de surface d'onde, en utilisant le niveau du signal de FFOCT comme métrique. Des expériences avec des échantillons diffusants et un œil artificiel sont menées pour démontrer la faisabilité d'un système d'AO-FFOCT conçu pour la correction d'aberration. Afin de résoudre les problèmes posés par les mouvements oculaires et de compenser en temps réel la différence de chemin optique entre les deux bras de l'interféromètre, l'instrument de FFOCT est couplé à un système d'OCT spectral. Avec cette combinaison de systèmes, l'imagerie FFOCT in vivo cellulaire de la rétine à haute résolution a été réalisée pour la première fois sur l'œil humain.

Mots Clés

Tomographie par cohérence optique plein champ, Optique adaptative, Cohérence spatiale, Haute résolution, Imagerie de la rétine, Ophtalmologie

Abstract

This thesis follows the study and development of an adaptive optics full-field optical coherence tomography (AO-FFOCT) system, aiming for high resolution *en face* human retinal imaging. During the quantification of the effects of geometrical aberrations on the FFOCT system performance, it is shown that, with spatially incoherent illumination, the lateral resolution of FFOCT is insensitive to aberrations, which only cause the FFOCT signal reduction. Since low order aberrations like myopia and astigmatism dominate in human eye, a non-conjugate AO configuration by using transmissive wavefront corrector is suggested and applied for low order aberrations correction to simplify the AO-FFOCT system. Wavefront corrections are done with a wavefront sensorless method by using FFOCT signal level as the metric. Experiments with scattering samples and artificial eye model are conducted to demonstrate the feasibility of the customized AO-FFOCT system for aberration correction. In order to resolve the eye motion effects and employ real-time matching of the optical path lengths of the two interferometric arms in FFOCT, a system combination of traditional spectral-domain OCT with FFOCT is adopted. With this combined system, high resolution FFOCT cellular retinal imaging is achieved in human eye in vivo for the first time.

Keywords

Full-field optical coherence tomography, Adaptive optics, Spatial coherence, High resolution, Retinal imaging, Ophthalmology